7-10-2019

Decoding the History of the Early Solar System Using Comet Volatile Compositions

Nathan Roth
University of Missouri-St. Louis, nxrq67@mail.umsl.edu

DECODING THE HISTORY OF THE EARLY SOLAR SYSTEM USING COMET VOLATILE COMPOSITIONS

by

NATHANIEL XAVIER ROTH

A DISSERTATION

Presented to the Graduate Faculty of the

MISSOURI UNIVERSITY OF SCIENCE AND TECHNOLOGY

and

UNIVERSITY OF MISSOURI – ST. LOUIS

In Partial Fulfillment of the Requirements for the Degree

DOCTOR OF PHILOSOPHY

in

PHYSICS

2019

Approved by

Erika Gibb, Advisor
Paul Parris, Co-Advisor
Boncho Bonev
Bruce Wilking
Alexei Yamilov

ABSTRACT

Understanding the evolution of the solar system, as well as its current volatile content, requires knowledge of the initial conditions present in the solar nebula. As some of the first objects to accrete in the solar nebula, cometary nuclei are among the most primitive remnants of solar system formation, and their present-day volatile composition likely reflects the composition and conditions where (and when) they formed. As such, the volatile compositions of cometary nuclei may serve as "fossils" of solar system formation. High-resolution near-infrared spectroscopy offers a valuable tool for sampling the primary volatile (i.e., ices subliming directly from the nucleus) composition of comets via analysis of fluorescence emission in cometary comae. Sampling fluorescence emission from a suite of primary volatiles has become possible from state-of-the-art ground-based observatories.

An overarching goal of comet volatile composition studies is determining whether comets can be classified according to their volatile content and what this reveals about the history of the early solar system. Early work produced encouraging results, but recent work has left pressing questions regarding whether a compositional taxonomy based on near-infrared measurements is feasible, as well as how to place such measurements into a meaningful context. These include questions such as: Are observed systematic compositional differences between ecliptic comets and Oort cloud comets the result of evolutionary effects or reflective of formative conditions? Is temporal variability in coma composition a common phenomenon, and if so, how can present-day measurements be related to natal solar system conditions? This work examines these questions in the context of near-infrared measurements of an Oort cloud comet, a Jupiter-family comet, and an ecliptic comet. The interplay between evolutionary effects, formative conditions, and temporal variability is examined in the context of the evolving composition-based taxonomy and the interpretation of the results of comet composition studies.

ACKNOWLEDGMENTS

I would like to thank my advisor, Dr. Erika Gibb, for teaching me everything I know: from reducing spectroscopic data, to writing grant proposals, to how to be a good scientist and teacher. I have truly looked forward to coming to work every day for the last six years. My experience as a student in your lab has been phenomenal, and it is the standard by which I will judge my future positions. I would like to thank my committee members, Drs. Paul Parris, Boncho Bonev, Bruce Wilking, and Alexei Yamilov, for their service and contributions to this work.

I have been privileged to work with an outstanding team of comet scientists, Drs. Boncho Bonev, Michael DiSanti, Neil Dello Russo, Hideyo Kawakita, Adam McKay, and Ronald Vervack, Jr. I would like to thank each of you for your time and invaluable contributions to all aspects of my research. I have waited my entire life to work with a group of scientists like you, and have valued our collaborations immensely. I sincerely hope we continue to work together long after the publication of this dissertation.

My work has been generously supported by NASA Headquarters under the NASA Earth and Space Science Fellowship Program (Grant NNX16AP49H).

I would like to thank the professors of the Department of Physics & Astronomy at UMSL, as well as Dr. Paul Parris from Missouri S&T, for exceptionally taught graduate courses that I thoroughly enjoyed.

Finally, I would like to thank my family, especially my wife, Alyssa, who has been my most ardent supporter in earning my Ph.D. From my first day at UMSL to finding a postdoctoral position, you have been with me through every high and low, and believed in me even when I did not believe in myself. I can never thank you enough.

TABLE OF CONTENTS

Page

LIST OF ILLUSTRATIONS

Figure Page

LIST OF TABLES

1. INTRODUCTION

1.1. THE FORMATION OF THE SOLAR SYSTEM IN A NUTSHELL

The solar system originated as a dense fragment of a giant molecular cloud. These giant molecular clouds are nurseries of stellar formation. Variations in local density lead to the formation of dense clumps and fragments in the clouds, which eventually undergo gravitational collapse. At the center of the collapsing fragment, a star is born when the local density becomes sufficiently high to ignite thermonuclear fusion, while the outer material of the fragment flattens out into a disk of gas and dust surrounding the young star. Over the next several million years, all of the planets, asteroids, moons, and comets of a stellar system will accrete from this "protoplanetary disk" of gas and dust. The protoplanetary disk from which the solar system formed is known as the solar (or protosolar) nebula.

Understanding a range of events and processes in the history and evolution of the solar system, from the formation of the planets to the source(s) of water and organic matter on Earth, requires knowledge of the initial composition and conditions present in the solar nebula. As small (up to tens of km) bodies of ice and dust, comets are some of the smallest objects in the solar system and were among the first to accrete out of the solar nebula. Lacking a known mechanism for efficient self-heating owing to their small sizes, their present-day volatile composition likely reflects the composition and conditions where (and when) they formed.

1.2. COMETS: ORIGINS AND PRESENT-DAY RESERVOIRS

The majority of comets that become available for remote sensing can be placed into one of two dynamical groups: 1) Ecliptic comets, such as the Jupiter-family comets (JFCs) and 2P/Encke (one of the subjects of this work), which originate principally from

the scattered Kuiper disk and have small orbital inclinations, and 2) nearly isotropic Oort cloud comets (OCCs), which originate from the outer reaches of the solar system and have random orbital inclinations.

The dynamical reservoir of a given comet can be identified using the Jupiter Tisserand parameter, T_J, which measures Jupiter's gravitational influence on a comet's orbital path. Comets with $T_J < 2$ originate from the Oort cloud, a spherical distribution of comets in the outer solar system extending up to tens of thousands of AU, and include dynamically new comets which are entering the inner solar system for the first time. Oort cloud comets have long periods (hundreds to hundreds of thousands of years, or more), and are often ejected from the solar system by Jupiter following a passage through the inner solar system. Comets with $2 < T_J < 3$ are the JFCs, which reside in the Kuiper disk beyond the orbit of Neptune. These comets have considerably shorter periods than Oort cloud comets, on the order of several to tens of years, and as such offer the opportunity to study the effects of multiple close perihelion passages on volatile composition. Comets with $T_J > 3$ are subdivided into two groups depending on the semi-major axis of their orbit: comets with a semi-major axis interior to that of Jupiter are Encke-type comets, whereas those with a semi-major axis exterior to that of Jupiter and interior to Neptune are Chiron-type comets. The term "ecliptic comets" is also used interchangeably to describe the JFCs, Encke-type comets, or Chiron-type comets, as they lie in or near the plane of the solar system, known as the ecliptic plane.

Historically, OCCs were thought to form in-situ at heliocentric distances ($R_{\rm h}$) between 5-30 AU before being scattered to the Oort cloud, whereas ecliptic comets formed separately at even larger heliocentric distances. However, the detection of crystalline silicates in some comets, e.g., 1P/Halley (Bregman *et al.*, 1987), 9P/Tempel 1 (via remote observations of material ejected during the Deep Impact mission (Harker *et al.*, 2005)), and 81P/Wild 2 (in grains returned by the Stardust mission (Zolensky *et al.*, 2006)) imply that material in their nuclei was processed at small $R_{\rm h}$ and mixed over ranges of distances

in the solar nebula. Additionally dynamical modeling (e.g., Gomes *et al.* (2005); Levison *et al.* (2011); Morbidelli *et al.* (2005)) suggests that comets were emplaced in their current dynamical reservoirs (either the Oort cloud or the Kuiper disk) early in the history of the solar system by gravitational scattering due to the migration of the giant planets. Taken together, this evidence suggests that comet formation was instead a more "spatially mixed" process.

Since their emplacement in the Oort cloud or the Kuiper disk, the interior compositions of cometary nuclei have remained (at least to a large degree) unchanged. Most processes that may alter the properties of the nucleus during its ($\sim$ 4.5 billion years) residence in the Oort cloud (or the Kuiper disk) are expected to affect a thin (a few meters deep) layer near the surface (Stern, 2003). This layer is lost during a typical passage through the inner solar system.

1.3. TAXONOMIES OF COMETS

Classifying comets according to their present day dynamical reservoir is useful for planning observations. However, given the complex "spatially mixed" process of comet formation and the scattering processes which placed comets in their current orbits, the volatile compositions of cometary nuclei may represent widely varying (or at the other extreme, largely overlapping) formation regions in the solar nebula, which have no ties to a particular comet's present day orbital characteristics. In terms of tying the present day volatile composition of comets to formative regions and conditions in the solar nebula, a taxonomy based on the volatile composition of comets is more informative.

1.3.1. Compositional Taxonomies of Comets as Measured at Optical and Radio Wavelengths. Comets have been observed and characterized at optical wavelengths for over thirty years, leading to large databases of photometric and spectroscopic observations and the development of a taxonomy based on composition (e.g., A'Hearn *et al.* (1995); Cochran *et al.* (2012) and references therein). Fragment species (e.g., CN, C_2, C_3, CS, NH, OH)

formed by photodissociation of larger molecules in the coma have spectroscopic features at optical wavelengths. Based on their fragment species composition, comets are broadly classified as either "normal" or "carbon-chain depleted", with as many as seven distinct taxonomic subgroupings (Cochran *et al.*, 2015; Schleicher and Bair, 2014). However, relating mixing ratios of fragment species to those of their parents is difficult due to their complicated lineage (multiple possible parents, including dust grains).

Primary volatiles, including complex molecules such as ethylene glycol, emit in the radio via rotational transitions. However, there is no agreement on the existence of taxonomic classes based on composition as measured at radio wavelengths (Crovisier *et al.*, 2009; Mumma and Charnley, 2011).

1.3.2. Compositional Taxonomies of Comets as Measured at Near Infrared Wavelengths. A suite of primary volatiles (i.e., ices subliming directly from the nucleus) emit in the near-infrared via ro-vibrational transitions. Using state-of-the-art near-infrared spectrographs such as CSHELL and iSHELL at the 3 m NASA Infrared Telescope Facility and NIRSPEC at the 10 m W. M. Keck Observatory, fundamental transitions of OCS, CO, H_2CO, CH_3OH, C_2H_6, CH_4, HCN, C_2H_2, and NH_3, and hot band transitions of H_2O can be sampled from the ground in sufficiently bright comets. The outputs of these studies include best-fit rotational temperatures, molecular production rates, molecular abundances ("mixing ratios") relative to H_2O (the dominant ice in most comets studied), and maps of molecular column density along the slit, known as emission spatial profiles.

Figure 1.1 shows spatial profiles of emissions for hydrocarbon species (C_2H_6, C_2H_2, CH_4), H_2O, and dust grains in OCC 153P/Ikeya-Zhang. These spatial profiles show that the emission intensity of each volatile peaks at the position of the nucleus and falls off with increasing nucleocentric distance (ρ) as $1/\rho$, consistent with ices subliming directly from the nucleus with constant outflow velocity followed by adiabatic expansion. This suggests that they are indeed "primary" volatiles. Thus, the core hypothesis in the interpretation of the results of these near-infrared measurements is that once sublimation of H_2O, the

least volatile ice in comets, is fully activated, the mixing ratios of primary volatiles in comet comae should remain relatively constant and reflect the native composition of the nucleus (assuming compositional homogeneity). Comets observed to date in the near-infrared suggest that this is true in general, although some primary volatiles (NH_3, H_2CO, and C_2H_2) and fragment species (CN and NH_2) show a trend towards enhanced production at heliocentric distance (R_h) < 0.8 AU (possibly due to release from grains; e.g., see Dello Russo *et al.* (2016a)).

The matter of classifying comets according to their primary volatile composition has proven to be a complex undertaking. Early near-infrared spectroscopic studies of the primary volatile compositions of comets 1P/Halley (Mumma *et al.*, 1986), C/1996 B2 (Hyakutake) (Dello Russo *et al.*, 2002b; DiSanti *et al.*, 2003; Magee-Sauer *et al.*, 2002b; Mumma *et al.*, 1996) and C/1995 O1 (Hale-Bopp) (Dello Russo *et al.*, 2001, 2000; DiSanti *et al.*, 2001; Magee-Sauer *et al.*, 1999) revealed that they are chemically similar objects (Mumma *et al.*, 2003). Subsequent observations of comet D/1999 S4 (LINEAR) prior to its complete disruption (Mumma *et al.*, 2001b) and of the split comet 73P/Schwassman-Wachmann 3B (Dello Russo *et al.*, 2007; Villanueva *et al.*, 2006) showed two comets that were highly depleted in virtually all trace primary volatiles relative to water. At the other extreme, comets C/2001 A2 (LINEAR) (Magee-Sauer *et al.*, 2008) and later C/2007 W1 (Boattini) (Villanueva *et al.*, 2011a) were enriched in the sampled trace primary volatiles. These results formed the basis for a proposed three-tiered taxonomy based on primary volatile abundance ratios, with comets classified as organics-enriched, organics-normal, or organics-depleted (e.g., Mumma and Charnley (2011) and references therein).

However, recent work has suggested that the three-fold classification scheme is incomplete and more complex (see Dello Russo *et al.* (2016a) for a recent review of comet taxonomies based on near-infrared spectroscopy). For example, the primary volatile compositions of comets 8P/Tuttle, C/2007 N3 (Lulin), and 2P/Encke (Bonev *et al.*, 2008b; Gibb *et al.*, 2012; Radeva *et al.*, 2013; Roth *et al.*, 2018) show no systematic enrichment, deple-

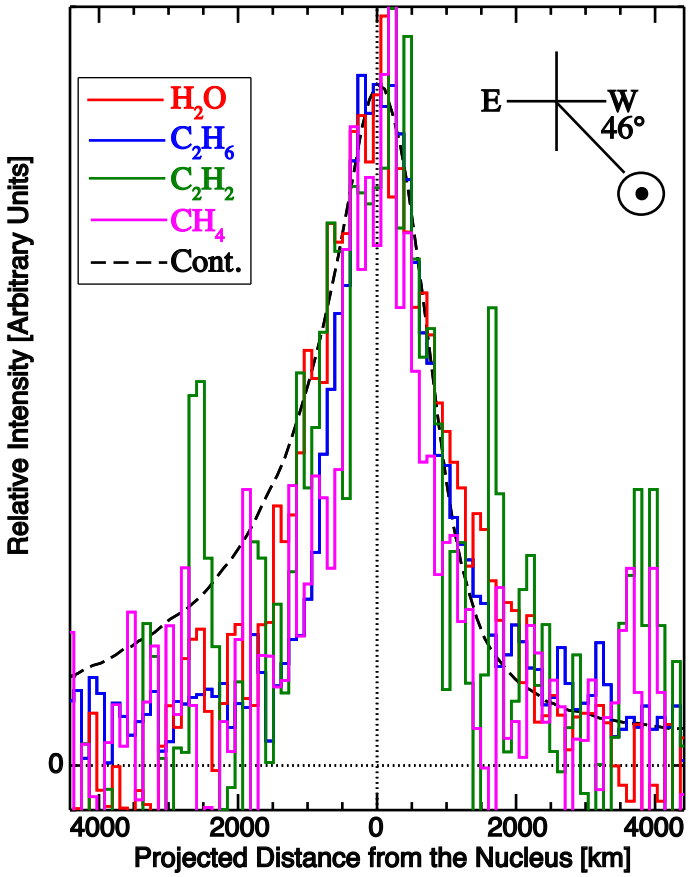

Figure 1.1. Spatial profiles of emissions in 153P/Ikeya-Zhang for C_2H_6 (blue), C_2H_2 (green), CH_4 (purple), H_2O (red), and dust (black, dashed) on UT 2002 March 21. The slit was oriented East-West, and the direction of the Sun relative to the slit is indicated.

tion, or similarity to the mean. Among these three comets (2P/Encke is a special case, see Section 3), CH_3OH may be seen as a "smoking gun" in that it is "overabundant" compared to other primary volatiles. Specifically, these three comets all had high CH_3OH abundances while being depleted in certain other molecules, for example C_2H_2, and "normal" in others, such as C_2H_6. This suggests that the chemical diversity among comets is more complex than the simple organics-enriched, organics-normal, and organics-depleted framework.

1.4. THE IMPACT OF EVOLUTIONARY EFFECTS VS. NATAL CONDITIONS ON COMET VOLATILE COMPOSITIONS

Although forming a comprehensive comet taxonomy based on composition as revealed at near-infrared wavelengths has proven elusive, results from all wavelengths have shown that considerable compositional diversity exists in the comet population. In particular, measured Jupiter-family comets are on average depleted in their primary volatiles relative to Oort cloud comets. If these systematic compositional differences are indicative of natal conditions, they would imply that JFCs formed in a compositionally distinct region in the solar nebula from that where OCCs formed.

However, there is some question of how repeated close encounters with the Sun affect volatile composition, and evolutionary effects over the ~4.5 billion year lifetime of comets must be considered. Although most processes that may alter the properties of the nucleus are expected to affect a thin (at most a few meters deep) layer near the surface over the course of a typical perihelion passage, an ecliptic comet experiencing many perihelion passages, particularly at small $R_{\rm h}$, may (possibly) suffer considerable processing compared to a dynamically new Oort cloud comet entering the inner solar system for the first time. Understanding potential evolutionary effects, including the systematic differences between ecliptic comets and OCCs, is critical to interpreting the clues of solar system formation that are imprinted in the ices of cometary nuclei, as well as to placing the results of present day observations into a meaningful context.

Interpreting the results of volatile composition studies also requires overcoming observational biases. Thus far, near-infrared studies of primary volatile composition have largely been "snapshots" – observations over a single apparition and at most a small range of $R_{\rm h}$ (often near ~ 1 AU) for comets that, in many cases, will make a single perihelion passage in a human lifetime. Although several comets have been observed in the near-infrared at small $R_{\rm h}$ (< 0.8 AU, e.g. DiSanti *et al.* (2017, 2016, 2003); Gibb *et al.* (2003)) and

large R_h (> 2 AU, e.g. Bonev *et al.* (2017); Brooke *et al.* (2003); Kawakita *et al.* (2014); Magee-Sauer *et al.* (1999); Paganini *et al.* (2012)), to date no comets have had a complete primary volatile inventory characterized over multiple apparitions.

Additionally, certain primary volatiles (specifically, C_2H_2, OCS, CO, and CH_4) are underrepresented in studies of comets as a whole, and in particular in studies of ecliptic comets. In the case of C_2H_2 and OCS, this has been due largely to limitations in sensitivity and lack of spectral coverage, respectively. For CH_4 and CO, their fundamental ro-vibrational bands are heavily populated in Earth's atmosphere, resulting in highly opaque telluric counterparts and requiring that comets have sufficiently large geocentric velocity (Δ_{dot}) to Doppler-shift corresponding cometary emissions to regions of adequate atmospheric transmittance. To compensate for their low brightness, most observations of ecliptic comets take place near closest passage to Earth, coinciding with small Δ_{dot}, and so precluding measurement of CO and CH_4. This has resulted in a significant paucity of detections of CO and CH_4 in ecliptic comets. Owing to their status as "hypervolatiles", cometary abundances of CO and CH_4 can provide unique insights into the processing in the early solar system (Dello Russo *et al.*, 2016a). Improving the number of secure measurements of these species in ecliptic comets is one of the primary goals of this work (see Sections 3 and 4 for more details).

1.5. COMPOSITIONAL HETEROGENEITY AND VARIABILITY IN COMETS

Although near-infrared measurements of the volatile composition of comets to date suggest that mixing ratios of trace species remain relatively constant once sublimation of H_2O is fully activated, this is not a hard and fast rule. A'Hearn *et al.* (1985) found that OH (and by proxy, water) production in the ecliptic comet 2P/Encke was symmetric about perihelion, whereas C_2, C_3, and CN production was much lower post-perihelion vs. pre-perihelion.

Non-uniform volatile mixing ratios have been observed in other comets, including during the Rosetta mission to JFC 67P/Churyumov-Gerasimenko. At comet 67P/C-G, Rosetta found that mixing ratios of CO and CO_2 in the coma varied due to seasonal effects on the nucleus (Hässig *et al.*, 2015). In these seasonal effects, different portions of the nucleus receive seasonal illumination during different portions of an orbit due to the comet's orientation with respect to the Sun, leading to distinct sources on the nucleus dominating outgassing at different times. Furthermore, variation in volatile mixing ratios was found on smaller time scales, with some volatiles (such as CH_4) showing diurnal variations that differed from those for other volatiles, such as CO and C_2H_6 (Bockelée-Morvan *et al.*, 2016; Fink *et al.*, 2016; Luspay-Kuti *et al.*, 2015).

Additionally, non-uniform mixing ratios of CO/H_2O were observed in OCC C/2009 P1 (Garradd) by both ground-based studies (McKay *et al.*, 2015) and spaced-based studies from the High Resolution Instrument Infrared Spectrometer aboard the *Deep Impact Flyby* spacecraft (Feaga *et al.*, 2014). In C/2009 P1 (Garradd), H_2O production rates traced the predicted heliocentric dependence, rising and then falling near perihelion. However, CO production increased monotonically throughout the apparition, continuing to rise long after perihelion, perhaps due to seasonal effects on the nucleus.

There is also evidence that some primary volatiles (NH_3, H_2CO, C_2H_2) display enhanced production at small R_h ($<\sim$ 0.8 AU), perhaps due to grain sources (Dello Russo *et al.*, 2016a). Furthermore, in the sun-grazing comet D/2012 S1 (ISON), HCN, NH_3, C_2H_2, and H_2CO showed increased abundances at small R_h (DiSanti *et al.*, 2016). However, as noted earlier, measurements of a given comet across a large range of R_h during a particular apparition are sparse, leaving the matter unresolved. Determining to what extent these phenomena occur in the comet population is crucial to interpreting the results of volatile composition studies and placing them in a meaningful context.

1.6. OVERVIEW OF OBSERVATIONS AND SPECTROSCOPIC DATA REDUCTION

This section will provide an overview of the the techniques used for the near-infrared spectroscopic observations reported in this work, as well as the procedures used for data reduction and analysis.

1.6.1. Observations. To address these pressing matters in cometary science, this study includes near-infrared spectroscopic measurements of the primary volatile compositions of three comets: the dynamically new OCC C/2012 K1 (PanSTARRS), the JFC 21P/Giacobini-Zinner, and the ecliptic comet 2P/Encke (the prototypical Encke-type comet). In all cases, these measurements were acquired with state-of-the-art near-infrared spectrographs at professional ground-based observatories. Measurements of C/2012 K1 (PanSTARRS) were obtained with NIRSPEC (McLean *et al.*, 1998) at the 10 m W. M. Keck Observatory. Measurements of comets 2P/Encke and 21P/Giacobini-Zinner were acquired with the newly-commissioned iSHELL spectrograph (Rayner *et al.*, 2012, 2016) at the 3 m NASA Infrared Telescope Facility.

Although there are notable differences in the spectrographs, such as nominal resolving power, array size, and spectral grasp, the observational techniques used to acquire data, as well as the data reduction algorithms, all operate on the same basic principles and are fundamentally similar for both instruments. A brief overview of these is given here, and a comprehensive description is provided in Appendix A.

Settings for both spectrographs were chosen so as to fully and efficiently sample a suite of molecular abundances. Observations were performed using a standard ABBA nod pattern, with A and B beams symmetrically placed about the midpoint of the slit and separated by half its length (on-chip nodding). In the case of 21P/Giacobini-Zinner, some of the data were acquired using off-chip nodding (see Section 4), in which the A beam is placed at the midpoint of the slit whereas the B beam is placed perpendicular to the slit. Combining spectra of the nodded beams as A-B-B+A cancelled emissions from thermal

background, instrumental biases, and "sky" emission (lines and continuum) to second order. The data were dark subtracted, flat-fielded, and cleaned of cosmic ray hits and "hot" (high dark current) pixels. Flux calibration was performed using appropriately placed bright IR flux standards on each date.

1.6.2. Data Reduction. The data reduction procedures used are described extensively in the refereed literature (Bonev, 2005; DiSanti *et al.*, 2006, 2014; Radeva *et al.*, 2010; Villanueva *et al.*, 2009). Their application to unique aspects of iSHELL spectra (in the case of comets 2P/Encke and 21P/Giacobini-Zinner) is detailed in §3.2 of DiSanti *et al.* (2017). Contributions from continuum and gaseous emissions were determined in the comet spectra as previously described (e.g. DiSanti *et al.* (2016)). This procedure is illustrated in Figure 1.2. The fully resolved transmittance function was convolved to the resolving power of the data (~2 x 10^4 for NIRSPEC, ~4 x 10^4 for iSHELL) and scaled to the level of the comet continuum. The modeled continuum was then subtracted to isolate cometary emission lines.

Nucleocentric (or "nucleus-centered") production rates (Q_{NC}) were determined using a well-documented formalism (Bonev, 2005; Dello Russo *et al.*, 1998; DiSanti *et al.*, 2001; Villanueva *et al.*, 2011a); see Section 3.2.2 of DiSanti *et al.* (2016) for further details. The nucleocentric production rates were multiplied by an appropriate growth factor (GF), which was determined using the well-established Q-curve methodology (e.g. Bonev (2005); DiSanti *et al.* (2001); Gibb *et al.* (2012)) to establish a total (or global) production rate, Q. This GF corrects for atmospheric seeing, which suppresses signal along lines of sight passing close to the nucleus due to the use of a narrow slit, as well as potential drift of the comet during an exposure sequence.

1.6.3. Molecular Fluorescence Analysis. Synthetic models of fluorescence emission for each targeted species were compared to observed line intensities, after correcting each modeled line intensity (g-factor) for the monochromatic atmospheric transmittance at its Doppler-shifted wavelength (according to the geocentric velocity of the comet at the time

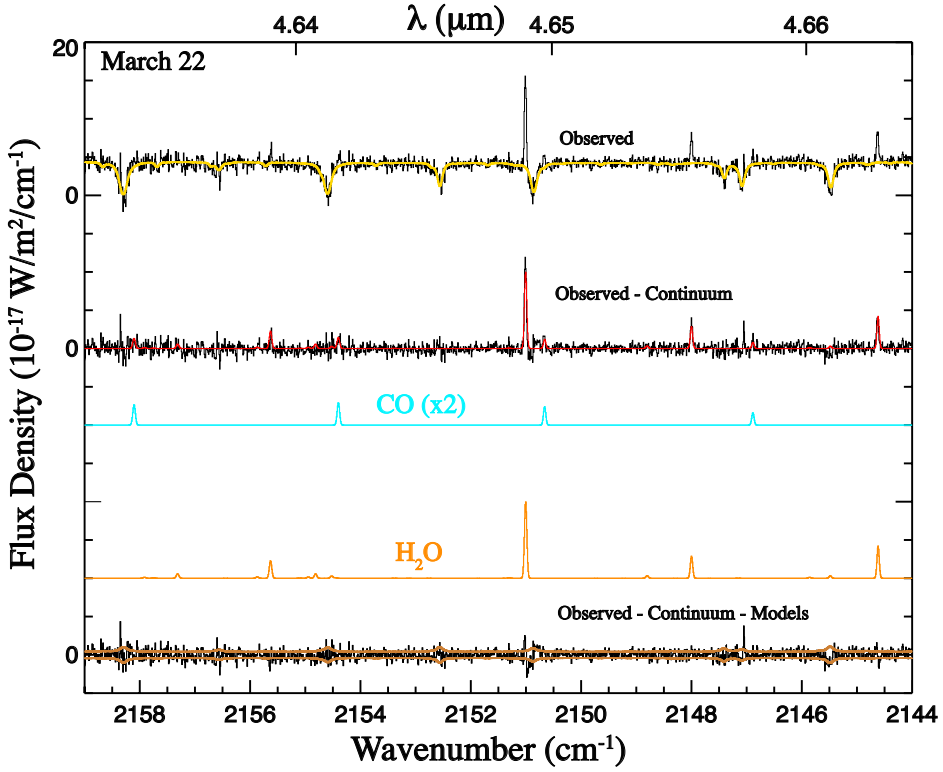

Figure 1.2. Extracted spectra showing clear detections of CO and H_2O in comet Encke superimposed on the cometary continuum on UT 2017 March 22. The gold trace overplotted on the uppermost cometary spectrum is the telluric absorption model (convolved to the instrumental resolution). Directly below is the residual spectrum (after subtracting the telluric absorption model), with the total modeled fluorescence emission overplotted in red. Individual fluorescence emission models (color-coded by species) are plotted below, offset vertically for clarity. At the bottom of each panel is the residual spectrum (after subtracting the telluric absorption model and all relevant molecular fluorescence models), with the 1σ uncertainty envelope overplotted in bronze.

of the observations). The *g*-factors used in synthetic fluorescence emission models in this study were generated with quantum mechanical models developed for each molecule. These models include CH_4 (Gibb *et al.*, 2003), C_2H_6 (Villanueva *et al.*, 2011b), H_2O (Villanueva *et al.*, 2012b), CH_3OH (DiSanti *et al.*, 2013; Villanueva *et al.*, 2012a), HCN (Lippi *et al.*, 2013; Villanueva *et al.*, 2011a), H_2CO (DiSanti *et al.*, 2006), OH* (Bonev *et al.*, 2006), C_2H_2 (Villanueva *et al.*, 2011a), CO (Paganini *et al.*, 2013b), and NH_3 (Villanueva *et al.*, 2013). A Levenberg-Marquardt nonlinear minimization technique (Villanueva *et al.*, 2008)

was used to fit fluorescence emission from all species simultaneously in each echelle order, allowing for high-precision results, even in spectrally crowded regions containing many spectral lines within a single instrumental resolution element. Production rates for each sampled species were determined from the appropriate fluorescence model at the rotational temperature of each molecule.

1.6.4. Determination of Rotational Temperature. Rotational temperatures were determined using correlation and excitation analyses as described in Bonev (2005); Bonev *et al.* (2008a); DiSanti *et al.* (2006); Villanueva *et al.* (2008). In general, well-constrained rotational temperatures can be determined for individual species with intrinsically bright lines and for which a broad range of excitation energies is sampled. These conditions were satisfied for H_2O by at least one setting in each data set.

2. THE COMPOSITION OF COMET C/2012 K1 (PANSTARRS) AND THE DISTRIBUTION OF PRIMARY VOLATILE ABUNDANCES AMONG COMETS

2.1. COMET C/2012 K1 (PANSTARRS)

Comet C/2012 K1 (PanSTARRS) (hereafter K1) was a dynamically new Oort cloud comet on its first journey into the inner solar system (Nakano, 2013). K1 reached perihelion (1.05 AU) on 2014 August 27 and was closest to Earth (0.95 AU) on 2014 October 31. On 2014 May 22 and 24, K1 was observed with the high-resolution ($\lambda/\Delta\lambda \approx 25{,}000$), near-infrared, long-slit echelle spectrograph NIRSPEC at the 10 m W. M. Keck Observatory (McLean *et al.*, 1998) to characterize its volatile composition.

The observing log is shown in Table 2.1. Seeing improved from $\sim 0.5''$ to $\sim 0.2''$ over the course of the night on May 22, and was stable at $\sim 0.5''$ on May 24. The column burden of atmospheric water vapor (expressed in precipitable millimeters) retrieved in fitting synthetic telluric absorption models to flux standard star continua was 2.9 on May 22, and 2.2 on May 24.

Table 2.1. C/2012 K1 (PanSTARRS) observing log and H_2O production rates.

Date (2014)	NIRSPEC Setting	UT	R_h (AU)	Δ (AU)	Δ_{dot} (km s^{-1})	T_{int} (minutes)	$Q(H_2O)$ (10^{28} s^{-1})
5/21	KL1	6:20 – 7:10	1.857	1.557	14.98	32	4.46 ± 0.27
	KL2	7:18 – 8:46	1.857	1.557	15.10	52	4.39 ± 0.31
5/22	KL1	5:48 – 6:29	1.834	1.574	16.02	28	5.95 ± 0.29
	MWA	6:39 – 8:37	1.833	1.575	16.14	28	3.61 ± 1.07
	KL2	8:49 – 9:06	1.832	1.576	16.26	16	3.53 ± 0.68

[1] R_h, Δ, and Δ_{dot} are heliocentric distance, geocentric distance, and geocentric velocity, respectively, of C/2012 K1 (PanSTARRS). T_{int} is total integration time on source, and $Q(H_2O)$ is the global water production rate.

2.2. RESULTS

Production rates were determined for six primary volatiles (H_2O, HCN, CH_4, CH_3OH, C_2H_6, and CO), and stringent upper limits were obtained for three others (C_2H_2, NH_3, and H_2CO) in K1. Growth factors (defined as GF = Q_{global}/Q_{NC}, where Q_{NC} is the nucleocentric production rate – see Section 1.6.2 and Appendix A.4.3, A.4.4) were determined for both the gas and the dust when the signal-to-noise ratio (S/N) was sufficiently high (i.e., only for water and ethane). These two species had similar spatial profiles (see Figure 2.1) and therefore, since their photodissociation lifetimes are comparable, provided similar growth factors. Table 2.2 shows rotational temperatures, production rates, and mixing ratios for all sampled species in K1 on each date.

For these observations, the most robust rotational temperature (T_{rot} = 42 ± 7 K) was found for H_2O in order 26 of the KL2 setting on May 22. A rotational temperature for HCN (43^{+11}_{-10} K) was also retrieved, in agreement with that for water. In general, rotational temperatures agree for different primary species measured at infrared wavelengths (see for example Gibb *et al.* (2012) and references therein; also see §3.2.1 of DiSanti *et al.* (2016)), supporting this approach. The rotational temperature derived for H_2O was therefore applied to species for which the rotational temperature could not be well-constrained.

The H_2O rotational temperature was poorly constrained on May 24, owing to poor S/N (less on-source integration time, see Table 2.1) in orders with temperature-sensitive water lines. Therefore, the May 22 H_2O rotational temperature was adopted in determining production rates and abundances on May 24. Additionally the water production rate in the KL1 setting on May 24 was significantly higher than that found for the KL2 setting (see Table 2.2), as well as the water production rate on May 22. However, production rates for all other traces volatiles in the KL1 setting on May 24 agree within uncertainty with those on May 22. McKay *et al.* (2016) reported a water production rate of 4.35(0.44) x 10^{28} s^{-1}

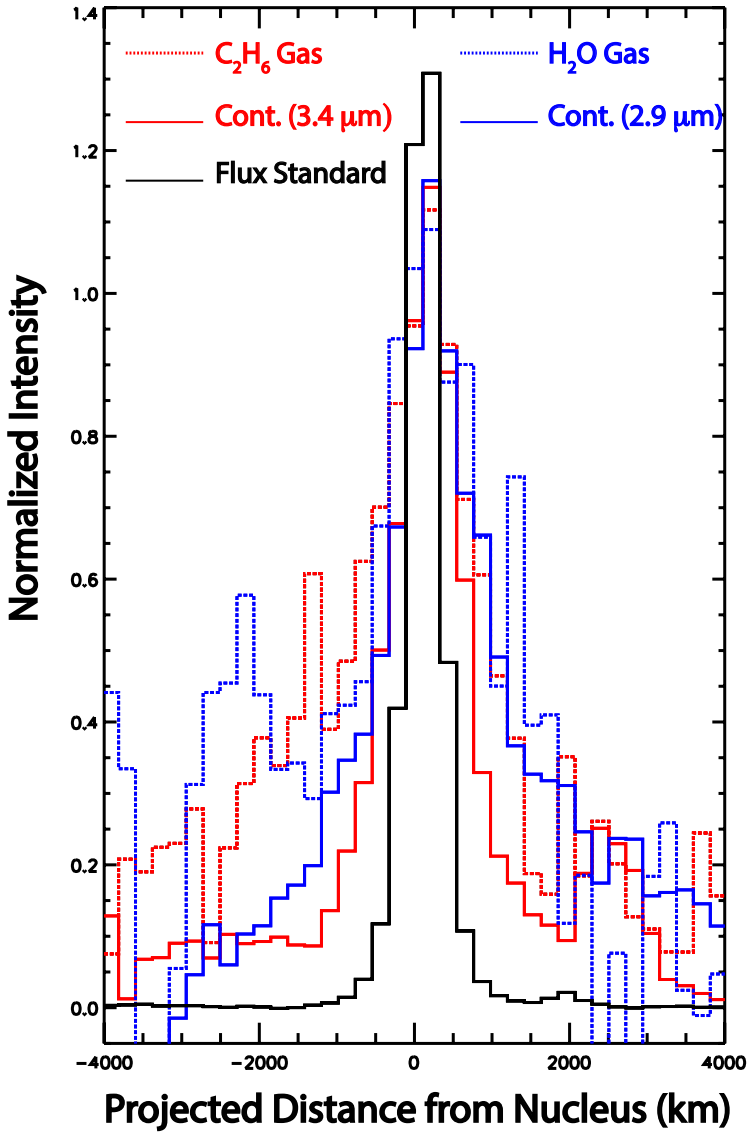

Figure 2.1. Spatial profiles of emission for C_2H_6 gas (dashed red line) and co-measured dust (solid red line), H_2O gas (dashed blue line) and co-measured dust (solid blue line), as well as the PSF for the flux standard on May 22 from the KL1 setting. All profiles are normalized to the mean intensity of the central three pixels.

on May 24, consistent with the $Q(H_2O)$ from May 22 reported here. Such variations are not unknown in comet observations and may be due to short-term variability. Spectra and best-fit fluorescence models are shown in Figures 2.2-2.6.

Table 2.2. Volatile composition of C/2012 K1 (PanSTARRS).

Setting	Molecule	T_{rot}[(1)] (K)	Growth Factor[(2)]	Q[(3)] (10^{26} mol s^{-1})	Q_x/Q_{H2O} (%)
2014 May 22, R_h = 1.857 AU, Δ = 1.557 AU, Δ_{dot} = 15 km s^{-1}					
KL2	H_2O	42 ± 7	1.6 ± 0.2[(4)]	439 ± 31	100
	H_2CO	(42)	(1.6)	<0.61 (3σ)	<0.14 (3σ)
	CH_4	(42)	(1.6)	2.02 ± 0.37	0.46 ± 0.09
	HCN	(42)	(1.6)	0.66 ± 0.07	0.15 ± 0.02
		43^{+11}_{-10}	(1.6)	0.67 ± 0.07	0.15 ± 0.02
	C_2H_2	(42)	(1.6)	<0.49 (3σ)	<0.11 (3σ)
	NH_3	(42)	(1.6)	<7.6 (3σ)	<1.8 (3σ)
KL1	H_2O	(42)	1.7 ± 0.1[(4)]	446 ± 27	100
	C_2H_6	(42)	1.7 ± 0.1[(5)]	4.37 ± 0.18	0.98 ± 0.07
Order 22	CH_3OH	(42)	(1.7)	10.5 ± 1.6	2.36 ± 0.39
Order 23				13.6 ± 1.3	3.06 ± 0.35
				12.4 ± 1.2[(6)]	2.74 ± 0.26
2014 May 24, R_h = 1.834 AU, Δ = 1.574 AU, Δ_{dot} = 16 km s^{-1}					
KL2	H_2O	(42)	1.6 ± 0.2[(4)]	353 ± 68	100
	HCN	(42)	(1.6)	0.39 ± 0.10	0.11 ± 0.04
KL1	H_2O	(42)	(1.6)	595 ± 29	100
	C_2H_6	(42)	1.6 ± 0.1[(4)]	4.63 ± 0.32	0.80 ± 0.06
	CH_3OH	(42)	(1.6)	15.0 ± 2.0	2.58 ± 0.36
	CH_4	(42)	(1.6)	<5.4 (3σ)	<0.91 (3σ)
MWA	H_2O	(42)	(2.0)	361 ± 107	100
	CO	(42)	(2.0)	14 ± 2	3.9 ± 1.2

[1] Rotational temperature. Values in parentheses are assumed.
[2] Growth factor. Values in parentheses are assumed.
[3] Global production rate. Errors in production rate include line-by-line deviation between modeled and observed intensities and photon noise (see Bonev (2005); Bonev *et al.* (2007); Dello Russo *et al.* (2004)).
[4] Continuum (dust) growth factor.
[5] Gas growth factor.
[6] Weighted average CH_3OH production rate from KL1 Order 22 and KL1 Order 23.

How does the primary volatile composition of comet K1 compare to other sampled Oort cloud comets? Table 2.3 shows the mixing ratios of all targeted primary volatiles in K1 (given as a weighted average for molecules detected on both dates). For comparison, Table 2.3 also provides the median abundances of these molecules as measured among Oort cloud comets using near-infrared spectroscopy only (Dello Russo *et al.*, 2016a),

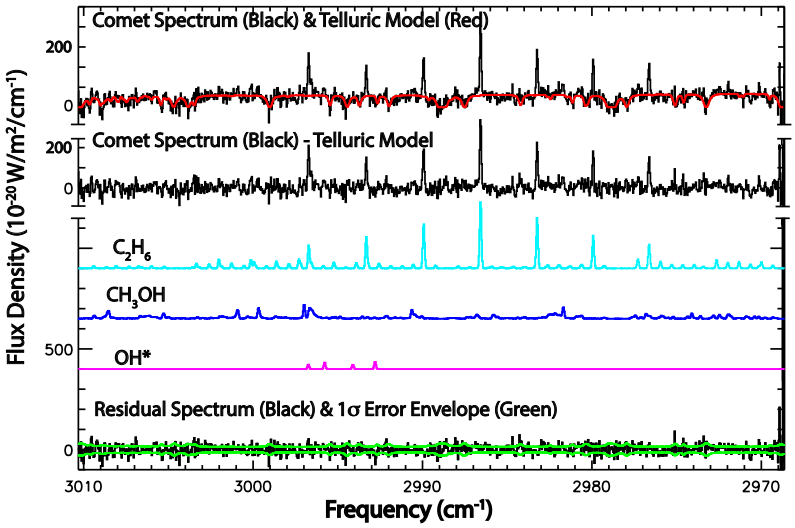

Figure 2.2. Detections of C_2H_6, CH_3OH, and OH* in comet C/2012 K1 on 2014 May 22, with traces and labels as described in Figure 1.2.

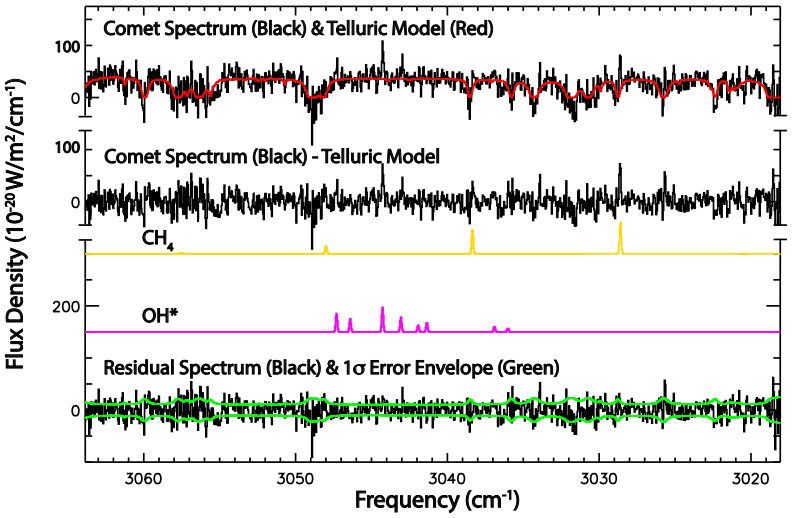

Figure 2.3. Detections of CH_4 and OH* in C/2012 K1 on 2014 May 22.

thereby avoiding uncertainties introduced when comparing results obtained over different wavelength regimes. From these it can be seen that C_2H_6 (0.87%) and CH_3OH (2.69%)

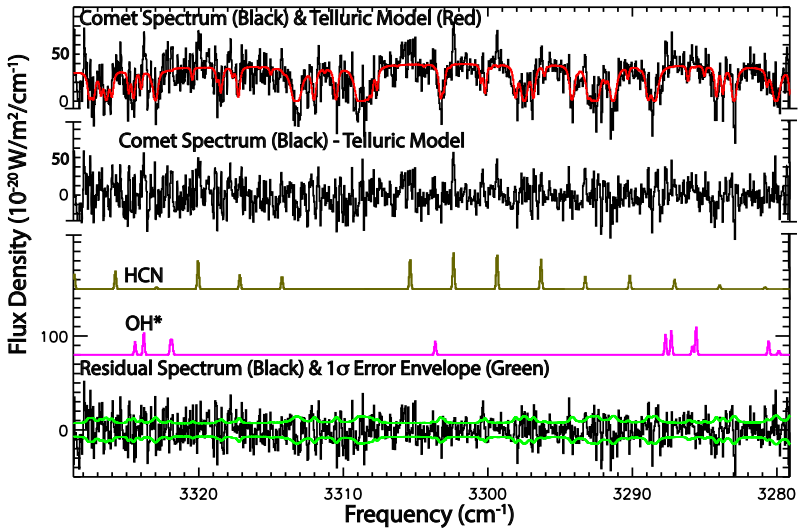

Figure 2.4. Detections of HCN and OH* in C/2012 K1 on 2014 May 22.

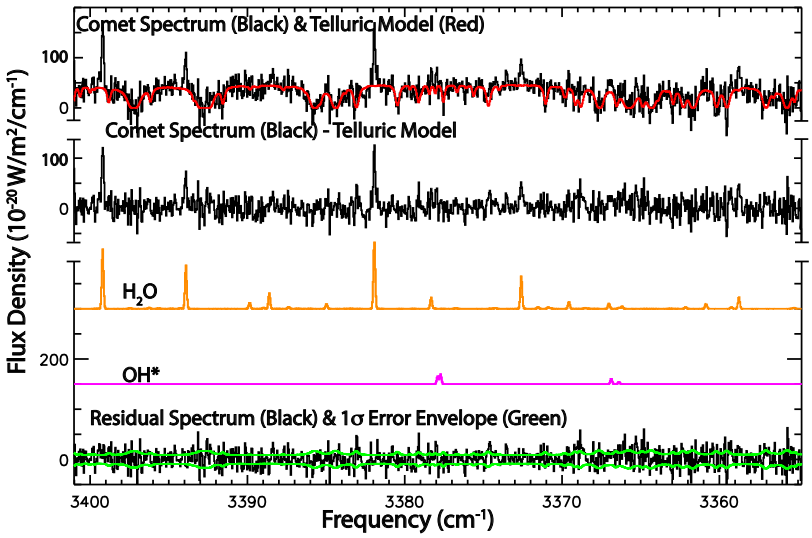

Figure 2.5. Detections of H_2O and OH* in C/2012 K1 on 2014 May 22.

are enriched, while CO (3.9%) and HCN (0.14%) are consistent with the cometary median. CH_4 (0.46%) and H_2CO (<0.14%) are depleted, and the 3σ upper limit for C_2H_2 (<0.11%) suggests it may be as well.

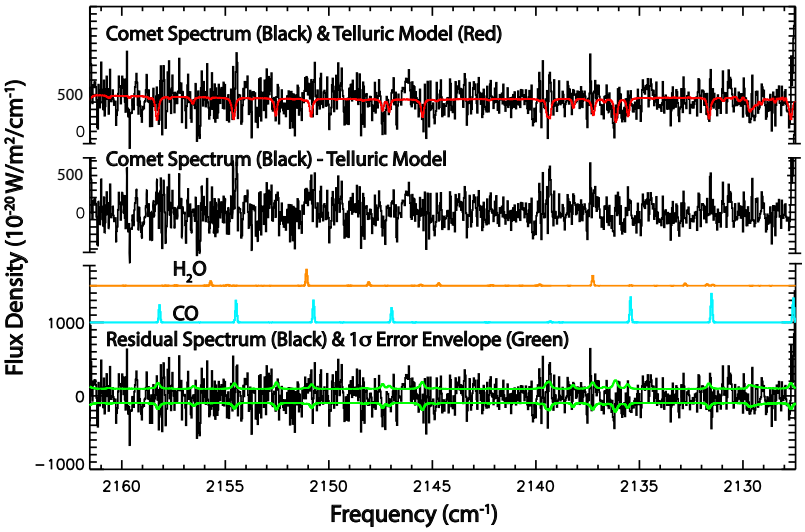

Figure 2.6. Detections of H_2O and CO in C/2012 K1 on 2014 May 24.

Table 2.3. Primary volatiles in K1 and in Oort cloud comets observed to date.

Molecule	Abundance in K1[1] (%)	Median Abundance in OCCs[2] (%)
C_2H_6	0.87 ± 0.05	0.61
CH_3OH	2.69 ± 0.21	2.14
CH_4	0.46 ± 0.09	0.90
CO	3.9 ± 1.2	3.73
HCN	0.14 ± 0.02	0.19
NH_3	<1.8	0.66
H_2CO	<0.14	0.38
C_2H_2	<0.11	0.17

[1] Abundances are given as weighted averages for molecules detected on both dates, excepting CO (searched only on May 24) and CH_4 (detected only on May 22 – the 3σ upper limit for CH_4 on May 24 is consistent). Upper limits for non-detected species are 3σ.

[2] Median abundances derived from Dello Russo *et al.* (2016a).

2.3. DISCUSSION

Given its primary volatile composition, it is clear that K1 is another example of a comet which shows no systematic enrichment, depletion, or similarity to median abundances. K1 does not fit into any taxonomic class, and taken together with previous examples (Section 1.3.2), suggests that the chemical diversity among comets is more complex than the simple organics-enriched, organics-normal, and organics-depleted framework.

The next natural question is whether the distribution of primary volatiles among comets is more nearly continuous versus distinct. Figure 2.7 shows abundances relative to water for HCN, C_2H_6, CH_3OH, and CH_4, respectively, in comets. For each molecule, most comets have abundances close to their median value, with some showing enrichment in certain molecules and depletion in others. Overall, the abundances of well-sampled primary volatiles, such as HCN, C_2H_6, and CH_3OH, suggest the emergence of a continuous distribution among comets. The graphic for HCN (Figure 2.7A), one of the most well measured volatiles in comets, shows an example of a well filled-in continuous distribution of volatile abundances between 0.6% and 0.05%. The results for K1 reinforce this view. Prior to this study, there was a lack of comets with C_2H_6 abundances between 0.87% and 1.70% (between nearly "average" and "enriched"; Figure 2.7B). While the C_2H_6 abundance in K1 on May 24 was within the range observed to date (due to the higher water production rate in that setting, see Section 2.2 and Table 2.2), on May 22 it was ~1% and fell within the previously unsampled range. This also suggests that the apparent gap for CH_3OH abundances between 0.20% and 1.0% (between "depleted" and close to "average"; Figure 2.7C) may be expected to be "filled in" with additional comet observations.

CH_4 has been sampled in fewer (~ 20) comets, and it appears that a gap remains between C/1999 T1 and the remaining comet population (Figure 2.7D); however, due to the large uncertainty in the T1 CH_4 abundance, the significance of the gap is unclear. CH_4 is difficult to detect, particularly in JFCs, due to lack of sensitivity with available instruments and (especially) the requirement that observable comets have a sufficiently large geocentric Doppler shift to displace cometary emission lines from the (opaque) cores of corresponding telluric absorptions. Clearly, more work is needed to characterize CH_4 in comets, and JFCs in particular.

Examination of Figure 2.7 also shows that the level of enrichment or depletion in a given comet does not necessarily correlate across all molecules sampled. One comet may be enriched in CH_3OH and consistent with normal in HCN (K1 – see red arrows in

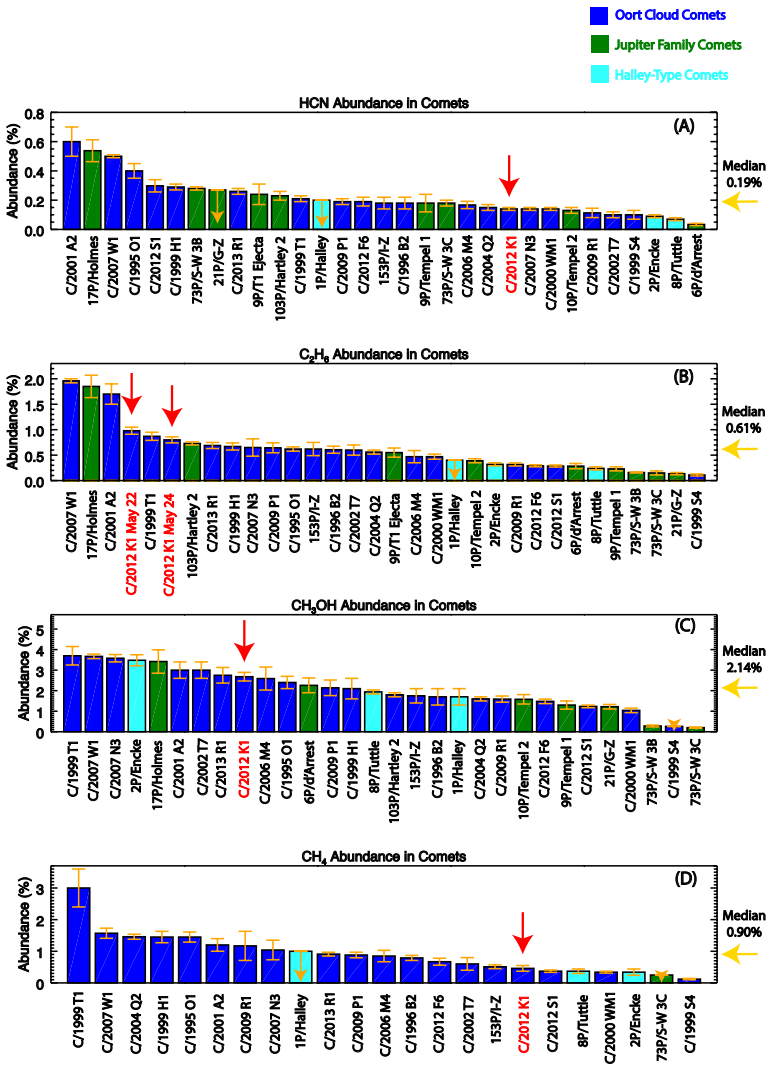

Figure 2.7. Distribution of abundances for selected volatiles in comets as measured in the near-infrared. Abundances of HCN (A), C_2H_6 (B), CH_3OH (C), and CH_4 (D) in comets, arranged in order of abundance for each species. Blue bars represent Oort cloud comets, green bars represent Jupiter-family comets, mint bars represent Halley-type comets, downward orange arrows represent 3σ upper limits, and the golden arrows on the right-hand side show the median abundance for each molecule. C_2H_6 is shown for both dates due to the observed differences in abundances (see Section 2.2 and Table 2.2). K1 is highlighted with a red arrow illustrating that it fills a gap between "average" and "enriched" comets in C_2H_6.

Figure 2.7) while another may be depleted in CH_3OH but not HCN (e.g., 73P/SW 3B), challenging attempts to assign definitive taxonomic classes. In support of this conclusion

is the lack of strong correlation between the abundance of CH_3OH and the other species represented in Figure 2.7. Dello Russo *et al.* (2016a) found correlation coefficients of 0.37, 0.66, and 0.51 between CH_3OH and HCN, C_2H_6, and CH_4, respectively.

There are several unanswered questions that need to be addressed before the distribution of volatile abundances in comets can be understood. First, what is the range of abundances for trace volatiles in comets? Are the currently proposed "taxonomic end-members" (C/2001 A2 on the "enriched" end, and D/1999 S4 on the "depleted" end) truly representative of compositional extremes? On the low abundance end, we are limited by technology and the sensitivity of state-of-the-art techniques. On the upper end, we are limited by the relatively small number of comets measured to date with adequate S/N. Of the $\sim 10^{11}$ cometary nuclei that reside in the Oort cloud (Emel'Yanenko *et al.*, 2007), we have measured primary volatile abundances for only about 40 comets in the near-infrared. For some molecules, most specifically C_2H_2 and OCS, that number is much lower, due principally to lack of sensitivity (in the case of C_2H_2) and/or spectral coverage (in the case of OCS) in "standard" NIRSPEC settings.

However, both areas are expected to be addressed with the availability of a powerful new cross-dispersed spectrograph (iSHELL) at the NASA Infrared Telescope Facility (IRTF; (Rayner *et al.*, 2012, 2016)). Specifically, regarding C_2H_2, iSHELL/IRTF will enable very long on-source integrations, including allowance for daytime observing. Regarding OCS, many lines will be sensed simultaneously with CO and H_2O in a standard iSHELL M-band setting. Conversely, targeting OCS with NIRSPEC requires an additional setting to MWA, one that includes CO lines having higher rotational quantum numbers. For rotational temperatures typically found in comets, these higher-J lines are relatively weaker than the low-J lines included in MWA (e.g., see Figure 4 in Gibb *et al.* (2012)). As the answers to these questions become more clear, one may also ask whether the distribution of

primary volatile abundances in comets is a primordial effect preserved from the cometary formation in the solar nebula, or if instead heterogeneous nuclei, such as the binary comet 67P/Churyumov-Gerasimenko (Rickman *et al.*, 2015) are being sampled.

Once the distribution of volatiles abundances in comets is understood, attempts can be made to interpret the abundance of a given volatile in a comet in terms of the extant conditions during its formation. In principle, this can be accomplished by comparing volatile abundances measured in comets with those of ices as predicted by models of protoplanetary disk midplanes (Drozdovskaya *et al.*, 2016). However, as with adding to the inventory of comet primary volatile abundances, much work remains to be done in improving protoplanetary disk models before firm conclusions can be drawn. Clearly, more studies of the primary volatile compositions of comets are needed to answer these complex questions.

3. A TALE OF "TWO" COMETS: THE PRIMARY VOLATILE COMPOSITION OF COMET 2P/ENCKE ACROSS APPARITIONS AND IMPLICATIONS FOR COMETARY SCIENCE

3.1. COMET 2P/ENCKE

The first quarter of 2017 provided the opportunity to address many pressing matters in cometary science with a highly favorable apparition of the unique ecliptic comet 2P/Encke (hereafter Encke). Encke is known for its weak dust production, asymmetric coma, and one of the shortest orbital periods among known comets (3.3 years). In terms of its dynamical history, Encke is truly unique among comets. In addition to its small perihelion distance (q ~ 0.3 AU), Encke has the smallest known aphelion distance of any comet (4.1 AU), distinguishing it from JFCs for which this is beyond Jupiter's orbit (5.2 AU). Explaining how Encke evolved to its current orbit, along with the fact that it is still an active comet, has proven challenging. Increasingly sophisticated dynamical modeling efforts (Levison *et al.*, 2006) suggest that after becoming decoupled from Jupiter, Encke accumulated a dust mantle and became temporarily inactive. Encke then evolved into the ν_6 secular resonance, causing its perihelion distance to slowly decrease, eventually blowing away its dust mantle, reigniting cometary activity, and dooming Encke to a collision with the Sun in 10^5 – 10^6 years.

The newly commissioned iSHELL spectrograph at the NASA Infrared Telescope Facility (IRTF) was used to characterize the volatile composition of Encke at small R_h (~ 0.4 AU) and at high Δ_{dot} (~ +27 km s^{-1}) on three post-perihelion dates. The excellent sensitivity, large spectral grasp, and daytime observing capabilities of iSHELL allowed for the secure measurement of CO and CH_4, the detection and stringent constraint of OCS

Table 3.1. 2P/Encke observing log and H_2O production rates.

Date (2017)	iSHELL Setting	UT	R_h (AU)	Δ (AU)	Δ_{dot} (km s^{-1})	T_{int} (minutes)	$Q(H_2O)$ (10^{28} s^{-1})
3/21	Lp1	19:52 – 20:54	0.456	0.751	26.87	34	3.53 ± 0.31
	L1	21:53 – 22:28	0.458	0.753	27.10	26	3.51 ± 0.11
3/22	M2	18:52 – 20:01	0.473	0.767	27.15	50	4.14 ± 0.16
3/25	LCS	17:49 – 20:43	0.526	0.814	27.14	96	2.89 ± 0.06
		21:53 – 22:22					

[1] R_h, Δ, and Δ_{dot} are heliocentric distance, geocentric distance, and geocentric velocity, respectively, of 2P/Encke. T_{int} is total integration time on source, and $Q(H_2O)$ is the global water production rate. Seeing increased over the course of the day from $\sim 0.6''$ to $\sim 1.2''$, from $0.6''$ to $\sim 2''$, and from $\sim 1''$ to $1.5''$ on March 21, 22, and 25, respectively. The column burden of atmospheric water vapor (expressed in precipitable millimeters) retrieved in fitting synthetic telluric absorption models to flux standard star continua was 1.7, 1.2, and 1.8 on March 21, March 22, and March 25, respectively.

and C_2H_2, respectively, and the first comprehensive characterization of primary volatile composition in a comet across multiple perihelion passages by comparing to published results from the 2003 apparition (Radeva *et al.*, 2013) – hereafter referred to as RD13.

During its 2017 apparition, Encke reached perihelion on March 10 and was closest to Earth (0.65 AU) on March 17. On UT 2017 March 21, 22, and 25, Encke was observed with the facility high-resolution ($\lambda/\Delta\lambda \sim 40,000$), near-infrared, immersion-grating echelle spectrograph iSHELL (Rayner *et al.*, 2012, 2016) at the 3 m NASA IRTF to characterize its volatile composition. The observing log is shown in Table 3.1.

3.2. RESULTS

Data for comet Encke were analyzed using the procedures described in Section 1.6.1. Results specific to comet Encke are discussed in turn below.

3.2.1. Growth Factors. Growth factors were determined for both the gas and the dust when signal-to-noise ratio (S/N) was sufficiently high (i.e., only for water and OH prompt emission, henceforth denoted OH*). Because OH* is well established as a reliable

proxy for the production and spatial distribution of its parent, H_2O, (Bonev and Mumma, 2006; Bonev *et al.*, 2006; Mumma *et al.*, 2001), these two species provided similar GFs (see Table 3.2).

It is noteworthy that the Q-curve methodology assumes a spherically symmetric coma and constant gas outflow speed. Although this spherically symmetric approach does not reproduce the aspherical and asymmetric coma of Encke (see Dorman *et al.* (2013); Ihalawela *et al.* (2011) and refs. therein), the calculated abundances (relative to water) should be accurate, since it was established that "symmetrizing" Q_{global} by averaging values to either side of the nucleus provides a reliable measure of total molecular production rate (Xie and Mumma, 1996a,b). Furthermore, any over (or under) estimate in volatile production rates introduced by the model will apply to all volatiles with similar spatial distributions and cancel out in determining relative abundances.

3.2.2. Spatial Profiles. Spatial profiles of emission were extracted for H_2O, OH*, CO, and CH_3OH in Encke. Figure 3.1A shows spatial profiles of co-measured emissions in Encke for OH*, CH_3OH, and dust on March 21. Figure 3.1B shows the same for H_2O, CO, and dust on March 22. The CO and CH_3OH profiles were smoothed by 3 pixels due to low S/N. Emission from dust on both dates show Encke's peculiar sunward-facing fan, which has been consistently observed during Encke's perihelion passages for over a century (Sekanina, 1988a,b). While low S/N prevents definitive conclusions, Figure 3.1A suggests that the CH_3OH emission may have peaked sunward of the OH* emission on March 21, and Figure 3.1B suggests that the CO emission may have been narrower than that for the dust, whereas the H_2O emission was broader.

3.2.3. Rotational Temperature. Consistent rotational temperatures for multiple molecules were found on all dates (including H_2O). The rotational temperature (T_{rot}) for H_2O was well-constrained and was consistent (within 1σ uncertainty) on all dates (being 62^{+2}_{-3} K, 67 ± 6 K, and 63 ± 2 K on March 21, 22, and 25, respectively). Rotational temperatures, production rates, and mixing ratios for all sampled molecules are listed in

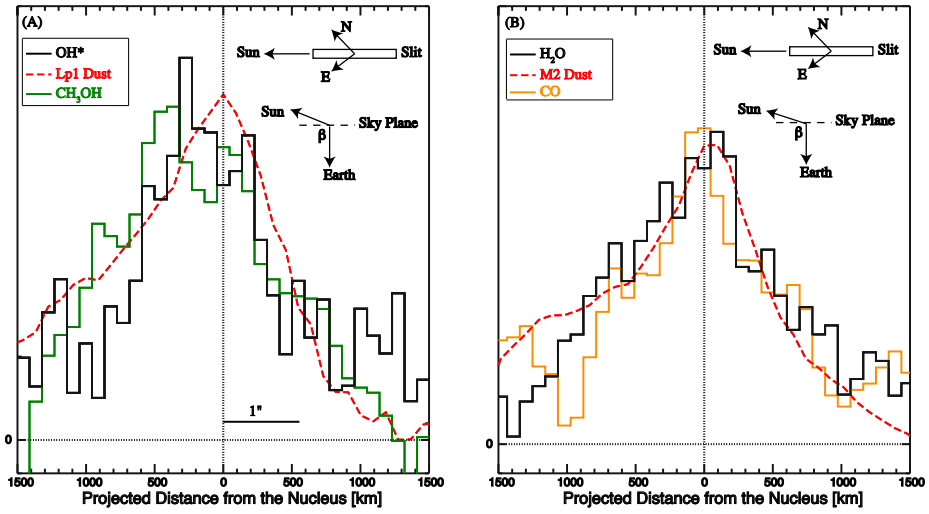

Figure 3.1. Coma spatial distributions of volatiles in 2P/Encke. A. Spatial profiles of co-measured emissions in Encke for OH* (prompt emission, black), CH_3OH (green) and dust (red) on UT 2017 March 21. The slit was oriented along the projected Sun-comet line (position angle 234°), with the Sun-facing direction to the left as indicated. Also shown is the Sun-comet-Earth angle (phase angle, β) of 108°, so largely in the sky plane. The horizontal bar indicating 1″ corresponds to a projected distance of approximately 550 km at the geocentric distance of Encke. B. Spatial profiles of co-measured emissions for H_2O (black), CO (orange), and dust (red) on UT 2017 March 22. The CO and CH_3OH profiles have been smoothed by 3 pixels. The observing geometry on March 22 was similar to that of March 21, with a position angle of 234°and a phase angle of 104°.

Table 3.2. When a rotational temperature for a particular molecule could not be retrieved, the rotational temperature from simultaneously measured H_2O within the same setting was assumed.

3.2.4. Secure Detections of CO and CH_4. The detections of CO and CH_4 in Encke are particularly notable for two reasons: (1) The paucity of measurements of CO and CH_4 in ecliptic comets in general, and (2) the measurement of these hypervolatiles in the most thermally-evolved comet known. Of all primary volatiles systematically measured in comets, these two molecules are most sensitive to thermal processing, but as noted earlier (Section 1.4), they are also among the most difficult to sample from the ground due to lack of sensitivity and/or adequate geocentric velocity. Encke's excellent geocentric velocity

Table 3.2. Volatile composition of 2P/Encke.

Setting	Molecule	T_{rot}[(1)] (K)	Growth Factor[(2)]	Q[(3)] (10^{25} mol s^{-1})	Q_x/Q_{H2O} (%)
2017 March 21, R_h = 0.456 AU, Δ = 0.757 AU, Δ_{dot} = 27.0 km s^{-1}					
L1	H_2O	68^{+2}_{-3}	2.04 ± 0.23	3505 ± 111	100
	HCN	78^{+15}_{-12}	(2.04)	6.20 ± 0.50	0.18 ± 0.02
		(68)	(2.04)	5.89 ± 0.47	0.17 ± 0.02
LP1	C_2H_6	(68)	(1.82)	1.29 ± 0.14	0.037 ± 0.005
	CH_3OH	52^{+7}_{-6}	(1.82)	27.5 ± 1.5	0.78 ± 0.08
		(68)		30.7 ± 1.8	0.87 ± 0.09
	CH_4	(68)	(1.82)	3.74 ± 0.28	0.11 ± 0.01
	H_2CO	(68)	(1.82)	9.42 ± 1.05	0.27 ± 0.04
	OH*	(68)	1.82 ± 0.19	3534 ± 313	100
2017 March 22, R_h = 0.473 AU, Δ = 0.767 AU, Δ_{dot} = 27.1 km s^{-1}					
M2	H_2O	67 ± 6	2.25 ± 0.11	4141 ± 158	100
	CO	(67)	(2.25)	17.9 ± 1.5	0.43 ± 0.04
	OCS	(67)	(2.25)	2.65 ± 0.55	0.06 ± 0.01
2017 March 25, R_h = 0.526 AU, Δ = 0.814 AU, Δ_{dot} = 27.2 km s^{-1}					
LCS[(4)]	H_2O	63 ± 2	2.02 ± 0.20	2890 ± 62.	100
	C_2H_2	(63)	(2.02)	<0.2 (3σ)	<0.007 (3σ)
	HCN	66^{+16}_{-11}	(2.02)	3.23 ± 0.26	0.11 ± 0.01
		(63)	(2.02)	3.20 ± 0.25	0.11 ± 0.01
	NH_3	(63)	(2.02)	17.8 ± 1.1	0.61 ± 0.04
	NH_2	(63)	(2.02)	6.81 ± 1.01	0.23 ± 0.03

[1] Rotational temperature. Values in parentheses are assumed.
[2] Growth factor. Values in parentheses are assumed.
[3] Global production rate. Errors in production rate include line-by-line deviation between modeled and observed intensities and photon noise (see Bonev (2005); Bonev *et al.* (2007); Dello Russo *et al.* (2004)).
[4] Custom L-band setting with iSHELL's user-defined cross disperser position abilities, spanning 2.9 – 3.1 μm.

(> 27 km s^{-1} for all dates) allowed for firm detections of both species. Each hypervolatile has been detected in less than 10 ecliptic comets (most below the 5σ level), making the measurements in Encke a critical component for establishing statistics for these species in ecliptic comets, and determining the importance of natal versus evolutionary effects

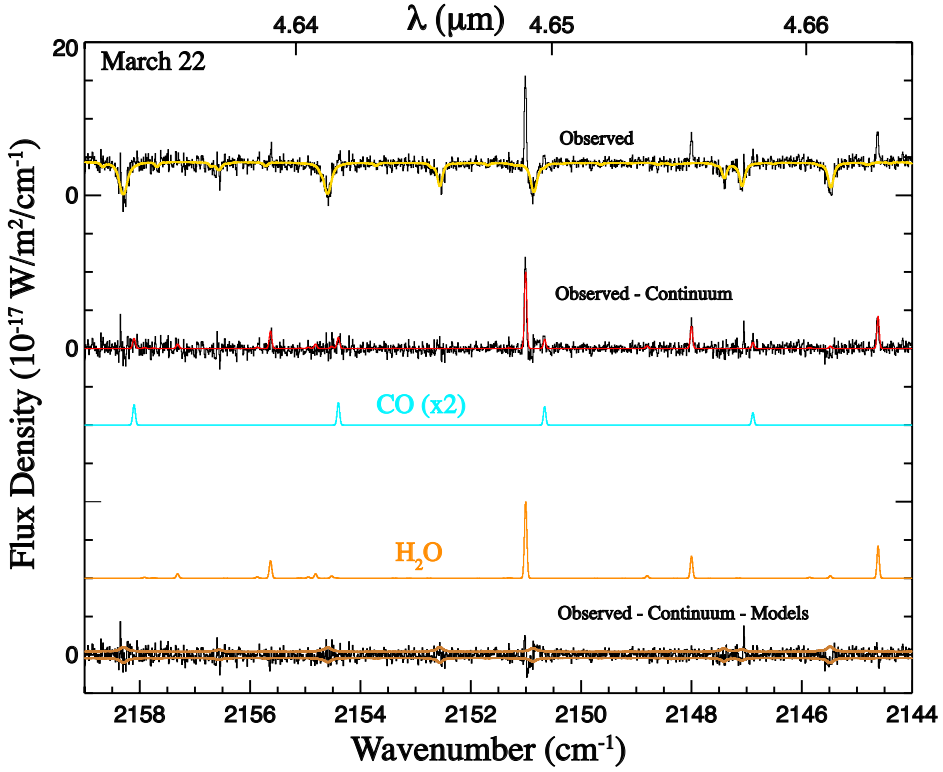

Figure 3.2. Extracted spectra showing detections of CO and H_2O on UT 2017 March 22 in 2P/Encke.

on present comet volatile composition. Figures 3.2 and 3.3 show clear CO, H_2O, and CN emissions in Encke superimposed on the cometary continuum, and Figures 3.4 and 3.5 show corresponding detections for CH_4, C_2H_6, and CH_3OH, along with (co-measured) OH*.

3.2.5. Other Volatiles. In the 3 μm region, emission from the nitrogen-bearing species HCN (Figure 3.6) was detected, as well as from NH_3 (Figure 3.7) for the first time in Encke. C_2H_2 was stringently constrained (Figure 3.6), with a (3σ) upper limit (<0.007% relative to H_2O; Table 3.2) that is consistent with (but well below) that reported by RD13 (<0.08%-0.10%). Figure 3.8 shows Order 179 of the iSHELL L filter, which samples H_2O lines spanning a broad range of rotational energies and thus is particularly diagnostic of T_{rot}. OCS was also detected with signal-to-noise exceeding 4σ, representing

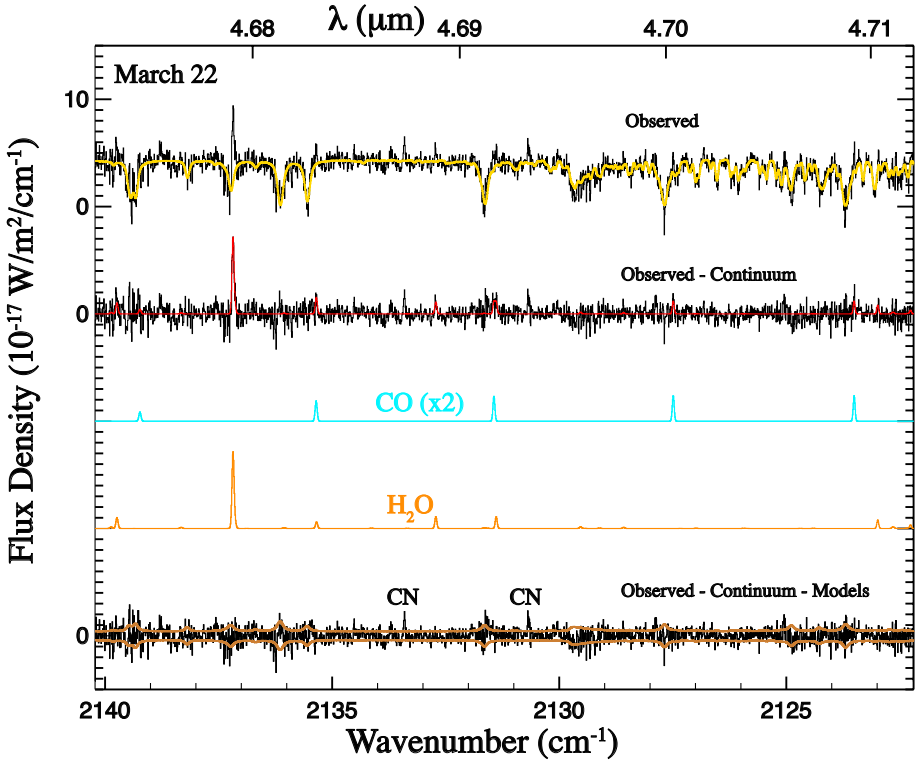

Figure 3.3. Extracted spectra showing detections of CO, CN, and H_2O on UT 2017 March 22 in 2P/Encke.

the first reported value for its abundance in Encke (Figure 3.9). CN emissions in Encke were strong (Figure 3.3,3.9) consistent with that seen in other comets measured at small R_h (e.g., Dello Russo *et al.* (2016a)). Analysis of CN in Encke is the subject of a future paper.

In the LP1 setting, C_2H_6 ν_7 band emission, together with CH_3OH ν_2 band and CH_4 ν_3 P-branch lines, was detected simultaneously in Orders 154 and 155 (Figure 3.5). CH_3OH ν_3 band, H_2CO ν_5 band, H_2CO ν_1 band (Figure 3.10), and CH_4 ν_3 R-branch lines (Figure 3.4) were also measured. These were sampled simultaneously with OH* in five orders. The value of $Q(H_2O)$ so determined was used in establishing mixing ratios (i.e., abundances relative to H_2O) for C_2H_6, CH_3OH, CH_4, and H_2CO.

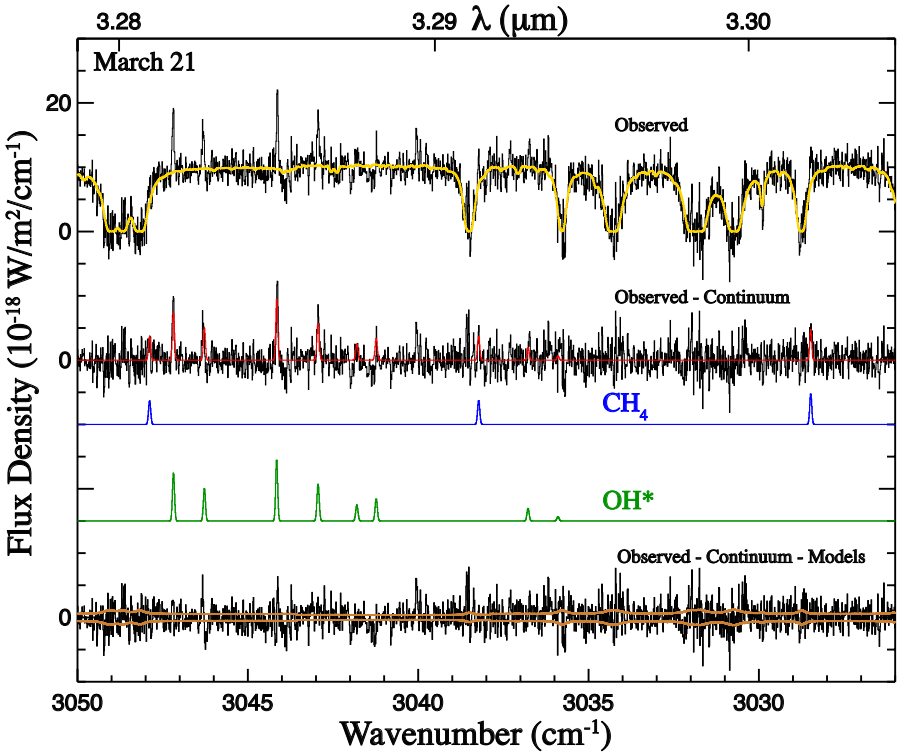

Figure 3.4. Extracted spectra showing detections of CH_4 and OH* on UT 2017 March 21 in 2P/Encke.

3.3. COMPARISONS WITH 2003 AND OTHER COMETS MEASURED

The 2017 apparition of Encke provided an opportunity to conduct the first comprehensive comparison of primary volatile composition through multiple perihelion passages, thereby allowing pressing questions in cometary science to be addressed. These include testing possible evolutionary and/or heliocentric distance effects on volatile production, and also examining asymmetries in volatile production about perihelion. Each of these topics will be discussed in turn, and Encke will be placed in the context of other comets observed to date.

3.3.1. Dramatic Compositional Differences Compared to the 2003 Apparition. Dramatic differences were observed in the primary volatile composition of Encke compared to the 2003 apparition. RD13 characterized the primary volatile composition of Encke in

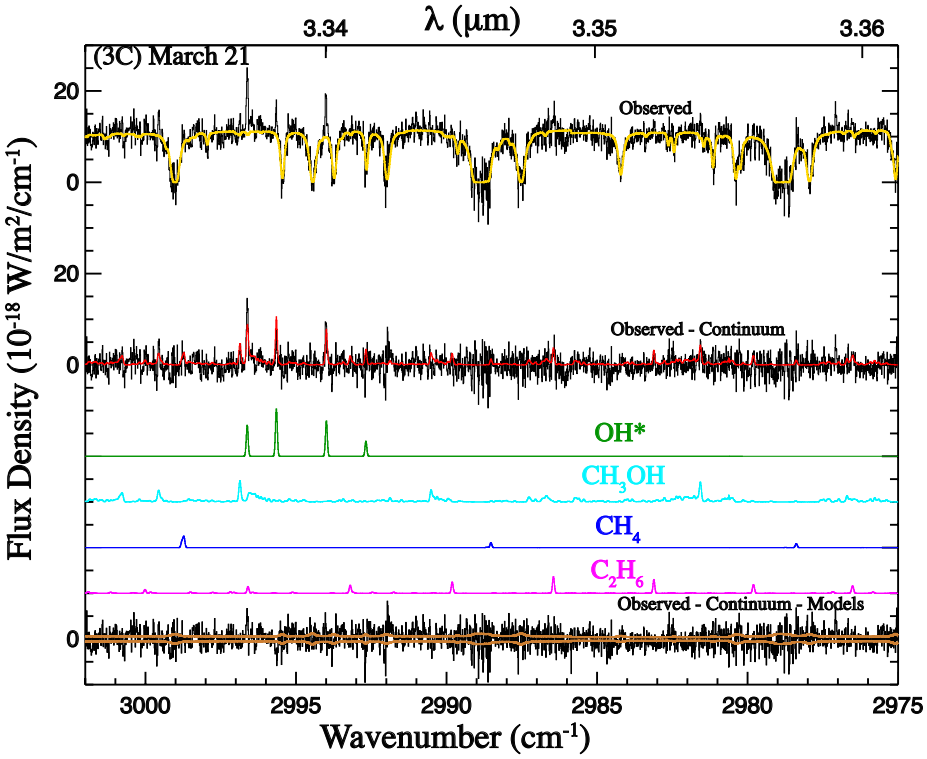

Figure 3.5. Extracted spectra showing detections of CH_4, C_2H_6, CH_3OH, and OH* on UT 2017 March 21 in 2P/Encke.

2003 at $R_h \sim 1.2$ AU pre-perihelion using NIRSPEC at the W. M. Keck Observatory. Table 3.3 shows a comparison from 2003 and 2017. Figure 3.11 provides the same comparison graphically, along with near-infrared measurements of each volatile in comets to date and their respective mean value among comets (Dello Russo *et al.*, 2016a; DiSanti *et al.*, 2017). The contrast between the two apparitions is obvious. Figure 3.11 illustrates that:

1. CH_3OH (0.87%), C_2H_6 (0.037%), and CH_4 (0.11%) show clear depletion, both with respect to the 2003 apparition as well as among measured comets. The 2003 measurement of CH_3OH (3.48%) placed Encke among the most CH_3OH-enriched comets observed to date, whereas the 2017 measurement is clearly depleted. Similarly the C_2H_6 mixing ratio (depleted by a factor of 10 compared to 2003) is the lowest measured in any comet to date.

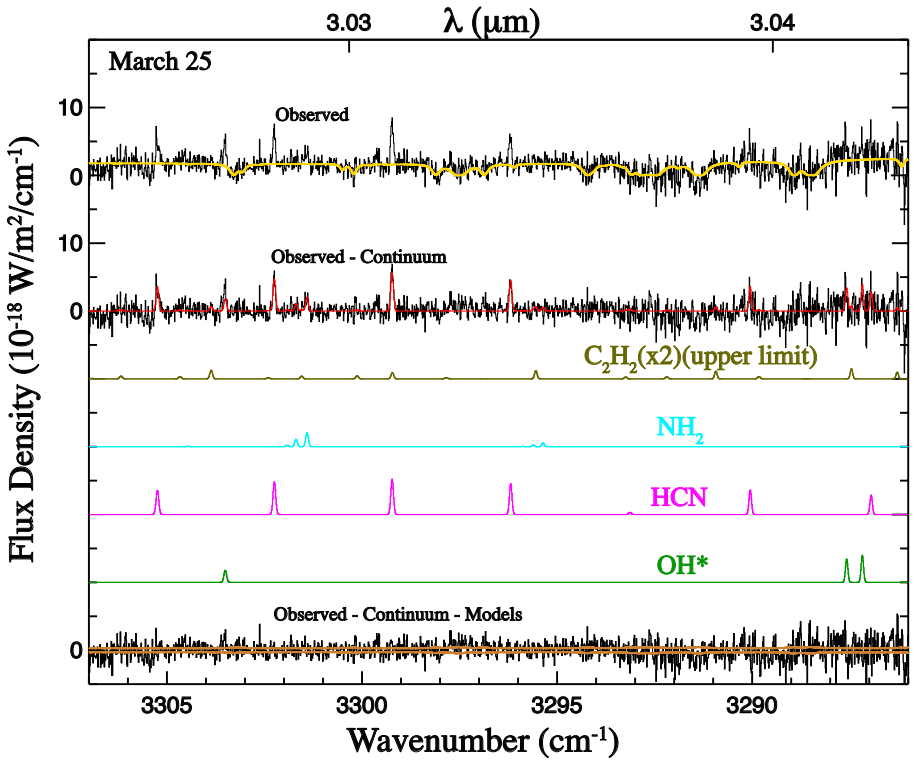

Figure 3.6. Extracted spectra showing detections of of HCN, NH_2, and OH* on UT 2017 March 25 in Encke.

2. H_2CO (0.27%) and HCN (0.12%) are enriched compared to their respective 2003 abundances. H_2CO is strongly enriched (by greater than a factor of 2) and consistent with the mean value among comets, and HCN is moderately enriched (by less than a factor of 2) compared to 2003 but is significantly less than its mean value.

3. NH_3 was not reported in RD13, but its value in 2017 (0.61%) is consistent with its mean. The mixing ratio for CO (0.43%) and the (3σ) upper limit for C_2H_2 (< 0.007%) are both consistent with upper limits reported for 2003, and both are strongly depleted compared to their respective mean values.

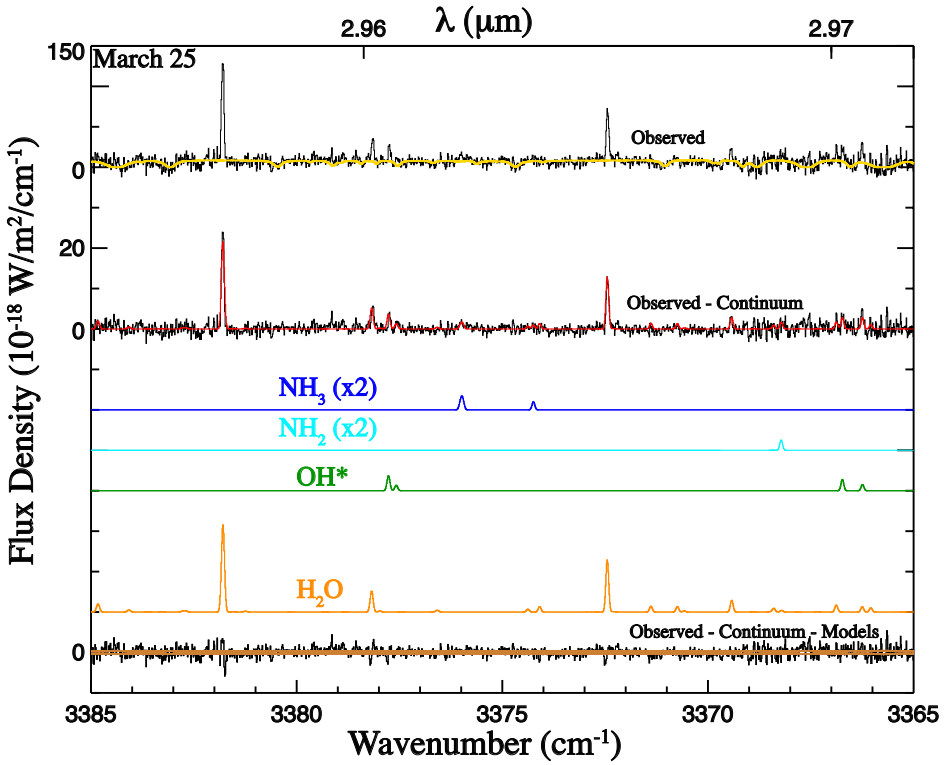

Figure 3.7. Extracted spectra showing detections of of NH_3, NH_2, H_2O, and OH* on UT 2017 March 25 in Encke.

3.3.2. Interpreting Differences in the Volatile Content of Encke Across Apparitions. The most striking feature of the primary volatile composition of Encke during the 2017 apparition is its difference from that reported for 2003. Understanding the cause(s) of these differences – and their significance – is crucial to tying observed primary volatile compositions to formative conditions in the solar nebula. Four possible explanations are examined (in turn) for these differences, each of which may have contributed simultaneously and to varying degrees: (1) dependence of volatile production on heliocentric distance, (2) evolutionary processing of a heterogeneous nucleus, (3) pre-/post-perihelion asymmetries in volatile mixing ratios, and (4) viewing geometry effects.

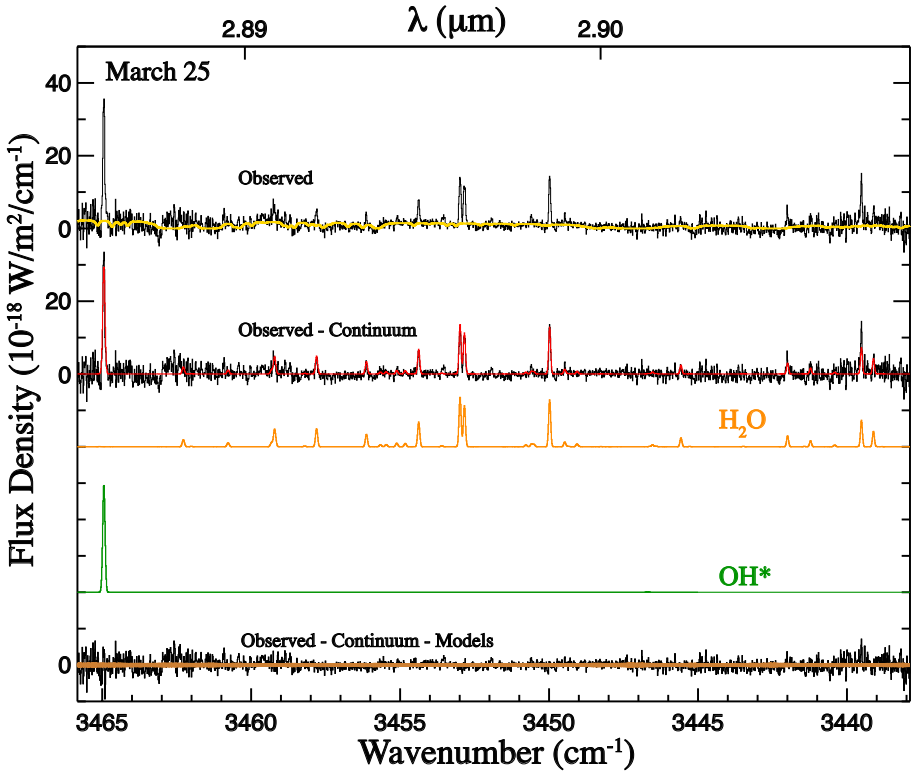

Figure 3.8. Extracted spectra showing detections of of H_2O and OH*, as well as determination of T_{rot}, on UT 2017 March 25 in Encke.

3.3.2.1. Dependence of volatile production on heliocentric distance. As noted earlier, near-infrared spectroscopic studies of comets spanning large ranges of heliocentric distances during a given apparition are sparse. Provided that the primary volatile composition of the coma accurately reflects the composition of the ices in the nucleus once sublimation of all volatiles has been completely activated, then mixing ratios of primary volatiles in comet comae should remain relatively constant once H_2O controls the overall activity. Comets observed to date suggest that this is true in general, although some primary volatiles (NH_3, H_2CO, and C_2H_2) and fragment species (CN and NH_2) show a trend towards enhanced production at $R_h < 0.8$ AU (possibly due to release from grains; e.g., see Dello Russo *et al.* (2016a)). Measurements at radio wavelengths have also shown that H_2CO may originate from extended sources (e.g., Cordiner *et al.* (2014)) and clearly shows

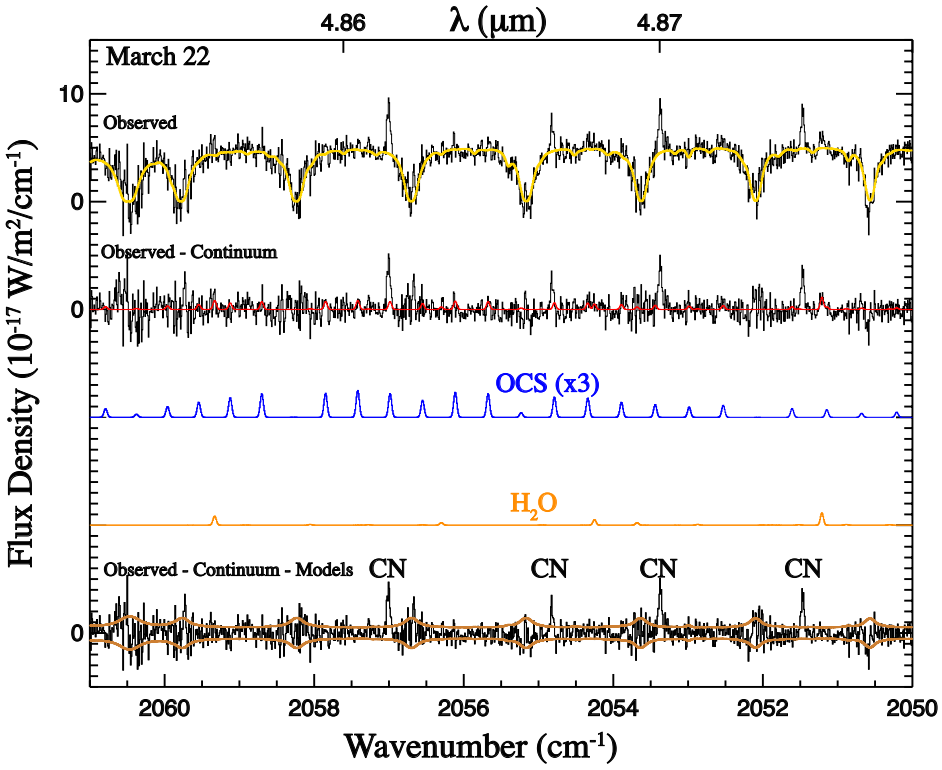

Figure 3.9. Extracted spectra showing detections of of OCS, H_2O, and CN on UT 2017 March 22 in Encke.

increasing abundances with decreasing R_h, possibly due to thermal degradation of polymers (Fray *et al.*, 2006). Although it was not possible to extract spatial profiles of H_2CO emission with adequate S/N to test for the presence of an extended source, the enrichment of H_2CO in 2017 (0.27%, $R_h \sim 0.4$ AU) compared to 2003 (<0.13%, $R_h \sim 1.2$ AU) suggests that this may be the case for H_2CO in Encke.

DiSanti *et al.* (2016) found that HCN became enriched in comet D/2012 S1 (ISON) at small R_h relative to measurements at larger R_h, increasing from 0.07% at $R_h = 0.82$ AU to 0.26% at $R_h = 0.43$ AU. A similar trend as observed in HCN with Encke in 2017 (0.17%, $R_h = 0.45$ AU on March 21) compared to 2003 (0.09%, $R_h \sim 1.2$ AU). However, HCN in Encke decreased from 0.17% to 0.11% on March 25 at $R_h = 0.53$ AU. Given the nearly four-fold increase in HCN in ISON between $R_h = 0.83$ and 0.46 AU, it is possible that the

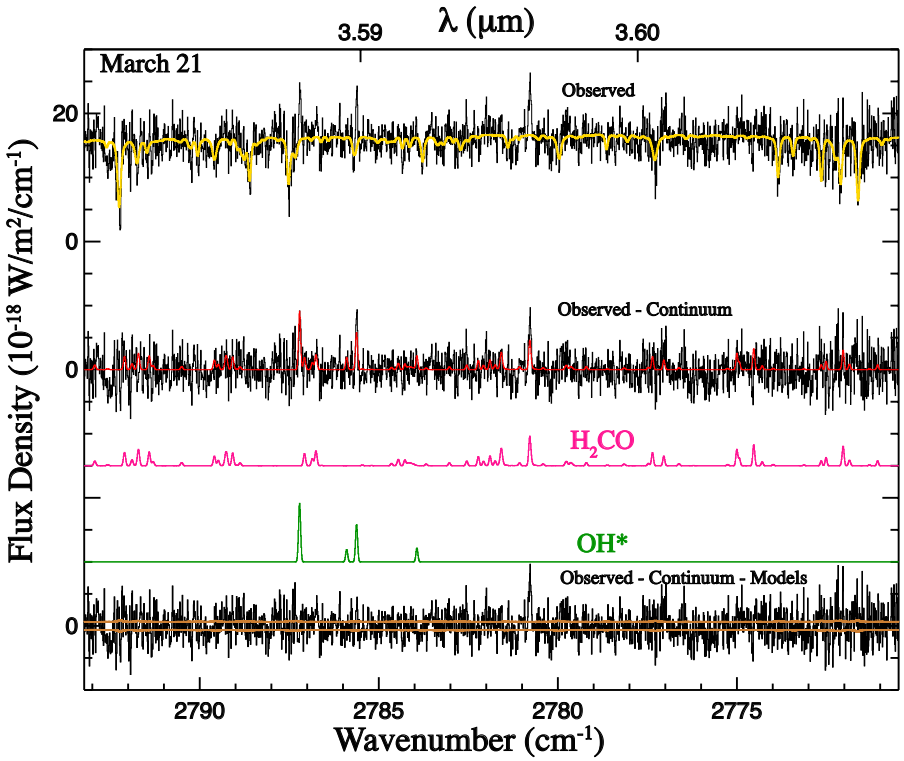

Figure 3.10. Extracted spectra showing detections of of H_2CO and OH* on UT 2017 March 21 in Encke.

decrease in HCN in Encke from March 21 to March 25 may also be explained by its receding 0.08 AU from the Sun. However, this does not explain the severe depletion of CH_3OH and C_2H_6 in 2017 compared to 2003, leaving the question unresolved. Clearly, further serial measurements of Encke over a range of R_h are needed to distinguish the possible dependence of its volatile composition on heliocentric distance from other factors.

3.3.2.2. Potential evolutionary processing of a heterogeneous nucleus. The near-infrared measurements in this study do not resolve the nucleus, and the few comets for which the structure of the nucleus is known are those visited by spacecraft. The Rosetta mission found a heterogeneous nucleus for comet 67P/Churyumov-Gerasimenko that is likely a contact binary (Rickman *et al.*, 2015). In Encke, it is possible that compositional differences within a heterogeneous nucleus are being viewed. This suggests two possibilities

Table 3.3. Primary volatile abundances in 2P/Encke across apparitions.

Molecule	2017 Apparition[(1)] %, relative to H_2O	2003 Apparition[(2)] %, relative to H_2O	Mean Value among Comets[3]
C_2H_6	0.037 ± 0.005	0.32 ± 0.03	0.55 ± 0.08
CH_3OH	0.87 ± 0.09	3.48 ± 0.27	2.06 ± 0.20
CH_4	0.11 ± 0.01	0.34 ± 0.10	0.78 ± 0.09
CO	0.43 ± 0.04	<1.77	5.2 ± 1.3
HCN	0.12 ± 0.01	0.09 ± 0.01	0.21 ± 0.02
NH_3	0.61 ± 0.07	···	0.80 ± 0.20
H_2CO	0.27 ± 0.04	<0.13	0.31 ± 0.06
C_2H_2	<0.007	<0.08	0.13 ± 0.02
OCS	0.06 ± 0.01	···	···

[1] This work. Abundances are given as weighted averages for molecules detected on multiple dates (HCN). Upper limits for non-detected species are 3σ. In all cases values are expressed relative to simultaneously measured H_2O.

[2] Abundances taken from Radeva *et al.* (2013).

[3] Mean values and 1σ uncertainties among measured comets taken from Dello Russo *et al.* (2016a). No value is listed for OCS due to the paucity of measurements at near-infrared wavelengths

– (1) a compositionally different area dominated its activity in 2017 compared to 2003 (seasonal differences), or (2) subsequent perihelion passages have exhausted material that was active during 2003, and new material within the nucleus that was covered during the 2003 apparition was exposed in 2017 (evolutionary changes). In light of the measurements of compositional diversity from 2003 to 2017, it is noteworthy that pre-perihelion optical observations of Encke from McDonald Observatory during 2003 and 2017 show no remarkable changes in composition (A. McKay 2018, personal communication). This suggests that seasonal effects may dominate evolutionary changes in the bulk composition of Encke.

3.3.2.3. Asymmetry in volatile mixing ratios about perihelion due to seasonal effects. Another possible explanation for the observed differences in Encke's composition is asymmetry in volatile mixing ratios about perihelion, in which distinct, chemically hetero-

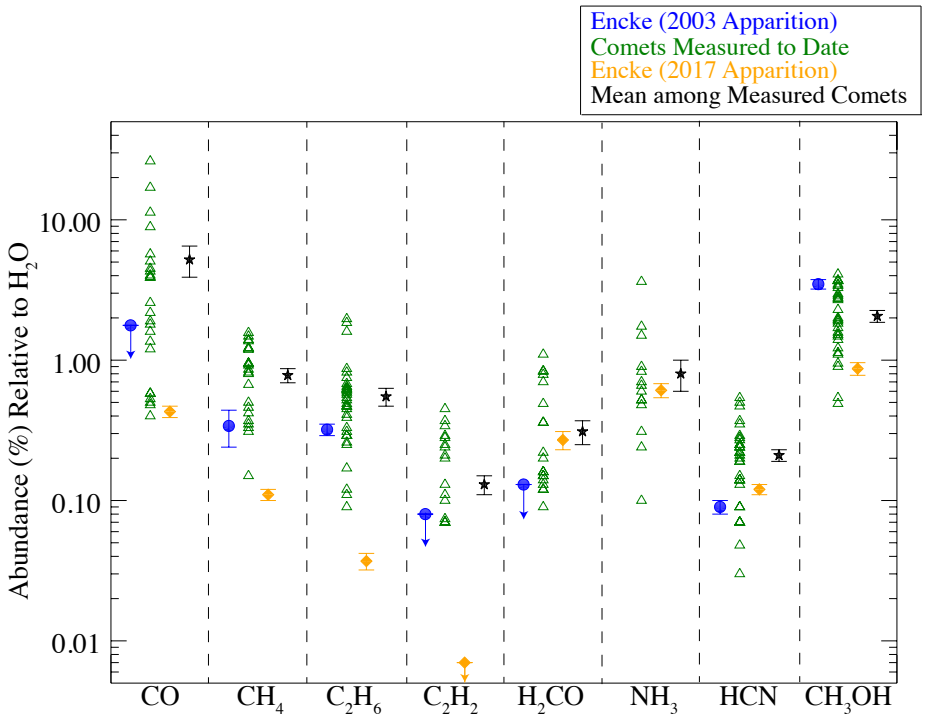

Figure 3.11. Comparison of mixing ratios (%, relative to H_2O) of primary volatiles sampled in Encke during the 2003 (blue, Radeva *et al.* (2013)) and 2017 (orange, Roth *et al.* (2018)) perihelion passages, as well as near-infrared measurements of each volatile in comets to date (green) and their respective mean values (black, Dello Russo *et al.* (2016a); DiSanti *et al.* (2017)). Error bars indicate measurements, whereas downward arrows indicate 3σ upper limits.

geneous sources on the nucleus dominate volatile release due to seasonal effects. Although observing time was granted to investigate such asymmetries in Encke with iSHELL, the pre-perihelion dates were completely weathered out.

Asymmetry in mixing ratios of fragment species about perihelion has been reported in the literature for Encke. A'Hearn *et al.* (1985) found that OH (and by proxy, water) production was symmetric about perihelion, whereas C_2, C_3, and CN production was much lower post-perihelion vs. pre-perihelion. If this asymmetry in fragment species production has persisted to the present day, then one might expect that the post-perihelion observations

in this work (obtained < 20 days post-perihelion) should show depletion in potential parent species for these fragments compared to the observations reported in RD13 (obtained > 30 days pre-perihelion). Although direct comparisons between mixing ratios of primary volatile and fragment species are difficult owing to the complicated lineage of fragment species (e.g., multiple molecules, dust grain sources), the results support this hypothesis, with the important exceptions of HCN and H_2CO. As noted earlier, the abundance ratios HCN/H_2O and H_2CO/H_2O are enriched compared to that reported in RD13, perhaps due to additional sources becoming active at the small heliocentric distances of the observations.

Non-uniform volatile mixing ratios have been observed in other comets, perhaps most notably during the Rosetta mission to comet 67P/Churyumov-Gerasimenko. At comet 67P/C-G, Rosetta found that mixing ratios of CO and CO_2 in the coma varied due to seasonal effects on the nucleus (Hässig *et al.*, 2015). Furthermore, variation in volatile mixing ratios was found on smaller timescales, with some volatiles (such as CH_4) showing diurnal variations that differed from those for other volatiles, such as CO and C_2H_6 (Bockelée-Morvan *et al.*, 2016; Fink *et al.*, 2016; Luspay-Kuti *et al.*, 2015).

At comet 103P/Hartley 2, EPOXI/DIXI revealed a comet with distinct sources of outgassing on the nucleus. Strong CO_2 emission from the smaller lobe dragged icy grains along into the coma, from which the ices sublimed and added to its gas content. In contrast, activity in the waist region was dominated by direct release of water gas (A'Hearn *et al.*, 2011; Protopapa *et al.*, 2014). Despite the heterogeneous outgassing at 103P/Hartley 2, ground-based observations showed that mixing ratios of trace species in the coma remained relatively constant (Dello Russo *et al.*, 2011; Mumma *et al.*, 2011).

Additionally, non-uniform mixing ratios of CO/H_2O were observed in comet C/2009 P1 (Garradd) by both ground-based studies (McKay *et al.*, 2015) and space-based studies from the High Resolution Instrument Infrared Spectrometer aboard the *Deep Impact Flyby* spacecraft (Feaga *et al.*, 2014). In C/2009 P1, H_2O production rates traced the predicted

heliocentric dependence, rising and then falling near perihelion. However, CO production increased monotonically throughout the apparition, continuing to rise long after perihelion, perhaps due to seasonal effects on the nucleus (Bodewits *et al.*, 2014; McKay *et al.*, 2015).

Seasonal effects have been proposed to interpret imaging and photometric studies of Encke's coma (e.g., Ferrin (2008); Sekanina (1988a) and references therein; Farnham (2009)), which suggest that (at least) two distinct nucleus sources receive seasonal illumination and account for outgassing in Encke during different portions of its orbit. However, there is debate regarding exactly when a given source activates and begins to dominate outgassing. Unfortunately, these observations are unable to trace the measured composition of the gases to individual source regions, and thus further test for compositional heterogeneity.

Perhaps the most compelling evidence linking the difference in primary volatile composition to the proposed existence of heterogeneous sources on the nucleus is the dramatic depletion of the least volatile trace species, CH_3OH, measured in Encke. RD13 reported $CH_3OH = 3.48 \pm 0.27\%$ during the 2003 apparition, making Encke one of the most highly CH_3OH-enriched comets observed in the near-infrared. In contrast, the measured 2017 mixing ratio ($CH_3OH/H_2O = 0.87 \pm 0.09\%$) places Encke decisively among CH_3OH-depleted comets (see Figure 3.11 and Table 3.3). Combined with observed asymmetries in fragment species, the lack of bulk compositional changes seen at other wavelengths, and the observational evidence for seasonal effects governing outgassing in Encke, the "switch" from a highly CH_3OH-enriched comet to a CH_3OH-depleted comet (and other compositional differences observed in 2017 compared to 2003), may be explained by a combination of chemically heterogeneous nucleus sources and seasonal effects on Encke. A contribution from additional sources activated at small R_h also cannot be ruled out, as volatiles that have tended to show increased abundances or emission intensities at small R_h (H_2CO, NH_3, NH_2, and CN) are generally enhanced compared to other detected species in Encke in 2017.

3.3.2.4. Consideration of viewing geometry. Encke has displayed an aspherical and asymmetric coma in almost every recorded apparition since 1896 (Sekanina, 1988a,b). Its unusual coma morphology, combined with the possibility that different sources on the nucleus may account for outgassing during different portions of its orbit, make considerations of observing geometry important when interpreting results of ground-based composition studies and comparing across apparitions. The observations in this work may have sampled a dramatically different projection of the non-uniform coma into the plane of the sky than those reported in RD13. In any case, the differences in its measured volatile composition between 2003 and 2017 are pronounced.

In addition, Encke's rotation period ($\sim$ 11 hours; Fernandez *et al.* (2005); Lowry and Weissman (2007); Woodney *et al.* (2007)) is important to consider. The longest observations of Encke on March 25 (UT 17:49 – 22:22) comprised $\sim$ 1/3 of a complete rotation, so it is possible that active sites rotated into or out of view during the course of both the observations reported here as well as those from 2003. These (possible) rotational effects may explain the decrease in HCN in Encke from 0.17% on March 21 to 0.11% on March 25. Analysis of time series of ground-based molecular spectra obtained with IRAM and CSO of 103P/Hartley 2 found that the varying illumination of chemically heterogeneous regions on the nucleus due to rotation caused significant changes in volatile release, creating variations on timescales of hours to days (Boissier *et al.*, 2014; Drahus *et al.*, 2012). However, despite these strong rotational effects observed at radio wavelengths, mixing ratios of primary volatiles derived from ground-based near-infrared measurements of the bulk coma remained relatively constant (Dello Russo *et al.*, 2011; Mumma *et al.*, 2011).

A search for similar short timescale variability was conducted in Encke by comparing derived HCN/H_2O in a time series of spectral extracts. Each spectral extract represented 8 minutes on-source integration time, and the entire time series spanned three hours of clock time. No evidence was found for statistically significant variation in HCN/H_2O during this

time series; however, as noted earlier, this represents less than 1/3 of a complete rotation period for Encke. Thus, further measurements are needed to quantify how much (if any) impact these effects had on calculated mixing ratios during each apparition of Encke.

3.3.2.5. Comparison of primary volatile mixing ratios with photodissociation products. An important task in cometary science is relating measured abundances of photodissociation products (i.e., fragment species) found in optical studies to potential parent volatiles. This is a challenging endeavor, because a given fragment species can have several possible parents. In contrast, near-infrared studies of primary volatiles suffer no such difficulty. Comparison of fragment species mixing ratios in the optical to near-infrared measurements of primary (parent) volatiles is one way to test parent-daughter relationships. In particular, one can compare the ratios C_2/OH, CN/OH, and NH/OH to the mixing ratios of C_2H_2/H_2O, HCN/H_2O, and NH_3/H_2O, respectively. Although this is an admittedly simplistic comparison, one can infer whether the mixing ratios of these primary volatiles can account for those of fragment species found in Encke. Unfortunately, the majority of the published data for Encke is taken from pre-perihelion observations. This adds an additional layer of uncertainty given its asymmetric behavior of volatile mixing ratios about perihelion observed at optical wavelengths. Additionally, with the exception of the NH_2/H_2O and NH_3/H_2O measurements from this work, the observations of the fragment species in this comparison were not taken simultaneously with those of the primary species. Thus, each of the processes mentioned in Section 3.3.2 may affect the comparisons; however, they are still informative.

Table 3.4 compares mixing ratios of primary volatiles to those of fragment species in Encke for several apparitions. The data are divided into pre- and post-perihelion observations for clarity. Note that the most direct comparisons between primary volatile and fragment species in Encke are those reported in RD13 to published pre-perihelion fragment species mixing ratios, and the mixing ratios reported in Roth *et al.* (2018) to the post-perihelion fragment species mixing ratios reported in A'Hearn *et al.* (1985). Since

Table 3.4. Comparison of primary volatile and fragment species mixing ratios in 2P/Encke.

Pre-perihelion		Post-perihelion	
$\log\left[\frac{Q(CN)}{Q(OH)}\right]$	$\log\left[\frac{Q(HCN)}{Q(H_2O)}\right]$	$\log\left[\frac{Q(CN)}{Q(OH)}\right]$	$\log\left[\frac{Q(HCN)}{Q(H_2O)}\right]$
-2.18[a]	-3.04 ± 0.11[b]	-2.54[c]	-2.91 ± 0.08[d]
-2.04 ± 0.44[e]			
$\log\left[\frac{Q(C_2)}{Q(OH)}\right]$	$\log\left[\frac{Q(C_2H_2)}{Q(H_2O)}\right]$	$\log\left[\frac{Q(C_2)}{Q(OH)}\right]$	$\log\left[\frac{Q(C_2H_2)}{Q(H_2O)}\right]$
-2.36[a]	<-3.09[b]	<-2.76[c]	<-4.15[d]
-2.23 ± 0.03[f]			
$\log\left[\frac{Q(NH)}{Q(OH)}\right]$	$\log\left[\frac{Q(NH_3)}{Q(H_2O)}\right]$	$\log\left[\frac{Q(NH_2)}{Q(H_2O)}\right]$	$\log\left[\frac{Q(NH_3)}{Q(H_2O)}\right]$
-2.25 ± 0.03[f]	–	-2.62 ± 0.13[d]	-2.21±0.07[d]

[a] A'Hearn *et al.* (1985). Measurements acquired at R_h = 0.9 AU during the 1984 apparition.
[b] Radeva *et al.* (2013). Measurements acquired at R_h = 1.2 AU during the 2003 apparition.
[c] A'Hearn *et al.* (1985). Measurements acquired at R_h = 0.62 AU during the 1984 apparition.
[d] Roth *et al.* (2018). Measurements acquired at R_h = 0.4 AU during the 2017 apparition.
[e] Ihalawela *et al.* (2011). Measurements acquired at R_h = 1.4 AU during the 2003 apparition.
[f] Dorman *et al.* (2013). Measurements acquired at R_h = 1.4 AU during the 2003 apparition.

A'Hearn *et al.* (1985) report mixing ratios over a range of R_h, comparisons are made to their measurements taken at R_h most similar to RD13 ($\sim$ 1.2 AU) or to those reported in Roth *et al.* (2018) ($\sim$ 0.4 AU), respectively.

For the pre-perihelion data, the primary volatile mixing ratios HCN/H_2O and C_2H_2/H_2O reported in RD13 cannot account for the mixing ratios CN/OH or C_2/OH in A'Hearn *et al.* (1985) or any other study, suggesting that HCN and C_2H_2 are not the sole parents of CN and C_2, respectively, during the pre-perihelion portion of an apparition. The mixing ratios HCN/H_2O and C_2H_2/H_2O reported in Roth *et al.* (2018) cannot account for the post-perihelion mixing ratios CN/OH and C_2/OH, and also suggest that HCN and C_2H_2 are not their sole parents.

Similar trends have been observed for other short-period comets. Measured HCN/H_2O and C_2H_2/H_2O for comets 103P/Hartley 2, 6P/d'Arrest, and 45P/Honda-Mrkos-Pajdušáková (hereafter 45P/HMP) cannot account for their CN/OH and C_2/OH, respectively (A'Hearn *et al.* (1995); Dello Russo *et al.* (2016a) and refs. therein; DiSanti *et al.* (2017)). However, the mixing ratio NH_3/H_2O reported in Roth *et al.* (2018) is large enough to account for both the reported NH_2/H_2O mixing ratio, as well as the NH/OH mixing ratio in pre-perihelion observations, suggesting that no additional parents may be needed to explain these fragment species abundances. Additionally, the mixing ratio NH_3/H_2O is also consistent with that predicted by Dorman *et al.* (2013) based on their measured NH/OH.

3.3.3. Comparison to Comets as Measured at Near-Infrared Wavelengths. Combined with previous work, the results of the 2017 perihelion passage of Encke can be placed into the context of the comet population observed at near-infrared wavelengths to date, including the hypervolatile content of comets and measurements of comets at small R_h. Aspects of Encke's place within this diverse population are discussed in turn below.

3.3.3.1. Comparison to measurements of other comets at small R_h. The measurements of Encke at $R_h \sim 0.4$ AU are among only a handful of IR studies of comets at $R_h < 0.8$ AU. Of particular interest are OCC D/2012 S1 (ISON) and JFC 45P/HMP, both of which were measured at similarly small R_h. ISON, a dynamically new, sun-grazing OCC that was the subject of a worldwide observing campaign, showed mixing ratios of HCN, NH_3, C_2H_2, and H_2CO that increased as its heliocentric distance decreased from 0.83 AU to inside 0.6 AU (Dello Russo *et al.*, 2016b; DiSanti *et al.*, 2016). 45P/HMP, the first JFC to have its primary volatile composition sampled within $R_h < 0.8$ AU, was enriched in CH_3OH, strongly depleted in CO and HCN, and consistent with respect to median values for CH_4, H_2CO, NH_3, C_2H_2, and C_2H_6 (DiSanti *et al.*, 2017). In these respects, Encke is perhaps most similar to ISON, in that H_2CO and HCN were enriched at $R_h \sim 0.4$ AU

in 2017 compared to $R_h \sim 1.2$ AU in 2003., however as mentioned more observations are needed to test whether this owes more to heliocentric distance rather than seasonal (pre-/post-perihelion) or other effects.

3.3.3.2. Comparison to comet 21P/Giacobini-Zinner. JFC 21P/Giacobini-Zinner is the only other comet to have high-resolution near-infrared spectroscopic measurements spanning more than one apparition. Weaver *et al.* (1999) detected H_2O and CH_3OH (with mixing ratio 0.9%–1.4%), and Mumma *et al.* (2000) reported CO (10 ± 6%) and C_2H_6 (0.22 ± 0.13%) during the 1998 apparition. DiSanti *et al.* (2013) reported H_2O, CH_3OH (1.22 ± 0.11%), and C_2H_6 (0.14 ± 0.02%) from spectra obtained during its 2005 apparition. Mixing ratios of the two species measured both in 1998 and 2005 (CH_3OH and C_2H_6) were consistent in 21P/G-Z. Although these results are suggestive, the uncertainties in the 1998 measurements are relatively large, and without a more comprehensive study of its volatile inventory, it is difficult to say whether the bulk primary volatile composition of 21P/G-Z showed secular changes across apparitions. In contrast to 21P/G-Z, multiple species were compared across apparitions and with small uncertainties in Encke. Fortunately, the 2018 apparition of 21P/G-Z provided an excellent opportunity to more completely and systematically characterize its volatile composition (see Sections 3.4 and 4.1).

3.3.3.3. Hypervolatiles in Encke: CO, CH_4, and C_2H_6. CO, CH_4, and C_2H_6 (respectively) are the three most volatile molecules systematically observed in comets (Dello Russo *et al.*, 2016a). All three hypervolatiles are depleted in Encke compared with their respective mean abundances among comets (Figure 3.11). Figure 3.12 compares these measurements ($CO/CH_4 = 3.90 \pm 0.51$ and $C_2H_6/CH_4 = 0.34 \pm 0.05$) to 18 OCCs and JFCs 67P/Churyumov-Gerasimenko (Le Roy *et al.*, 2015) and 45P/HMP (DiSanti *et al.*, 2017). For Encke the ratio CO/CH_4 falls near the median, whereas C_2H_6/CH_4 is near the low end; however, $C_2H_6/CH_4 = 0.94 \pm 0.29$ for Encke in 2003, near the median. On the other hand, 67P/C-G has the highest CO/CH_4 and C_2H_6/CH_4 measured in any comet, although direct comparisons between the in situ measurements of Le Roy *et al.* (2015) and the ground-

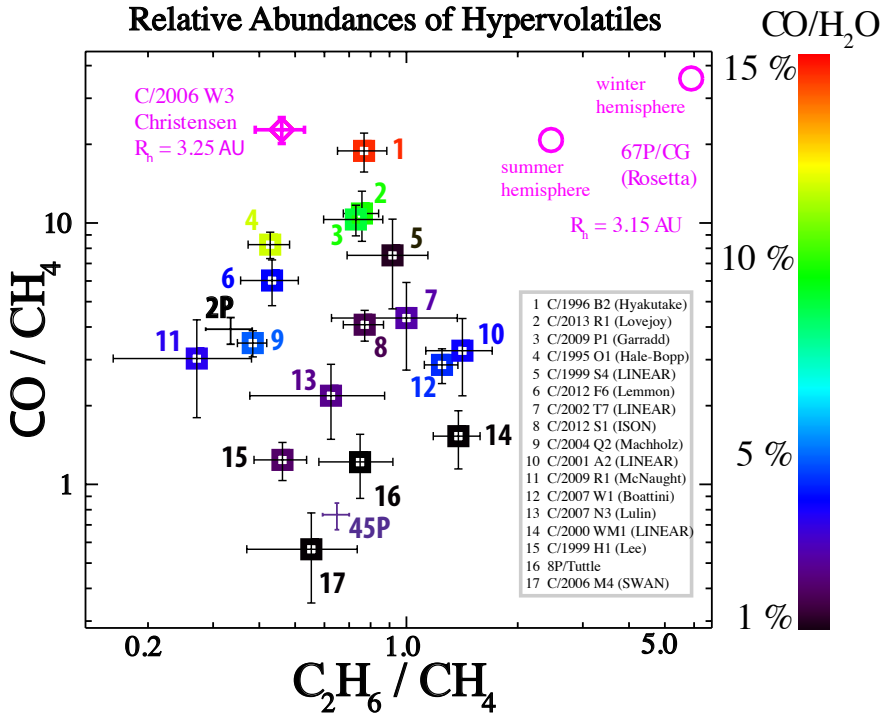

Figure 3.12. Ratios of hyperovlailes in comets characterized to date in the near-infrared, adapted from Bonev *et al.* (2017), and modified to include 2P/Encke (Roth *et al.*, 2018) and 45P/HMP (DiSanti *et al.*, 2017). Encke is highlighted as "2P".

based line of sight (bulk coma) measurements in this work are not straightforward. Thus, it is possible that the hypervolatile content of JFCs may span the entire range of CO/CH_4 and C_2H_6/CH_4 measured among OCCs. However, with relative hypervolatile abundances characterized to date for only three ecliptic comets (compared to 18 OCCs), it is worth noting that these statistics are still being *established* for ecliptic comets, and further observations are critically needed.

3.3.3.4. Hydrocarbon species, oxygen-bearing species, and nitrogen-bearing species in Encke. Similarly, Encke can be compared to other comets observed at near-infrared wavelengths by examining the ratios of chemically related hydrocarbon species (CH_4, C_2H_2, C_2H_6), oxygen-bearing species (CO, H_2CO, CH_3OH), and nitrogen-bearing species (NH_3, HCN). For Encke in 2017, Roth *et al.* (2018) reported CH_4/C_2H_6 = 2.97

± 0.48 and C_2H_2/C_2H_6 < 0.19, CO/CH_3OH = 0.49 ± 0.06 and H_2CO/CH_3OH = 0.31 ± 0.05, and NH_3/HCN = 5.08 ± 0.72. Figures 3.13-3.15 show these values in Encke along with corresponding measurements in comets sampled to date in the near-infrared. All values are taken from Dello Russo *et al.* (2016a) with the exception of 45P/HMP (DiSanti *et al.*, 2017). Figure 3.13 shows that whereas Encke was closer to the median during 2003, in 2017 it was distinctly on the low end of hydrocarbon abundances among comets. Its exceptionally low mixing ratios C_2H_6/H_2O and (upper limit for) C_2H_2/H_2O are reflected in its high CH_4/C_2H_6 and low C_2H_2/C_2H_6. Figure 3.14 shows that in 2017 Encke was near the median in its oxygen-bearing species content (relative to CH_3OH), yet in 2003 it was among the lowest values in measured comets, owing largely to its enriched CH_3OH. This change in oxygen-bearing species abundances can be attributed to the significant differences in H_2CO/H_2O and CH_3OH/H_2O between 2003 and 2017 measurements. Figure 3.15 shows that Encke is among depleted comets in nitrogen-bearing species.

3.3.3.5. Encke in the context of the comet population. As in RD13, the 2017 apparition of Encke showed a comet that does not easily fit into a taxonomic classification. Although no species were found to be enriched in 2017 compared to mean values among comets, two species (H_2CO and NH_3) were similar to the mean, and all other species were depleted to varying degrees. Dello Russo *et al.* (2016a) proposed a classification system based on primary volatile abundances using cluster analysis. Based on its composition as measured in 2003, Encke falls within Group B (hydrocarbon, HCN, H_2CO, and CO poor-to-typical), and is most similar to Subgroup 4 (hydrocarbon, HCN, and H_2CO poor, CH_3OH typical). However, Encke does not fall into the same Group (or Subgroup) based on the 2017 study reported in Roth *et al.* (2018). Rather, Encke belongs within Group A (hydrocarbon, CH_3OH, and CO poor) and is most similar to Subgroup 2 (hydrocarbon, CH_3OH, and CO poor, H_2CO and HCN typical).

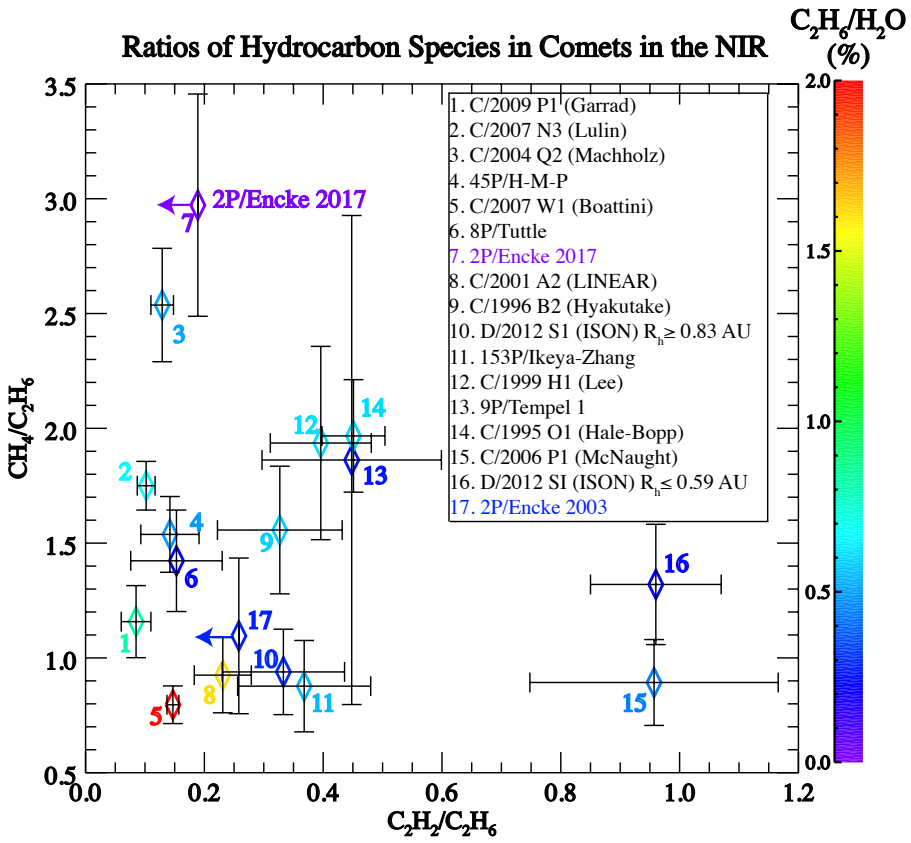

Figure 3.13. Ratios of hydrocarbon species in comets as measured in the near-infrared (Dello Russo *et al.*, 2016a; DiSanti *et al.*, 2017). Each comet is color-coded by its ratio C_2H_6/H_2O. Encke is highlighted with a text box, and the left-facing arrow represents the 3σ upper limit C_2H_2/C_2H_6.

Encke's place within these groupings during each apparition is not surprising. Ecliptic comets (JFCs and Encke-type) are most likely to be found in Groups A and B, reflecting the generally depleted nature of their volatile content. However, one could reasonably expect to have found Encke in Group C based on its composition as measured in 2017. This group is mostly populared by comets that were observed at small R_h such as Encke (0.45–0.53 AU) or after a perihelion passage well within 1 AU. This is perhaps reflective of the nature of volatile release at small R_h, which can originate from native ices and/or from thermal degradation of grains (Dello Russo *et al.*, 2016a). Perhaps Encke is an exception

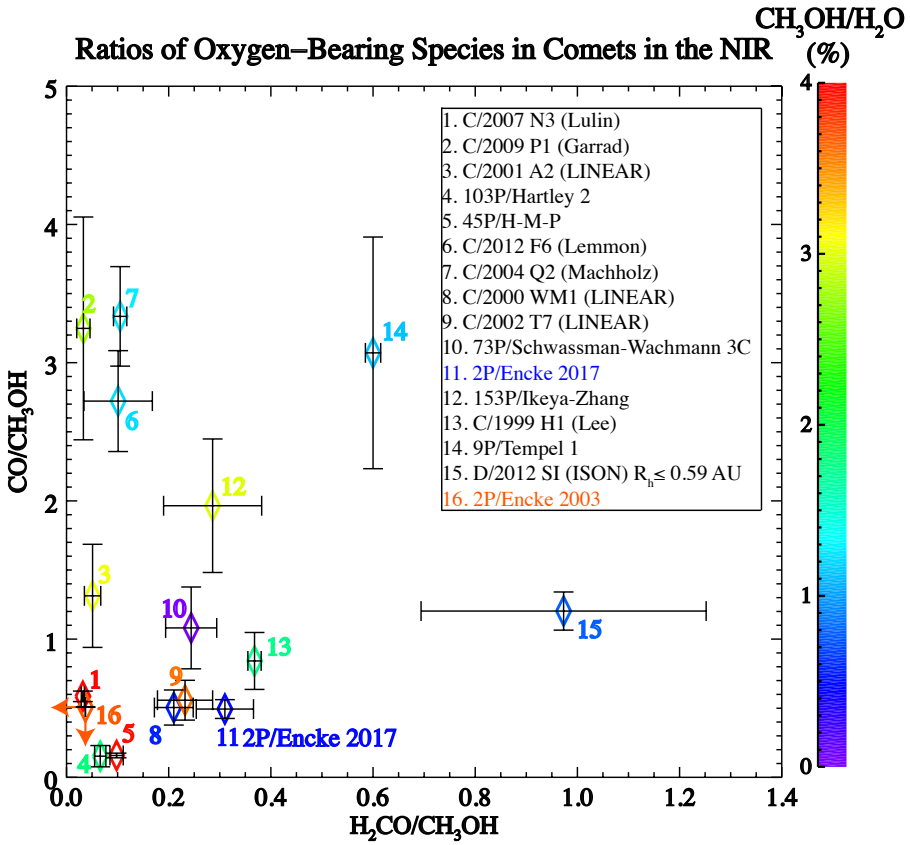

Figure 3.14. Ratios of oxygen-bearing species in comets as measured in the near-infrared. Each comet is color-coded by its ratio CH_3OH/H_2O. Encke is highlighted with a text box.

to this trend due to its status as the most thermally evolved comet known, as evidenced by its strongly depleted volatile content. Clearly, more work is needed to further improve the evolving taxonomy based on primary volatile composition.

3.4. SUMMARY OF RESULTS FOR 2P/ENCKE AND UPCOMING OPPORTUNITIES

Fluorescence emission was detected from a suite of primary volatiles (H_2O, CO, C_2H_6, CH_3OH, CH_4, H_2CO, NH_3, OCS, and HCN) and fragment species (OH*, NH_2, and CN) in ecliptic comet 2P/Encke, and C_2H_2 was stringently constrained, using the recently commissioned iSHELL spectrograph at the NASA IRTF. The highly favorable 2017

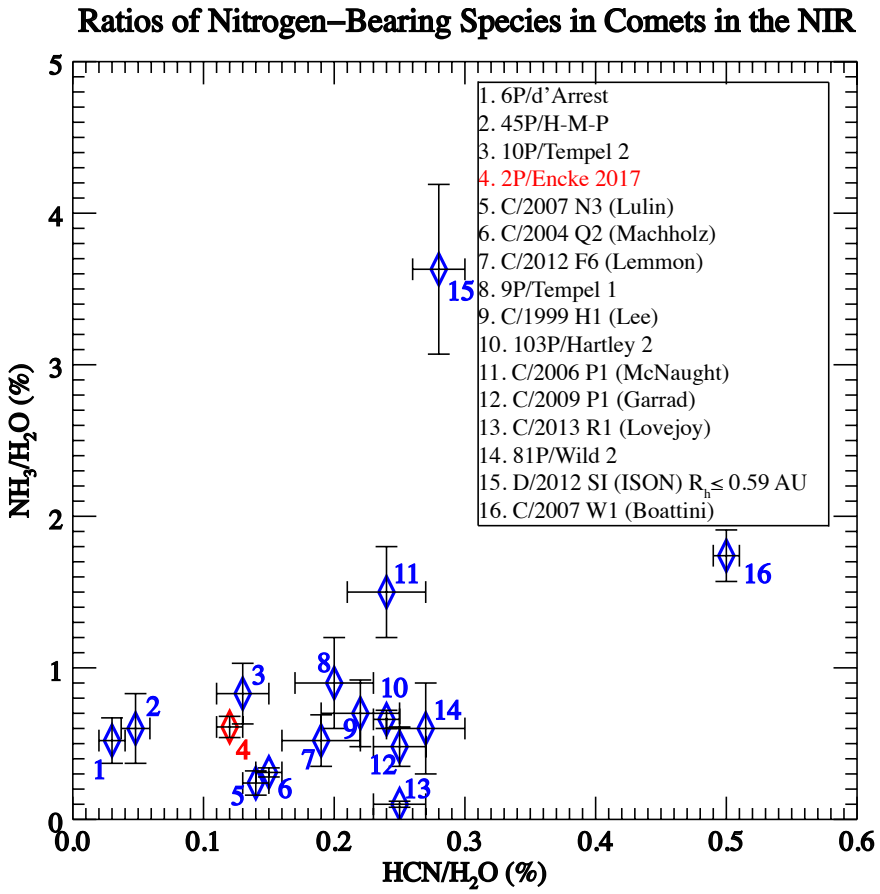

Figure 3.15. Ratios of nitrogen-bearing species in comets as measured in the near-infrared. Encke is highlighted in red.

apparition of Encke featured sufficient geocentric velocity to permit secure detections of the hypervolatiles CO and CH_4, further laying the groundwork for establishing robust statistics for these species in ecliptic comets. The excellent sensitivity, large spectral grasp, and unique daytime guiding capabilities of iSHELL allowed for the first comprehensive comparison of primary volatile composition in a comet across multiple apparitions. Dramatic differences were observed in the mixing ratios of several primary volatiles in 2017 compared to those reported from 2003. Possible mechanisms for these effects were discussed, including the

possibility of distinct, chemically heterogeneous sources in the nucleus, additional sources (e.g., dust) at small heliocentric distances, and pre-/ post-perihelion asymmetries in volatile release.

Ground-based studies of primary volatile composition of comets are critical to interpreting the (continually evolving) taxonomy of comets and relating measured mixing ratios to conditions in the proto-solar nebula where and when a given comet formed. It is yet another reminder of the extensive compositional diversity among comets in that one short-period ecliptic comet (Encke) showed clear differences in coma composition across apparitions, whereas another (21P/Giacobini-Zinner) may not. This reinforces the difficulty of drawing conclusions from a single body based on limited observations during a given apparition. Fortunately, the 2018 apparition of 21P/G-Z was favorable, and an extensive campaign (including both pre- and post-perihelion observations) was carried out. Additionally, the bright comet 46P/Wirtanen made a historic apparition in 2018 December, passing within 30 lunar distances of Earth near perihelion. A global, multi-wavelength observation campaign was carried out, which will reveal the composition and spatial distributions of volatiles in the coma of 46P/Wirtanen at more nearly mission-scale sensitivities. These observations may shed further light on potential differences in composition, both about perihelion and across apparitions, for ecliptic comets.

Further studies that address each of these pressing areas in cometary science (i.e., observations at small R_h, pre-/ post-perihelion, and comparisons across multiple apparitions) are needed to answer questions stimulated by the 2017 study of the peculiar comet 2P/Encke.

4. PROBING THE EVOLUTIONARY HISTORY OF COMETS: AN INVESTIGATION OF THE HYPERVOLATILES CO, CH_4, AND C_2H_6 IN THE JUPITER-FAMILY COMET 21P/GIACOBINI-ZINNER

4.1. COMET 21P/GIACOBINI-ZINNER

Understanding the cosmogonic record encoded in the parent volatiles stored in cometary nuclei requires investigating whether evolution (thermal or otherwise) has modified the composition of short-period comets during successive perihelion passages. As the most volatile molecules in comets, the abundances of CO, CH_4, and C_2H_6 in short-period comets may serve to elucidate the interplay between natal conditions and post-formative evolution in setting present-day composition, yet secure measurements of CO and CH_4 in Jupiter-family comets (JFCs) are especially sparse. The highly favorable 2018 perihelion passage of JFC 21P/Giacobini-Zinner (hereafter G-Z) featured sufficiently high geocentric velocity simultaneously with small geocentric distance, and afforded the opportunity to characterize its hypervolatile content. The increased sensitivity and long on-source integration times afforded by the high-resolution iSHELL spectrograph, which became available for use at the NASA Infrared Telescope Facility in late 2016, together with unusually favorable apparitions for several short-period comets have to date enabled sensitive searches for these molecules in short-period comets similar to G-Z, such as 2P/Encke (Roth *et al.*, 2018) and JFC 45P/Honda-Mrkos-Pajdušáková (DiSanti *et al.*, 2017). G-Z is the prototype for the eponymous "GZ-type" of carbon-chain depleted comets, depleted in both C_2 and NH_2 with respect to H_2O and accounting for ~6% of comets measured (A'Hearn *et al.*, 1995; Fink, 2009). Coupled with published near-infrared observations of G-Z during the 1998 and 2005 apparitions (DiSanti *et al.*, 2013; Mumma *et al.*, 2000; Weaver *et al.*, 1999),

the measurements reported here also enabled searches for coma compositional variability of hypervolatiles on timescales of days, both pre- vs. post-perihelion, and across multiple perihelion passages.

During its 2018 apparition, G-Z both reached perihelion (1.01 AU) and was closest to Earth (0.39 AU) on September 10. On UT 2018 July 25, 28, 29, and 31, September 7 and 11, and October 10, G-Z was observed with the high-resolution ($\lambda/\Delta\lambda \sim 40{,}000$), near-infrared, immersion-grating echelle spectrograph iSHELL (Rayner *et al.*, 2012, 2016) at the 3 m NASA IRTF to characterize its hypervolatile composition. Three iSHELL settings (Lcustom, Lp1, and M2) were utilized so as to fully sample a suite of molecular abundances. The slit was oriented along the projected Sun-comet line on all dates (see Table 4.1).

On July and October dates, observations were performed with a 6-pixel (0.75″) wide slit, using a standard ABBA nod pattern, with A and B beams symmetrically placed about the midpoint of the 15″ long slit and separated by half its length. A malfunction of the iSHELL dekker precluded the use of the 15″ long slit in September and necessitated off-chip nodding using the 0.75″ wide by 5″ long slit. G-Z was placed in the center of the slit for A frames and nodded 20″ perpendicular to the slit for B (sky) frames. In both cases, combining spectra of the nodded frames as A-B-B+A cancelled emissions from thermal background, instrumental biases, and "sky" emission (lines and continuum) to second order in air mass. Flux calibration was performed using appropriately placed bright IR flux standard stars on each date using a wide (4.0″) slit. On October 10, a telescope pointing error precluded the acquisition of flux calibration sets; therefore, a flux calibration factor (Γ, W/m^2/cm^{-1}/ADU/s) was adopted based on that measured on other dates. Although this could affect absolute production rates, derived mixing ratios should be unaffected, as the targeted molecules were observed simultaneously or contemporaneously with water or OH prompt emission (OH*, a proxy for water production, see Bonev *et al.* (2006)) within each setting. The observing log is shown in Table 4.1.

Table 4.1. Observing Log for 21P/Giacobini-Zinner.

Date (2018)	iSHELL Setting	UT	R_h (AU)	Δ (AU)	Δ_{dot} (km s^{-1})	T_{int} (minutes)	Slit PA
7/25	M2	12:02 – 13:58	1.20	0.64	-13.67	85	220°
7/28	Lp1	10:58 – 12:41	1.18	0.61	-13.53	92	222°
	M2	13:32 – 15:44	1.18	0.61	-13.39	96	
7/29	LCS	11:17 – 13:08	1.17	0.61	-13.43	100	223°
	M2	13:25 – 15:23	1.17	0.61	-13.32	86	
7/31	Lp1	10:42 – 12:56	1.16	0.59	-13.30	120	225°
	M2	13:50 – 15:24	1.16	0.59	-13.16	74	
9/7	Lp1	14:01 – 16:14	1.01	0.39	-1.89	54	270°
	LCS	16:56 – 18:16	1.01	0.39	-1.61	34	
9/11	Lp1	13:37 – 15:53	1.01	0.39	0.36.	66	271°
10/10	M2	13:21 – 14:23	1.10	0.51	11.16	50	276°
	Lp1	14:35 – 16:58	1.10	0.51	11.32	108	

R_h, Δ, and Δ_{dot} are heliocentric distance, geocentric distance, and geocentric velocity, respectively, of 21P/Giacobini-Zinner, and T_{int} is total integration time on source. The slit position angle (PA) was oriented along the projected Sun-comet line on all dates.

For the September observations (using the shorter 5″ slit), examination of the frames revealed that the iSHELL flat lamp provided illumination of the chip that was not consistent with that of the sky. This introduced a curvature effect into the spectra, which was corrected by fitting and then subtracting a polynomial baseline (Figure 4.1). This may have affected flux calibration and therefore the calculated absolute molecular production rates (Q's) reported for the September dates. However, emissions from all molecules within each individual iSHELL setting are sampled simultaneously, and therefore the derived mixing ratios should be unaffected. The general consistency of production rates and derived mixing ratios on both September dates suggests that any uncertainties introduced by this illumination offset were likely minimal.

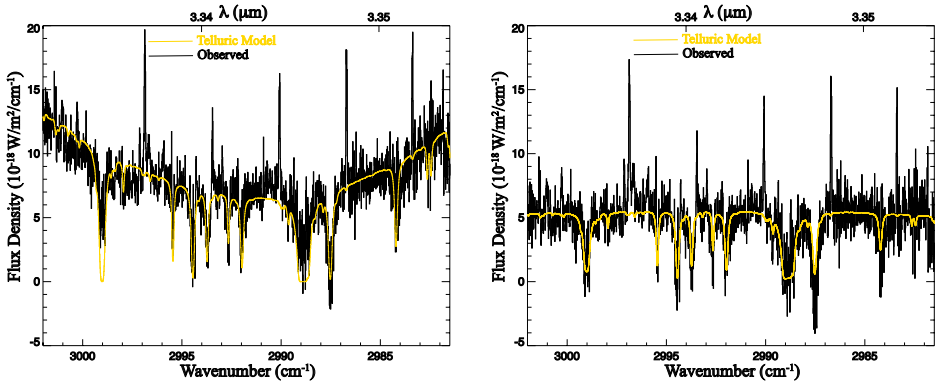

Figure 4.1. Extracted spectra of comet G-Z showing order 155 of the iSHELL Lp filter taken with the 5″ long slit on UT 2018 September 11 before (left panel) and after (right panel) baseline subtraction. The gold trace is the telluric absorption model (convolved to the instrumental resolution).

4.2. RESULTS

Data for G-Z were analyzed using the procedures described in Section 1.6.1. Results specific to G-Z are discussed in turn below.

4.2.1. Growth Factors. Growth factors (GF) were determined for both the gas and the dust when signal-to-noise ratio (S/N) was sufficiently high (i.e., only for H_2O, CO, and C_2H_6). For September dates, the narrow 5″ slit precluded the use of Q-curves to calculate GFs. Therefore, a GF of 1.8 was assumed, a value consistent with that obtained from other dates (see Tables 4.2, 4.3, 4.4).

4.2.2. Spatial Profiles. For July dates, emission spatial profiles were extracted for H_2O, CO, and C_2H_6 in G-Z (Figure 4.2). Figure 4.2 shows that (within uncertainty) the spatial profiles for each molecule and dust are very similar. This suggests that emission for all three species closely tracked that of co-measured dust; therefore, on dates for which molecular GFs could not be well-constrained, that of co-measured dust within each setting was adopted when calculating production rates (Tables 4.2, 4.3, 4.4).

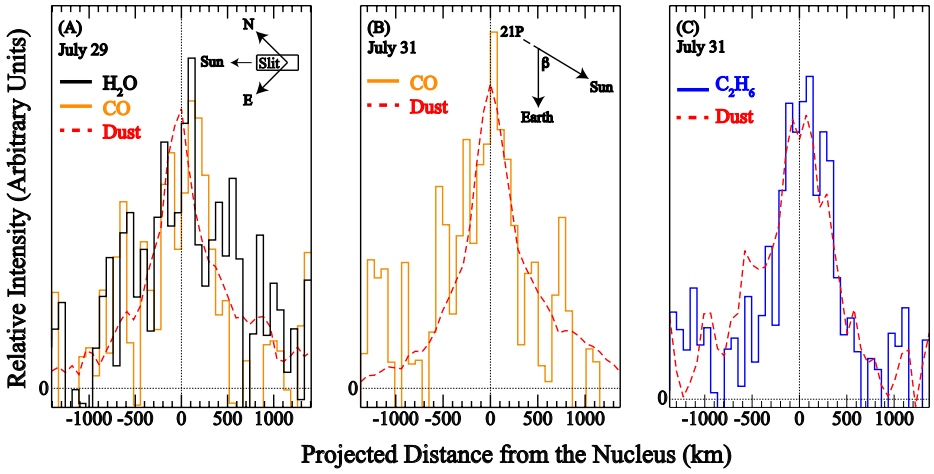

Figure 4.2. Coma spatial distributions of volatiles in G-Z. A. Spatial profiles of co-measured emissions in G-Z for H_2O (black), CO (orange), and dust (red) on UT 2018 July 29. The slit was oriented along the projected Sun-comet line (position angle 223°), with the Sun-facing direction to the left as indicated. Also shown is the Sun-comet-Earth angle (phase angle, β) of 59°. The horizontal bar indicating 1″ corresponds to a projected distance of approximately 449 km at the geocentric distance of G-Z. B. Spatial profiles of co-measured emissions for CO (orange) and dust (red) on UT 2018 July 31. C. Spatial profiles of co-measured emissions for C_2H_6 (blue) and dust (red) on UT 2018 July 31. The observing geometry on July 31 was similar to that of July 29, with a position angle of 225°and a phase angle of 60°

4.2.3. Rotational Temperature. Consistent rotational temperatures for multiple molecules were found on all dates (including H_2O). The rotational temperature ($T_{\rm rot}$) for H_2O was well-constrained on September 7 (being 75 ± 3 K) and was consistent (within 1σ uncertainty) with that for C_2H_6 on September 11 (66^{+12}_{-9} K). Rotational temperatures for the July dates were also in formal agreement, being 64^{+15}_{-11} K for CO on July 28 and 48^{+19}_{-13} K for H_2O on July 29. Well-constrained rotational temperatures could not be derived for any molecules on October 10. Production rates and mixing ratios were calculated at $T_{\rm rot}$ = 48 K and 64 K for July dates. $T_{\rm rot}$ was varied as a parameter for the October date, with

production rates and mixing ratios calculated for each molecule at representative T_{rot} = 50 K, 60 K, and 70 K. In general, mixing ratios for a given species derived at each temperature are consistent with one another within 1σ uncertainty (Tables 4.2, 4.3, 4.4).

4.2.4. Secure Detections of Hypervolatiles. The detections of CO, CH_4, and C_2H_6 in G-Z are particularly notable for two reasons: (1) They address the paucity of measurements of CO and CH_4 in ecliptic comets in general, and (2) The measurement of these hypervolatiles in an individual ecliptic comet across multiple perihelion passages, and on multiple dates during its 2018 apparition. Of all primary volatiles systematically measured in comets, these three molecules are most sensitive to thermal processing, but as noted earlier, CO and CH_4 are also among the most difficult to sample from the ground due to a lack of sensitivity and/or adequate geocentric velocity. G-Z's excellent geocentric velocity ($|\Delta_{dot}| > 13$ km s^{-1} pre-perihelion, $|\Delta_{dot}| > 11$ km s^{-1} post-perihelion) allowed firm detections of all three species. CO and CH_4 have been measured in fewer than ten ecliptic comets (with most detections being below the 5σ level), making these measurements in G-Z a critical component in establishing statistics for these species in ecliptic comets, and determining the importance of natal versus evolutionary effects on present cometary volatile composition. Figures 4.3 – 4.8 show clear CO, H_2O, CH_4, C_2H_6, and OH* emissions in G-Z superimposed on the cometary continuum during various portions of its 2018 perihelion passage.

4.3. COMA HYPERVOLATILE COMPOSITION THROUGHOUT THE 2018 PERIHELION PASSAGE

The 2018 apparition of G-Z provided an opportunity to conduct the first comprehensive comparison of hypervolatile abundances through three perihelion passages and on multiple dates within a given perihelion passage, thereby allowing pressing questions in cometary science to be addressed. These include testing possible evolutionary effects on coma volatile composition, as well as searching for coma compositional variability on

Table 4.2. Pre-perihelion Hypervolatile Composition of Comet 21P/Giacobini-Zinner.

Setting	Molecule	T_{rot}[1] (K)	GF[2]	Q[3] (10^{25} mol s^{-1})	Q_x/Q_{H2O} (%)
2018 July 25, R_h = 1.20 AU, Δ = 0.64 AU, Δ_{dot} = -13.67 km s^{-1}					
M2	H_2O	(48)	1.82 ± 0.17[4]	2692 ± 292	100
	CO	(48)	(1.82)	40.5 ± 5.1	1.51 ± 0.25
	H_2O	(64)	(1.82)	3028 ± 306	100
	CO	(64)	(1.82)	47.4 ± 5.9	1.56 ± 0.25
2018 July 28, R_h = 1.18 AU, Δ = 0.61 AU, Δ_{dot} = -13.5 km s^{-1}					
LP1	C_2H_6	(48)	(1.91)	6.26 ± 1.28	0.23 ± 0.05
	CH_4	(48)	(1.91)	17.5 ± 4.2	0.63 ± 0.17
	C_2H_6	(64)	(1.91)	7.02 ± 1.33	0.24 ± 0.05
	CH_4	(64)	(1.91)	26.1 ± 6.2	0.88 ± 0.24
M2	H_2O	(48)	1.91 ± 0.14[4]	2771 ± 251	100
	CO	(48)	(1.91)	45.1 ± 3.6	1.63 ± 0.20
	H_2O	(64)	(1.91)	2961 ± 297	100
	CO	64^{+15}_{-11}	(1.91)	50.4 ± 4.0	1.70 ± 0.22
2018 July 29, R_h = 1.17 AU, Δ = 0.61 AU, Δ_{dot} = -13.3 km s^{-1}					
LCS	H_2O	48^{+19}_{-13}	(1.97)	2643 ± 229	100
M2	H_2O	(48)	(1.97)	2527 ± 345	100
	CO	(48)	1.97 ± 0.21[4]	34.8 ± 4.7	1.38 ± 0.26
	H_2O	(64)	(1.97)	2726 ± 369	100
	CO	(64)	(1.97)	41.2 ± 4.4	1.51 ± 0.26
2018 July 31, R_h = 1.16 AU, Δ = 0.59 AU, Δ_{dot} = -13.2 km s^{-1}					
LP1	C_2H_6	(48)	(1.66)	6.05 ± 0.77	0.24 ± 0.05
	CH_4	(48)	(1.66)	28.1 ± 4.1	1.12 ± 0.26
	C_2H_6	(64)	(1.66)	6.64 ± 0.92	0.24 ± 0.05
	CH_4	(64)	(1.66)	41.4 ± 6.0	1.52 ± 0.31
M2	H_2O	(48)	(1.66)	2503 ± 365	100
	CO	(48)	1.66 ± 0.22	50.1 ± 4.9	2.00 ± 0.36
	H_2O	(64)	(1.66)	2716 ± 262	100
	CO	(64)	(1.66)	58.6 ± 4.8	2.15 ± 0.27

[1] Rotational temperature. Values in parentheses are assumed.
[2] Continuum growth factor. Values in parentheses are assumed.
[3] Global production rate. Errors in production rate include line-by-line deviation between modeled and observed intensities and photon noise (see Bonev (2005); Bonev *et al.* (2007); Dello Russo *et al.* (2004)).

multiple timescales, including day-to-day, pre- vs. post-perihelion, and across perihelion passages. Each of these topics is discussed below in turn. Unless otherwise noted, all dates refer to the 2018 apparition.

Table 4.3. Perihelion Hypervolatile Composition of Comet 21P/Giacobini-Zinner.

Setting	Molecule	T_{rot}[1] (K)	GF[2]	Q[3] (10^{25} mol s^{-1})	Q_x/Q_{H2O} (%)
2018 September 7, R_h = 1.01 AU, Δ = 0.39 AU, Δ_{dot} = -1.7 km s^{-1}					
LP1	C_2H_6	(75)	(1.8)[4]	10.6 ± 1.1	0.35 ± 0.06
	OH*	(75)	(1.8)[4]	3036 ± 357	100
LCS	H_2O	75 ± 3	(1.8)[4]	3206 ± 112	100
2018 September 11, R_h = 1.01 AU, Δ = 0.47 AU, Δ_{dot} = 0.3 km s^{-1}					
LP1	C_2H_6	64^{+12}_{-9}	(1.8)[4]	7.15 ± 0.39	0.26 ± 0.02
	C_2H_6	(75)	(1.8)[4]	7.49 ± 0.43	0.28 ± 0.02
	OH*	(75)	(1.8)[4]	2713 ± 168	100

[1] Rotational temperature. Values in parentheses are assumed.
[2] Growth factor. Values in parentheses are assumed.
[3] Global production rate. Errors in production rate include line-by-line deviation between modeled and observed intensities and photon noise (see Bonev (2005); Bonev *et al.* (2007); Dello Russo *et al.* (2004)).
[4] A growth factor for September dates could not be derived owing to use of the 5″ wide slit; therefore, a GF of 1.8, consistent with growth factors derived for major species pre- and post-perihelion, was assumed.

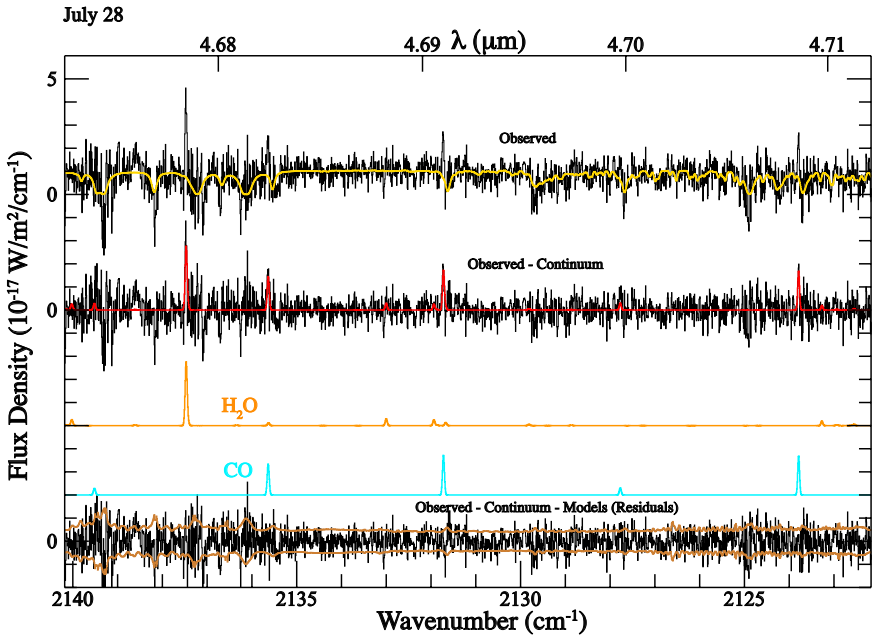

Figure 4.3. Extracted spectra showing clear detections of CO and H_2O in comet G-Z on UT 2018 July 28.

Table 4.4. Post-perihelion Hypervolatile Composition of Comet 21P/Giacobini-Zinner.

Setting	Molecule	T_{rot}[1] (K)	GF[2]	Q[3] (10^{25} mol s^{-1})	Q_x/Q_{H2O} (%)
2018 October 11, R_h = 1.10 AU, Δ = 0.51 AU, Δ_{dot} = 11.1 km s^{-1}					
M2	H_2O	(50)	1.93 ± 0.28[4]	2054 ± 257	100
	CO	(50)	(1.93)	22.9 ± 2.9	1.11 ± 0.20
	H_2O	(60)	(1.93)	2029 ± 253	100
	CO	(60)	(1.93)	25.5 ± 3.3	1.26 ± 0.23
	H_2O	(70)	(1.93)	2028 ± 252	100
	CO	(70)	(1.93)	28.1 ± 3.2	1.39 ± 0.25
LP1	C_2H_6	(50)	(1.93)	2.65 ± 0.42	0.13 ± 0.03
	CH_4	(50)	(1.93)	< 10 (3σ)	< 0.55 (3σ)
	C_2H_6	(60)	(1.93)	2.92 ± 0.39	0.14 ± 0.03
	CH_4	(60)	(1.93)	< 13 (3σ)	< 0.72 (3σ)
	C_2H_6	(70)	(1.93)	3.20 ± 0.41	0.16 ± 0.03
	CH_4	(70)	(1.93)	< 16 (3σ)	< 0.89 (3σ)

[1] Rotational temperature. Values in parentheses are assumed.
[2] Growth factor. Values in parentheses are assumed.
[3] Global production rate. Errors in production rate include line-by-line deviation between modeled and observed intensities and photon noise (see Bonev (2005); Bonev *et al.* (2007); Dello Russo *et al.* (2004)).
[4] Continuum (dust) growth factor.

4.3.1. CO. Clear, simultaneously measured detections of CO and H_2O were found on multiple dates in G-Z (Figures 4.3, 4.7) pre- as well as post-perihelion. The mixing ratio CO/H_2O was consistent on all pre-perihelion July dates within 1σ uncertainty (Table 4.2; see also Figure 4.9) with a weighted average abundance of 1.72 ± 0.12% for T_{rot} = 64 K. This was somewhat lower post-perihelion in October, 1.26 ± 0.23% for T_{rot} = 60 K, suggesting that CO/H_2O in G-Z may display pre- vs. post-perihelion asymmetry. However, given the uncertainty in T_{rot} in October, it is important to note that the range of possible October CO mixing ratios is in formal agreement with those from July (Tables 4.2, 4.4). These mixing ratios are depleted with respect to the mean for all comets measured to date at near-infrared wavelengths (5.1 ± 1.3%), but are consistent with the few measurements in ecliptic comets (Dello Russo *et al.*, 2019, 2016a; DiSanti *et al.*, 2017; Roth *et al.*, 2018).

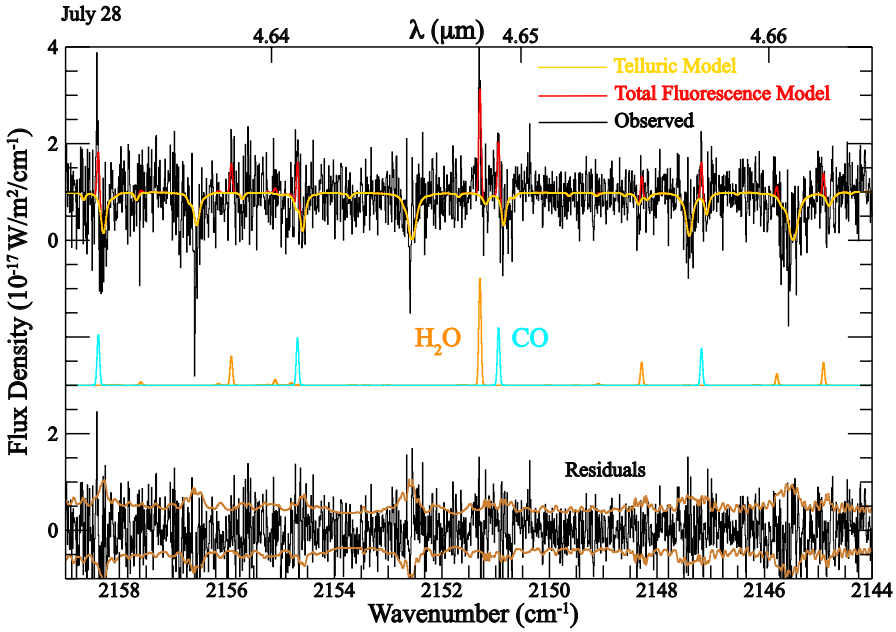

Figure 4.4. Extracted spectra showing detections of CO and H_2O on UT 2018 July 28.

4.3.2. CH_4. CH_4 bears the distinction of being the most severely undersampled hypervolatile in ecliptic comets, having been firmly measured in only six to date (Dello Russo *et al.* (2016a) and refs. therein, Dello Russo *et al.* (2019); DiSanti *et al.* (2017); Roth *et al.* (2018)). Utilizing the large spectral grasp of iSHELL, CH_4 was measured in G-Z at the 4σ level on July 28 (0.88 ± 0.24% for T_{rot} = 64 K; see Figure 4.5 and Table 4.2) and at >6σ on July 31 (1.52 ± 0.31% for T_{rot} = 64 K). A sensitive (3σ) upper limit was derived for October 10 (< 0.72% for T_{rot} = 60 K). This suggests that CH_4 may have been variable from day-to-day in G-Z. However, there are important caveats for this CH_4 study.

A well-constrained rotational temperature for CH_4 could not be derived, and calculated CH_4 production rates and mixing ratios show a sensitive dependence on assumed T_{rot} (Tables 4.2, 4.4). Assuming T_{rot} = 48 K, pre-perihelion CH_4 mixing ratios in G-Z (0.63 ± 0.17% for July 28, 1.12 ± 0.26% for July 31; Table 4.2) are consistent with mean values in measured OCCs (0.88 ± 0.10%), and are enriched compared to the few measurements

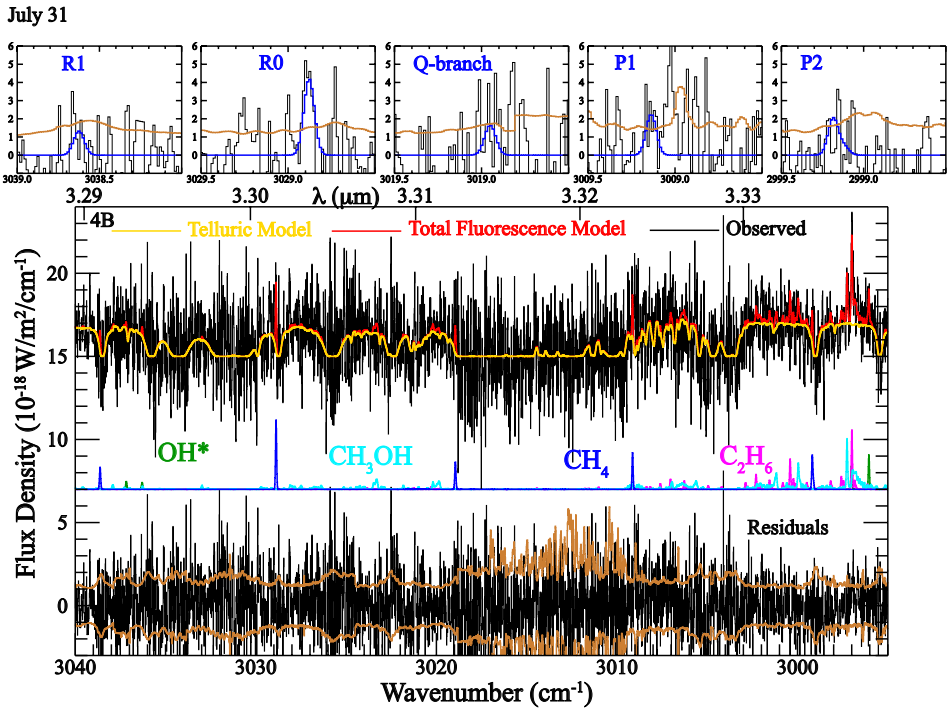

Figure 4.5. Extracted spectra showing detections of CH_4, C_2H_6, CH_3OH, and OH* on UT 2018 July 31. The zoomed subplots highlight the locations of individual CH_4 emissions. Each subplot has the same units as the larger plot.

in JFCs. For T_{rot} = 64 K, the degree of CH_4-enrichment increases. However, G-Z is not the first instance of a CH_4-enriched JFC, with similar mixing ratios reported in 45P/Honda-Mrkos-Pajdušáková (Dello Russo *et al.*, 2019; DiSanti *et al.*, 2017). The (3σ) upper limit for October 10 is similarly sensitive to assumed T_{rot} (Table 4.4), but is consistent with the July measurements assuming $T_{rot} \geq 60$ K, a reasonable assumption given the rotational temperatures measured in July and September for other molecules at similar R_h.

Additionally, an emission spatial profile for CH_4 could not be extracted due to low S/N along the slit; therefore, GFs measured from other species (or co-measured dust) within a given date were assumed for CH_4 in order to calculate global production rates. It is possible that CH_4 outgassing differed day-to-day from that for H_2O, CO, or co-measured

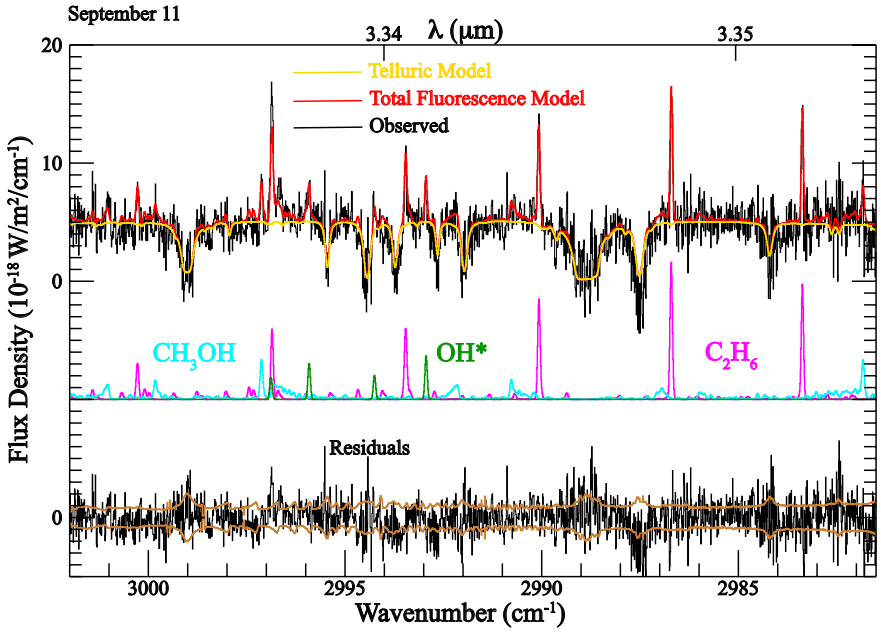

Figure 4.6. Extracted spectra showing detections of C_2H_6, CH_3OH, and OH* on UT 2018 September 11. Analysis of CH_3OH is the subject of a future paper.

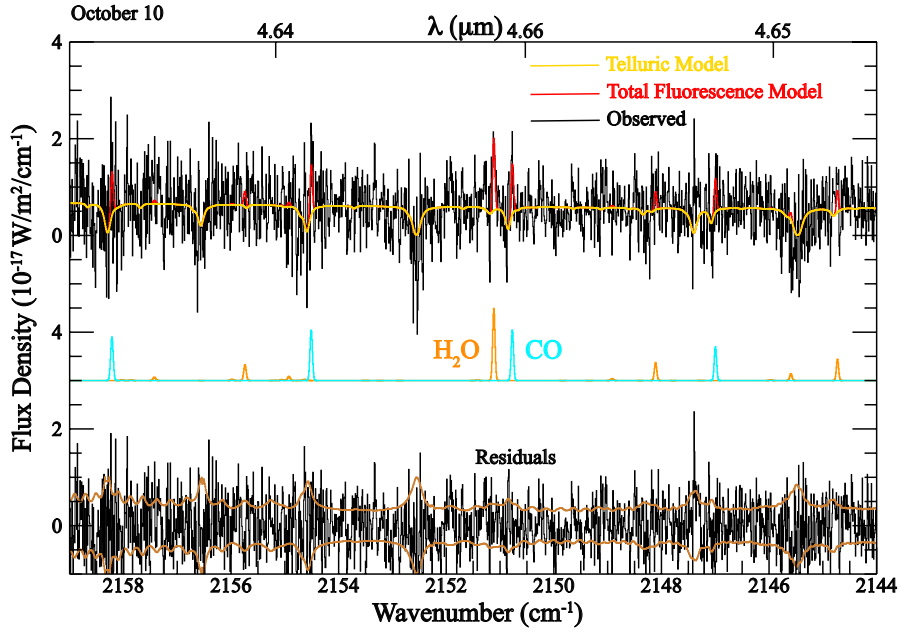

Figure 4.7. Extracted spectra showing detections of CO and H_2O on UT 2018 October 10.

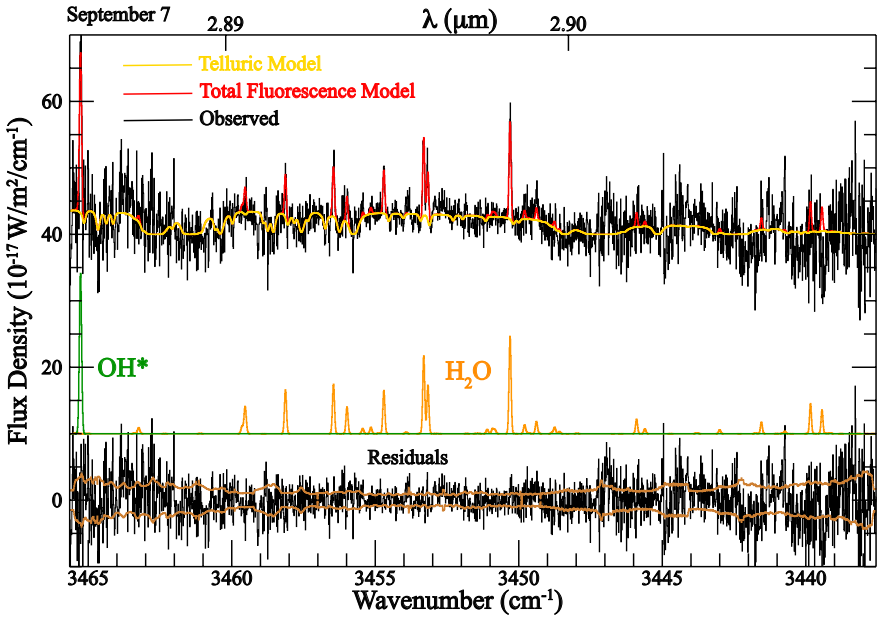

Figure 4.8. Extracted spectra showing detections of H_2O and OH* on UT September 7.

dust, and that the suggested variability may be due the assumed CH_4 GFs. That being said, no unusual outgassing patterns were found among the other molecules or dust relative to one another in G-Z, so the assumed GF for CH_4 should be reasonable.

Finally, OH prompt emission (OH*, see Bonev *et al.* (2006)) was weak in G-Z for July and October dates, and was only firmly detected in September. We therefore calculated mixing ratios using $Q(H_2O)$ obtained from the M2 setting on the same date. The inter-setting calibration uncertainty introduced is estimated to be ~10%, and has been incorporated into the reported uncertainty in the mixing ratios. Use of contemporaneously (but not simultaneously) measured $Q(H_2O)$ for CH_4 abundances in July and October may also account for some of the spread in abundances from date-to-date. However, the formal agreement between $Q(H_2O)$ obtained from both OH* (in Lp1) and H_2O (in Lcustom) on September 7 (Table 4.3) argues against both a systematic difference in retrieving water

production rates in these two ways, and also against short-term variations in $Q(H_2O)$ in G-Z. Clearly, further measurements of G-Z are necessary to clarify the possible variability of its coma CH_4 content.

4.3.3. C_2H_6. Of all the hypervolatiles, C_2H_6 is the most routinely sampled in comets owing to its intrinsically strong near-infrared transitions and the availability of multiple lines in regions of favorable telluric transmittance independent of Δ_{dot}. This enabled measuring C_2H_6 mixing ratios on multiple dates during G-Z's 2018 apparition, including pre-perihelion, near perihelion, and post-perihelion. Similar to CO, C_2H_6 mixing ratios were consistent (within uncertainties) pre-perihelion (weighted average 0.24 ± 0.03% for T_{rot} = 64 K) and additionally near perihelion (weighted average 0.29 ± 0.02%). However, C_2H_6 was lower post-perihelion with mixing ratio 0.14 ± 0.03% (assuming T_{rot} = 60 K). Compared to ecliptic comets measured to date, G-Z was consistent with mean mixing ratios for C_2H_6 (0.34 ± 0.07%) pre-perihelion and near perihelion, but was depleted post-perihelion (severely depleted compared to the mean for all comets measured (0.55 ± 0.08%), including ecliptic comets). In the same manner as CH_4, the use of $Q(H_2O)$ from H_2O in the M2 setting rather than from OH* in the Lp1 setting to calculate C_2H_6 mixing ratios in July and October may have contributed to its suggested variability. However, it is important to note that $Q(H_2O)$ was dramatically lower in October compared with both July and September dates, being closer to 2 x 10^{28} than 3 x 10^{28} molecules s^{-1}, consistent with asymmetry in water production with respect to perihelion found by A'Hearn *et al.* (1995). This in turn could indicate distinct active regions dominating activity in G-Z at these times, and that its chemical composition (at least in terms of CH_4/H_2O and C_2H_6/H_2O) may also be different on October 10 compared with the pre-/near-perihelion dates.

4.4. COMPARISON WITH PREVIOUS PERIHELION PASSAGES AND OTHER COMETS MEASURED

Understanding the implications of the hypervolatile content of G-Z during its 2018 passage, as well as potential variability, requires comparing to published measurements of G-Z from previous perihelion passages, as well as placing G-Z into the context of the comet population measured to date. Each of these is discussed below.

4.4.1. Comparison with Previous Perihelion Passages. G-Z is the only comet surveyed at near-infrared wavelengths during three different perihelion passages: 1998 (Mumma *et al.*, 2000; Weaver *et al.*, 1999), 2005 (DiSanti *et al.*, 2013), and 2018 (Roth *et al.*, 2019), and is just the second comet to have a comprehensive comparison of hypervolatile abundances across apparitions (the other being 2P/Encke; see Radeva *et al.* (2013); Roth *et al.* (2018)). Figure 4.9 shows hypervolatile abundances in G-Z for all three perihelion passages, including measurements for each species by date in 2018. Table 4.5 gives a similar comparison numerically. Figure 4.9 and Table 4.5 suggest that each hypervolatile may display at least some degree of variability, whether across perihelion passages or within a particular apparition. Each species will be discussed in turn.

4.4.1.1. CO. In the case of CO, pre- and post-perihelion mixing ratios are consistent with (but lower than) the upper limit from the 1998 apparition (using CSHELL) found by Weaver *et al.* (1999), but are considerably lower than the mixing ratio reported by Mumma *et al.* (2000) from observations conducted approximately three weeks earlier. However, Mumma *et al.* (2000) did not detect H_2O, even though the strong line near 2151 cm^{-1} (as shown in Figure 4.4) was encompassed together with the CO R0 and R1 lines in the same CSHELL setting. Instead, their value for CO/H_2O was inferred from the measured CO abundance relative to C_2H_6 (detected at the $\sim 5\sigma$ confidence level), and an adopted (1.9σ) value for $Q(H_2O)$ based on residual flux at the Doppler-shifted frequency of the 2151 cm^{-1}

Table 4.5. Hypervolatile Abundances in 21P/Giacobini-Zinner Across Apparitions[1].

Year	Molecule	Pre-perihelion	Perihelion	Post-Perihelion
1998	CO	< 3.2[2] 10 ± 6[3]	–	–
	C_2H_6	< 0.08[2] 0.22 ± 0.13[3]	–	–
2005[4]	C_2H_6	0.14 ± 0.02	–	–
2018[5]	CO	1.72 ± 0.12	–	1.26 ± 0.23
	CH_4	0.63 – 1.52	–	<0.55 – <0.89
	C_2H_6	0.24 ± 0.04	0.29 ± 0.02	0.14 ± 0.03

	Mean among Comets Measured[6]	Range in Comets[7]
CO	6.1 ± 1.6 (19)	0.30 – 2.6
CH_4	0.88 ± 0.10 (19)	0.11 – 1.6
C_2H_6	0.55 ± 0.08 (27)	0.037 – 1.9

[1] Upper limits for non-detected species are 3σ. In all cases values are expressed as % relative to H_2O.

[2] Abundances taken from Weaver *et al.* (1999).

[3] Abundances taken from Mumma *et al.* (2000).

[4] Abundances taken from DiSanti *et al.* (2013).

[5] This work. Abundances for CO and C_2H_6 are given as weighted averages for molecules detected on multiple dates, assuming T_{rot} = 64 K for pre-perihelion values, T_{rot} = 75 K for perihelion values, and T_{rot} = 60 K for post-perihelion values. Owing to its sensitive dependence on T_{rot}, the mixing ratio for CH_4 is given as a range based on the values in Tables 4.2 and 4.4.

[6] Mean values and 1σ uncertainties among measured comets taken from Dello Russo *et al.* (2016a). The number of measurements used to calculate the mean is given in parentheses. Mean values for CO and CH_4 are given for OCCs only owing to the extreme paucity of such measurements in JFCs, whereas the mean for C_2H_6 is given for all comets measured (JFCs and OCCs).

[7] Range among comets measured after Dello Russo *et al.* (2019, 2016a); DiSanti *et al.* (2017); Faggi *et al.* (2018); Roth *et al.* (2018, 2017)

line. In any case, results obtained to date suggest that the abundance ratio of CO in G-Z may display variability, both during a single apparition (as is also suggested by the 2018 measurements) and across multiple apparitions.

It is important to note that the 1998 measurements of G-Z with CSHELL – the small spectral grasp of which precluded measuring H_2O simultaneously with CH_4 or C_2H_6 – introduced uncertainties due to inter-setting calibration in addition to potential temporal

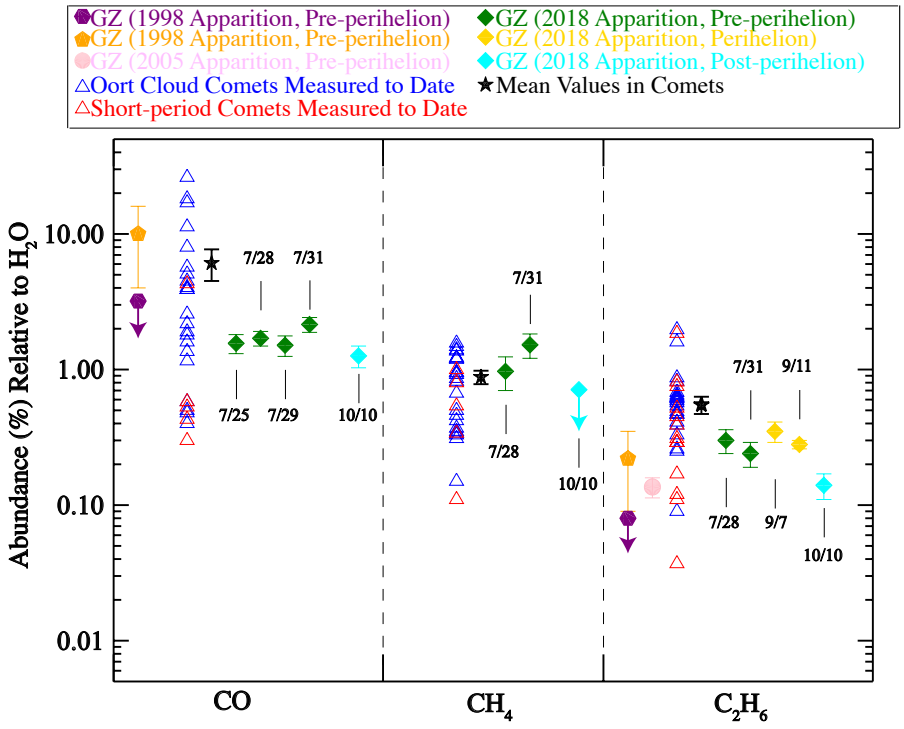

Figure 4.9. Comparison of mixing ratios (%, relative to H_2O) of hypervolatiles sampled in G-Z during the 1998 (purple, Weaver *et al.* (1999); orange, Mumma *et al.* (2000)), 2005 (pink, DiSanti *et al.* (2013)), and 2018 (green, yellow, cyan, Roth *et al.* (2019)) perihelion passages, as well as near-infrared measurements of each volatile in OCCs to date (blue), in ecliptic comets to date (red), and the respective mean values for CO and CH_4 among OCCs and for C_2H_6 among all comets (black, Dello Russo *et al.* (2019, 2016a); DiSanti *et al.* (2017); Faggi *et al.* (2018); Roth *et al.* (2018, 2017). Error bars indicate measurements, whereas downward arrows indicate 3σ upper limits.

variations in production rates. In contrast, the large spectral grasp of iSHELL enabled simultaneous measurements of all three hypervolatiles with either H_2O or OH* during the 2018 perihelion passage of G-Z.

In the context of preserving natal solar system signatures in the nucleus ices of JFCs, it is important to note the stark contrast of the 2018 CO measurements along with those reported by Weaver *et al.* (1999) compared to those of Mumma *et al.* (2000). The CO/H_2O mixing ratio inferred by Mumma *et al.* (2000) (10 ± 6%) places G-Z as the only known

CO-enriched JFC to date. If G-Z were indeed so enriched in CO, it would have profound implications for the origins and evolutionary processing history of JFCs. However, as mentioned previously this is based on an extremely tentative "detection" ($< 2\sigma$) of H_2O. Nonetheless, the 2018 measurements do not support this conclusion, and instead indicate that G-Z has a CO abundance that is similar compared to the few measurements in ecliptic comets, and is depleted when compared to all comets measured.

4.4.1.2. CH_4. CH_4 has not been reported previously in G-Z – for both the 1998 and 2005 observations $|\Delta_{dot}| < 10$ km s^{-1}, thereby precluding its measure – but the results reported here indicate that it may have been variable on timescales of days to months in 2018. However, as previously noted, there are important caveats regarding its purported variability. In any case, these measurements indicate that G-Z is consistent-to-enriched compared to the mean CH_4 abundance for all comets measured.

4.4.1.3. C_2H_6. The C_2H_6 mixing ratios obtained pre-perihelion and near perihelion in 2018 were consistent with that found by Mumma *et al.* (2000), but were considerably enriched compared to the upper limit reported by Weaver *et al.* (1999), as well as compared to the measurement from 2005 (0.14% DiSanti *et al.* (2013)). However, the post-perihelion measurement for C_2H_6 on October 10 was considerably lower (by approximately a factor of 2) than earlier 2018 dates, yet consistent with the 2005 pre-perihelion value, suggesting possible short-term (i.e., "diurnal", perhaps associated with nucleus rotation, or seasonal, such as that seen by Rosetta at 67P/Churyumov-Gerasimenko; see Section 4.4.2) variability in its C_2H_6 abundance ratio when compared with pre-perihelion results. It is important to note that the possible variability in C_2H_6 within the 2018 G-Z measurements (as well as those from previous perihelion passages) is small compared to the overall spread of C_2H_6 abundances in all comets measured (Figure 4.9).

4.4.2. Discussion of Possible Variability of Coma Hypervolatile Abundances in G-Z. Combined with previous work, the 2018 results suggest that coma hypervolatile abundances in G-Z may be variable. At 67P/Churyumov-Gerasimenko, the Rosetta mission

found that nucleus shape and the location of active areas, combined with seasonal and rotational illumination effects, resulted in coma compositional variability on a variety of timescales. Hässig *et al.* (2015) found long-term variation in the coma abundances of CO and CO_2 due to seasonal illumination effects; furthermore, other species (such as CH_4) varied on smaller timescales, showing diurnal variations that differed from those of other volatiles, such as CO and C_2H_6 (Bockelée-Morvan *et al.*, 2016; Fink *et al.*, 2016; Luspay-Kuti *et al.*, 2015). Similar effects may have contributed to the suggested coma hypervolatile variability in G-Z. Unfortunately, the ground-based measurements reported here do not have sufficient spatial resolution to determine whether this was the case.

To further examine the nature of the suggested variability in G-Z, the evolution of molecular production rates for each species reported here during the 2018 apparition was evaluated. Figure 4.10 shows the production rate of each species relative to perihelion (September 10). The measurements for all four species (H_2O,CO, CH_4, C_2H_6) agree with A'Hearn *et al.* (1995), who found that G-Z was more active pre-perihelion than post-perihelion. However, these results indicate that the relative asymmetry in molecular production is shaper for the trace species than for H_2O, which is reflected in the general depletion of their post-perihelion mixing ratios compared to pre-perihelion values (Figure 4.9, Table 4.5.

In order to test whether the possible variability indicated by the 2018 results is owing to the activity of H_2O vs. that of the trace species in G-Z, the ratios CO/C_2H_6 were compared. CO/C_2H_6 was found to be consistent within uncertainties pre- vs. post-perihelion, being 7.18 ± 2.14 on July 28, 8.82 ± 1.69 on July 31, and 8.75 ± 1.85 on October 10 (assuming $T_{\rm rot}$ = 64 K for July and 60 K for October). Combined with results shown in Figures 4.9 and 4.10, this suggests that although CO and C_2H_6 were consistent relative to one another throughout the 2018 perihelion passage, their contributions to the volatile content of the coma were not, as evidenced by their steeper variation about perihelion than H_2O.

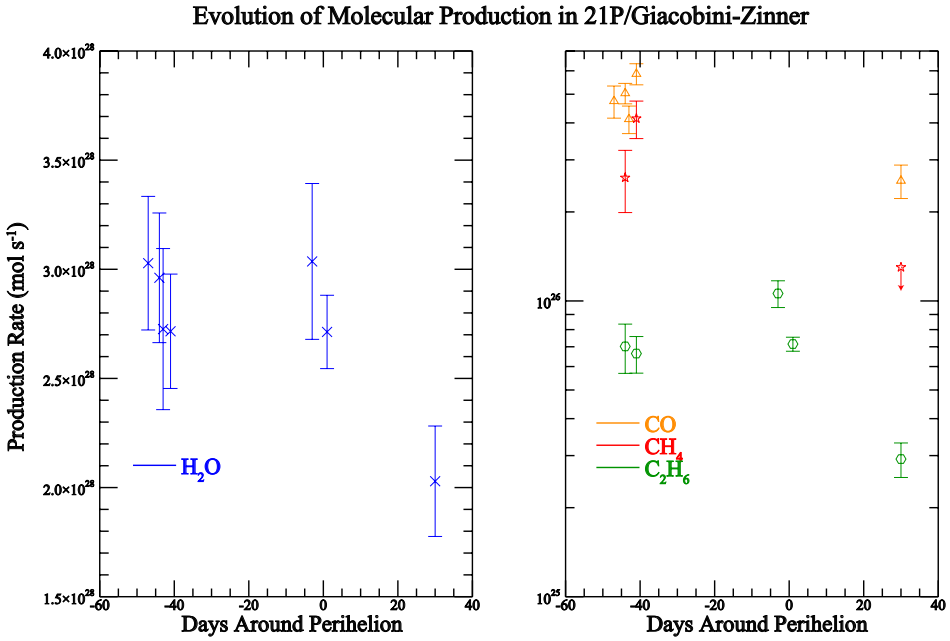

Figure 4.10. Evolution of molecular production in G-Z throughout the 2018 perihelion passage for H_2O (left panel) and CO, CH_4, and C_2H_6 (right panel) with respect to perihelion (UT 2018 September 10). Error bars indicate measurements, whereas downward arrows indicate 3σ upper limits.

If G-Z is indeed variable, it is not the first such comet reported in the literature. As the number of serial measurements (i.e., both within and across perihelion passages) of primary volatiles in ecliptic comets increases, the number of reports of variability on multiple timescales has similarly increased (e.g., Dello Russo *et al.* (2019); Fink *et al.* (2016); Roth *et al.* (2018); Bodewits *et al.* (2014); DiSanti *et al.* (2016); Feaga *et al.* (2014); McKay *et al.* (2015)), with explanations ranging from diurnal variations in outgassing, to seasonal illumination effects, to chemically heterogeneous nuclei. Understanding whether such variations are common or rare phenomena and how to account for them during analysis is crucial to placing the results of present-day primary volatile measurements in cometary comae into the framework of solar system formation theories.

It is important to note that the variability suggested by the measurements in Table 4.5 cannot explain the variation in each molecule among comets revealed in measurements to date (Figure 4.9). If the range of volatile abundances observed among all comets can be reproduced by time-resolved measurements of one comet, it would seriously call into question whether the chemical diversity among the population is cosmogonic. Alternatively, a comet such as G-Z, in which measurements over three perihelion passages suggest (with carefully explored caveats) that the abundances of CO/H_2O and C_2H_6/H_2O vary on scales much smaller than the comet-to-comet range, may serve as evidence that cosmogonic signatures are indeed being sampled in present-day measurements of parent volatiles in short-period comets. Further unraveling the complex relationship between nascent solar system conditions and evolutionary processes in comets clearly requires increasing the sample size of serial measurements in short-period comets, particularly observations targeting the hypervolatiles.

4.5. COMPARISON WITH OTHER COMETS MEASURED

Comprehensive hypervolatile abundances have been securely measured in 19 OCCs to date, yet in only four ecliptic comets, including G-Z. This highlights that statistics for these species in ecliptic comets (particularly CO and CH_4) are far from being firmly established. Figure 4.11 shows relative hypervolatile abundances reported in all comets to date, including G-Z and in-situ measurements taken by Rosetta at 67P/Churyumov-Gerasimenko using ROSINA measurements of C_2H_6 (Le Roy *et al.*, 2015), MIRO measurements of CO (Biver *et al.*, 2019), and VIRTIS measurements of CH_4 (Bockelée-Morvan *et al.*, 2016). The particularly low C_2H_6/CH_4 ratio in G-Z (#22-24) is supported by observations at other wavelengths. Kiselev *et al.* (2000) reported a blueish linear polarization spectrum for continuum in G-Z at optical wavelengths, and suggested this was caused by the presence of organic grains (or large-sized complex organics). This implies that G-Z is depleted in simple organics, such as C_2H_6, but enriched in more complex organics, which may indicate

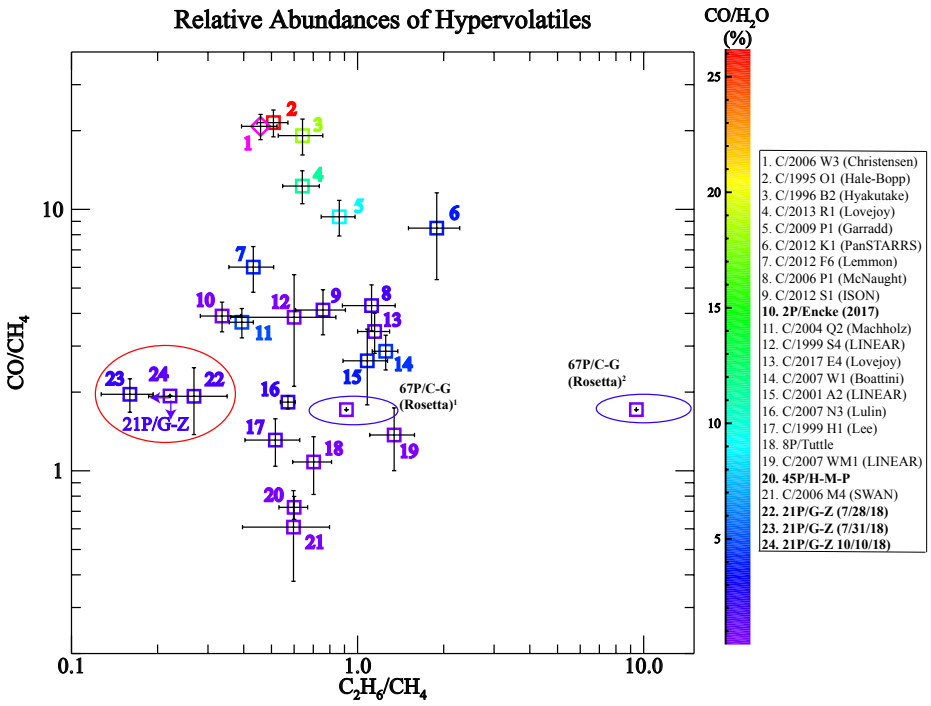

Figure 4.11. Ratios of hypervolatiles in comets characterized to date, including comets G-Z (Roth *et al.*, 2019), 67P/Churyumov-Gerasimenko (Biver *et al.*, 2019; Bockelée-Morvan *et al.*, 2016; Le Roy *et al.*, 2015), 45P/Honda-Mrkos-Pajdušáková (DiSanti *et al.*, 2017), C/2006 W3 (Christensen) (Bonev *et al.*, 2017), C/2012 K1 (PanSTARRS) (Roth *et al.*, 2017), C/2017 E4 (Lovejoy) (Faggi *et al.*, 2018), 2P/Encke (Roth *et al.*, 2018), and 16 OCCs (after Dello Russo *et al.* (2016a)). Values for G-Z were taken from each of the three dates for which all three hypervolatiles were sampled, and assuming $T_{\rm rot}$ = 64 K for July dates and $T_{\rm rot}$ = 60 K for October 10. For the October date, the downward- and leftward-facing arrows indicate the (3σ) upper limits CO/CH_4 and C_2H_6/CH_4. Owing to the sensitive dependence of $Q(CH_4)$ on assumed $T_{\rm rot}$, the red oval traces the total possible spread in G-Z's hypervolatile content for the range $T_{\rm rot}$ = 48 – 70 K. Each comet is color-coded by its mixing ratio CO/H_2O. [1] Values for 67P using C_2H_6/H_2O as reported in Le Roy *et al.* (2015) for the northern hemisphere. [2] Values for 67P using C_2H_6/H_2O as reported in Le Roy *et al.* (2015) for the southern hemisphere. In both cases, the blue ovals trace the total possible spread in 67P's hypervolatile content.

warmer conditions were present during the formation and subsequent evolution of G-Z's constituent ices. The low measured C_2H_6/CH_4 supports this hypothesis, and together with the observed blueish polarization, may indicate that simple hydrocarbons were efficiently converted into more complex organics in G-Z.

It is apparent from Figure 4.11 that hypervolatile abundances among OCCs span a large range of values. Similarly, as the hypervolatile abundances of more ecliptic comets are completely characterized, it appears that they may span the same range of CO/CH_4 and C_2H_6/CH_4 as observed in OCCs, from severely depleted (45P/Honda-Mrkos-Pajdušáková, #20 in Figure 4.11; DiSanti *et al.* (2017)) to near-mean values (2P/Encke, #10; Roth *et al.* (2018)) to the (possibly) enriched values measured in 67P/Churyumov-Gerasimenko (Biver *et al.*, 2019; Bockelée-Morvan *et al.*, 2016; Le Roy *et al.*, 2015). It is important to note that comparisons between the in-situ measurements of Le Roy *et al.* (2015) and bulk coma measurements (e.g., Biver *et al.* (2019); Bockelée-Morvan *et al.* (2016); Roth *et al.* (2019)) are not straightforward, particularly given the differences in R_h between each set of measurements.

The relative isolation of G-Z on the graph further highlights the spread in hypervolatile abundances among ecliptic comets, reflecting its unique combinations of CH_4 being consistent with the mean for OCCs versus the moderately depleted values for CO and C_2H_6. This underscores that much work remains in firmly characterizing the ranges of hypervolatile abundances in ecliptic comets and understanding their implications for placing such measurements into a meaningful context.

4.6. SUMMARY OF RESULTS FOR 21P/GIACOBINI-ZINNER

The hypervolatile composition of the prototypical "GZ-type" comet 21P/Giacobini-Zinner was characterized with the powerful, recently commissioned iSHELL spectrograph at the NASA-IRTF on four dates pre-perihelion, two dates near perihelion, and one date post-perihelion. Combined with previous work, the results suggest that coma abundances of all three hypervolatiles (CO, CH_4, and C_2H_6) may be variable on several timescales, including day-to-day, pre- vs. post-perihelion, and even across perihelion passages. However, as noted

in Section 4.3, there are important caveats to this study, and additional serial measurements of G-Z are needed to confirm possible variability in its coma hypervolatile content. In any case, the results reported here suggest that:

1. Mixing ratios of CO were consistent (within uncertainty) day-to-day pre-perihelion, but were slightly lower post-perihelion. These measurements are consistent with depleted values in comets measured, as well as with an upper limit derived from the 1998 perihelion passage (Weaver *et al.*, 1999).

2. The measurements of CH_4, the most severely underrepresented hypervolatile in studies of ecliptic comets, represent its first reported values in G-Z. CH_4 abundances were consistent with mean values among all comets measured, and may have been variable from day-to-day. However, there are important caveats to the possible variability of CH_4 in G-Z (Section 4.3).

3. C_2H_6 was found to decrease significantly pre- vs. post-perihelion, and its post-perihelion value was consistent with being depleted. The pre-perihelion C_2H_6 mixing ratios were enriched compared to measurements during the same seasonal phase in 2005 (DiSanti *et al.*, 2013), yet the post-perihelion mixing ratio was consistent with the results from 2005.

4. If G-Z is indeed variable, the spread between the measurements reported here, as well as between those from previous perihelion passages, is significantly smaller than the variation in each molecule among all comets measured (Figure 4.9). This may be evidence that natal conditions dominate over evolutionary effects due to successive perihelion passages in setting the composition of short-period comets.

Understanding the cause(s) of the considerable spread in hypervolatile abundances seen in Figure 4.11 is necessary to disentangle primordial from evolutionary effects in setting the present-day (observed) abundances of hypervolatiles (and of primary volatiles in general)

in comets. On the one hand, chemical models of protoplanetary disks (e.g., Drozdovskaya *et al.* (2016); Willacy *et al.* (2015)) predict that comets incorporated a wide range of hypervolatile abundances from their formation region(s) in the protosolar nebula. On the other hand, the nontrivial effects of heterogeneous outgassing and seasonal illumination on coma composition, such as that seen by Rosetta at 67P (i.e., Bockelée-Morvan *et al.* (2016); Feldman *et al.* (2018); Fougere *et al.* (2016a,b); Hässig *et al.* (2015); Luspay-Kuti *et al.* (2015)), cannot be overlooked. This emphasizes the high impact of serial observations of comets, particularly those targeting hypervolatiles in ecliptic comets, which may be most indicative of the role that primordial vs. evolutionary effects play in setting the composition of comets. Thankfully, the availability of next-generation instruments such as iSHELL, capable of delivering the long on-source integration times and excellent sensitivity required for such measurements, is enabling a better understanding of the interplay between nascent solar system conditions, evolutionary processing, and coma compositional variability when interpreting the results of primary volatile studies in comets.

5. A SUMMARY OF THIS WORK AND A LOOK TO THE FUTURE OF COMETARY SCIENCE

5.1. MAJOR SCIENCE GOALS ADDRESSED BY THIS DISSERTATION

This dissertation is comprised of the results of six observing programs spread over 5 years. These results have either been published (Roth *et al.*, 2018, 2017) or submitted for publication (Roth *et al.*, 2019) in peer-reviewed academic journals. This section will identify the major science goals addressed in each work and place these goals into the context of cometary science at the time of their undertaking, as well as give an overview of future work and opportunities in the field.

5.1.1. The Composition of Comet C/2012 K1 (PanSTARRS) and the Distribution of Primary Volatile Abundances Among Comets. Roth *et al.* (2017) was written and published during an exciting, yet challenging time in recent cometary science. The number of comets characterized with near-infrared spectroscopy had recently reached 30, and unexpected results from the Rosetta mission to comet 67P/Churyumov-Gerasimenko were appearing in earnest in the literature. The paradigm in studies of primary volatiles at near-infrared wavelengths was that the primary volatile composition of the coma at any given time could be used to infer the native composition of the nucleus, which in turn could be tied to nascent solar system conditions. Yet as detailed in this dissertation, the Rosetta spacecraft found a comet whose primary volatile composition varied on multiple time scales.

Furthermore, comets were classified based on their primary volatile content as"organics-enriched","organics-normal", or "organics-depleted" (Mumma and Charnley, 2011). Yet as the number of comets measured increased, so did the number of "atypical" comets: those which were enriched in some primary volatiles, normal in others, and depleted in the rest. These comets could not be accommodated by any of the proposed taxonomic classes.

Furthermore, the definition of enriched, average, or depleted was a frequently changing goalpost, with taxonomic classes defined by arbitrary cutoffs based on comets measured to date (Dello Russo *et al.*, 2016a). With each new comet characterized, mean abundances in the measured population changed, and hence the bounds of taxonomic classes.

Roth *et al.* (2017) found that comet C/2012 K1 (PanSTARRS) was another example of an "atypical" comet: enriched for CH_3OH and C_2H_6, depleted for H_2CO, CH_4, and possibly C_2H_2, yet consistent with normal for CO and HCN. To place the primary volatile content of "atypical" comets such as C/2012 K1 (PanSTARRS) into the framework of probing solar system formation conditions, Roth *et al.* (2017) examined the nature of abundances for individual volatiles in comets measured to date rather than all volatiles simultaneously. They found that results to date suggested that well-sampled volatiles (such as HCN) formed a continuous distribution of abundances among the comet population (Figure 2.7). In the case of C_2H_6, a volatile that was well-sampled yet still showed a gap between "normal" and "enriched", the C_2H_6 abundance of C/2012 K1 (PanSTARRS) filled in this gap and suggested a continuous distribution of C_2H_6 abundances among comets. This in turn suggested that other volatiles that were either well-sampled but with "gaps" (e.g., CH_3OH) or under-sampled (e.g., CH_4) may also display a continuous distribution of abundances among the population as more comets are characterized.

5.1.2. A Tale of "Two" Comets: The Primary Volatile Composition of Comet 2P/Encke Across Apparitions and Implications for Cometary Science. Roth *et al.* (2018) reported the results of early comet observations with the new near-infrared spectrograph iSHELL at the NASA-IRTF after its commissioning in December 2016. These observations came during the midst of a 3-year period from 2016-2018 which featured unusually favorable apparitions of multiple short-period comets, including 2P/Encke, 45P/Honda-Mrkos-Pajdušáková, 41P/Tuttle-Giacobini-Kresak, 21P/Giacobini-Zinner, and 46P/Wirtanen. Each of these comets made perihelion passages featuring small geocentric distance simultaneously with high geocentric velocity, and in several cases, small heliocentric distance. These

circumstances represented rare observational occurrences for ecliptic comets: 2P/Encke will not make a similar apparition until 2026, and 46P/Wirtanen will not make as favorable of an apparition for at least another 75 years. As detailed in Sections 3 and 4, this presented an outstanding and timely opportunity to address pressing questions in cometary science regarding the properties of ecliptic comets.

Roth *et al.* (2018) capitalized on these favorable circumstances to make the first comprehensive comparison of primary volatile abundances in a comet across multiple apparitions, as well as to secure measurements of the hypervolatiles CO and CH_4, whose abundances are severely underrepresented in studies of short-period comets. These measurements revealed yet another "atypical" comet, including the most severely depleted C_2H_6 in a comet observed to date, yet HCN and H_2CO consistent with normal. Furthermore, Roth *et al.* (2018) found dramatic changes in the primary volatile content of 2P/Encke's coma in 2017 compared to measurements from the 2003 perihelion passage (Radeva *et al.*, 2013), and reinforced the findings of the Rosetta mission that coma composition may vary in comets on several timescales. This highlighted the importance of serial measurements of comets, which have become increasingly feasible owing to the capabilities of newer advanced instruments, such as iSHELL. Furthermore, these measurements provided just the third complete hypervolatile inventory for an ecliptic comet, and contributed to establishing statistics for these species in this important comet subclass. As noted earlier, understanding hypervolatile abundances in ecliptic comets may provide a path for disentangling natal conditions from evolutionary processes in setting the present-day volatile composition of short-period comets (Dello Russo *et al.*, 2016a).

5.1.3. Probing the Evolutionary History of Comets: An Investigation of the Hypervolatiles CO, CH_4, and C_2H_6 in the Jupiter-family Comet 21P/Giacobini-Zinner. With its 2018 perihelion passage being the most favorable in the last 35 years, 21P/Giacobini-Zinner presented an opportunity to build on the results found by Roth *et al.* (2018) in 2P/Encke. 21P/Giacobini-Zinner had been observed in two previous perihelion passages

(DiSanti *et al.*, 2013; Mumma *et al.*, 2000; Weaver *et al.*, 1999), but these observations resulted in limited primary volatile inventories. With the availability of iSHELL, Roth *et al.* (2019) were able to conduct a comprehensive hypervolatile inventory of 21P/Giacobini-Zinner throughout its 2018 apparition, representing the first instance of primary volatile measurements of a given comet across three apparitions, as well as providing the fourth complete hypervolatile catalog of an ecliptic comet. Roth *et al.* (2019) found a comet depleted in CO and C_2H_6, yet with average-to-enriched CH_4. Additionally, these results indicated that the coma hypervolatile composition of 21P/Giacobini-Zinner may have been variable on multiple timescales, including from day-to-day, pre- vs. post-perihelion, and even across apparitions. However, the variation between these measurements (as well as between those from previous apparitions) was a fraction of the spread in each hypervolatile revealed among the comet population by measurements to date. As detailed in Section 4, this suggests that natal conditions may dominate over evolutionary effects due to repeated (and frequent) perihelion passages in setting present-day primary volatile composition, and represented an important step in determining the degree to which primary volatile studies in comets are sampling cosmogonic signatures.

5.2. THE NEXT GENERATION OF COMETARY ASTRONOMY

The combination of new/upgraded and upcoming state-of-the-art instruments, such as the Atacama Large Millimeter/Submillimeter Array (ALMA), iSHELL, NIRSPEC-2, and the James Webb Space Telescope (JWST) is enabling the next generation of cometary astronomy. These facilities are enabling searches for novel and less-understood behaviors in comets, such as compositional variability and small R_h studies (iSHELL), the detection and mapping of complex organics and tests of isotopic ratios in moderately bright comets (ALMA), and testing coma composition and spatial associations with unprece-

dented sensitivity and at large R_h (JWST). The work in this dissertation will be continued and complemented by postdoctoral research addressing these topics, and each will be briefly discussed.

5.2.1. Revealing Spatial Interrelationships among Volatiles. Differentiating parent species from products is critical for inferring nucleus composition from detected volatiles. Notably, the coma distributions of several common molecules (recent examples include H_2CO and HNC in comet ISON; Cordiner *et al.* (2014)) are inconsistent with release by direct sublimation alone, suggesting the presence of unidentified parents (Cottin and Fray, 2008). Rosetta detected nonvolatile organic macromolecular materials on the surface of comet 67P (Capaccioni *et al.*, 2015), which may be the parent sources for some of these distributed species. Other molecules, such as H_2CO, have been suggested to originate form thermal degradation of polymers in some cases (Cordiner *et al.*, 2014; Fray *et al.*, 2006). However, much work remains to firmly understand the sources of many coma volatiles, including important prebiotic molecules.

These questions can be addressed by spatial-spectral studies with long-slit, near-infrared spectrographs such as iSHELL (examples of such studies are shown in this work) and with radio facilities such as ALMA. With its high angular resolution, ALMA has the unique ability to generate three-dimensional spatial maps of gases within ~300 to several thousand km of the nucleus, and the high spatial resolution afforded by long-slit IR measurements enables studying how species are released from the nucleus and possible additional sources through their derived column densities along the slit. Comparing the sources for different species is essential for understanding the origin of each volatile and whether they are associated with nucleus sources (and hence can be related to formation conditions). By understanding the origin of coma volatiles and how volatiles might be associated or segregated in nucleus ices, future work with instruments such as iSHELL and ALMA will address a fundamental question in post-Rosetta cometary science: *How are comet ices put together?* (A'Hearn, 2017).

5.2.2. Testing for Isotopic Fractionation and Complex Organics in Comets. Decrypting the clues of solar system formation that are imprinted in the ices of cometary nuclei requires an understanding of the formation circumstances and history of cometary material. Testing isotopic ratios in coma volatiles provides a powerful tool for unraveling this history, as isotopic fractionation is sensitive to the prevailing conditions during their assembly, including temperature and processing. Isotopic ratios measured in comets (e.g., Bockelée-Morvan *et al.* (2015)) include D/H, $^{32}S/^{34}S$, $^{12}C/^{13}C$, $^{14}N/^{15}N$, and $^{16}O/^{18}O$. A significant deviation of these ratios in comets from solar values could indicate that their material experienced isotopic fractionating during solar/planet formation, or even earlier. For instance, excesses of heavy hydrogen and nitrogen are favored in very low temperature environments, as evidenced by deuterium enrichment in the interstellar medium and heavy nitrogen enrichment toward dark cloud cores (Bockelée-Morvan *et al.*, 2015; Milam *et al.*, 2015). Significantly, cometary isotopic ratios show signs of such fractionation in D and ^{15}N, suggesting a heritage from a very low temperature environment, perhaps interstellar. However, isotopic ratios of carbon, sulfur, and oxygen in comets are generally consistent with solar values (Bockelée-Morvan *et al.*, 2015), leaving the question unresolved and requiring a larger sample of isotopic fractionation measurements to determine whether cometary material is consistent with an interstellar origin, nebular material, or both.

Isotopic fractionation studies can be complemented by measuring the abundances of complex organic molecules (COMs) in comets. COMs, such as glycoaldehyde and formamide, have been detected in comets and can be formed via grain-surface reactions in cold prestellar cores, or later in the protoplanetary disk; thus, the abundances of COMs in comets can provide insights into whether their nuclei have incorporated material from the protosolar nebula or even earlier by comparison with their abundances in interstellar sources and with chemical models of dark clouds and protoplanetary disks (Biver, 2015). Future work will test isotopic fractionation and for the presence of complex organics in comets by targeting their rotational transitions with facilities such as ALMA.

5.2.3. Probing Coma Composition at Large R_h. The James Webb Space Telescope (JWST) is scheduled to become operational in 2021, and JWST-based comet observations will form a portion of the author's postdoctoral research. JWST will provide highly complementary results to ground-based observations of comets. JWST will be particularly powerful for observing comets at $R_h > 3$ AU and at excellent spatial resolution (Kelley *et al.*, 2016), enabling studies of coma volatile composition and spatial distributions at heliocentric distances that are often out of reach to ground-based IR and sub-mm observatories. JWST will also enable comprehensive studies of CO_2 in comets, a primary driver for cometary activity along with H_2O and CO, but which is unobservable from the ground and therefore not well understood (Kelley *et al.* (2016) and refs. therein). JWST will enable simultaneous or contemporaneous studies of the abundances and spatial distributions of all three species in comets over a range of R_h, providing highly complementary results to the ground-based spatial studies conducted at smaller R_h and dramatically improving the understanding of cometary behavior over all portions of an orbit.

5.3. FINAL REMARKS

Cometary science in the era after the Deep Impact, EPOXI, and Rosetta missions can be best described as searching for how (or whether) the properties and behaviors of comets change with time. The results of these missions have led to fundamental questions (posed by A'Hearn (2017)) regarding the nature of comets: To what degree do comets retain cosmogonic signatures in their nuclei? How are comets ices put together? How do comets change with time? Are the behaviors seen by these missions exceptional or common? The results reported in this work seek to address these questions by characterizing the primary volatile composition of three comets, and using these results to decode the history of volatile matter in the early solar system.

APPENDIX A

OBSERVATIONS AND DATA REDUCTION PROCEDURES

OVERVIEW

This appendix serves to a provide a more detailed description of the observational techniques and data reduction procedures applied in cometary near-infrared spectroscopy in this work as outlined in Section 1.6. This appendix will also serve to familiarize the reader with the NIRSPEC and iSHELL spectrographs used for data collection. As previously mentioned, these observational techniques and reduction algorithms have been rigorously tested and are documented in the refereed literature (see Section 1.6 for citations). Rather than a comprehensive examination, this appendix will focus on the aspects most pertinent to the data in this work, notably the recent upgrades made to the algorithms to allow processing of iSHELL frames.

OBSERVATIONAL TECHNIQUES

The observational techniques used to gather near-infrared spectroscopic data for this work are commonly used and well-known in astronomy. Exposures were acquired with state-of-the-art near-infrared spectrographs mounted on large telescopes at professional observatories: NIRSPEC at the 10 m W. M. Keck Observatory and iSHELL at the 3 m NASA Infrared Telescope Facility, both on Maunakea, HI. In all cases, exposures were acquired following the sequence "A1, B1, B2, A2" and combined for analysis as "A1-B1-B2+A2". Figure A.1 illustrates what "A" and "B" frames correspond to in terms of the instrument and target object.

The majority of the data in this work were gathered using "on-chip" nodding, in which the A and B beam positions are placed symmetrically about the midpoint of the slit and separated by half its length. In this procedure, the comet is first placed in the "A" position and an exposure (A1) is taken. The telescope then performs a nod, placing the comet in the "B" position along the slit and taking a second exposure (B1). A second B-frame exposure is taken (B2) and the telescope is then nodded back to the A position for

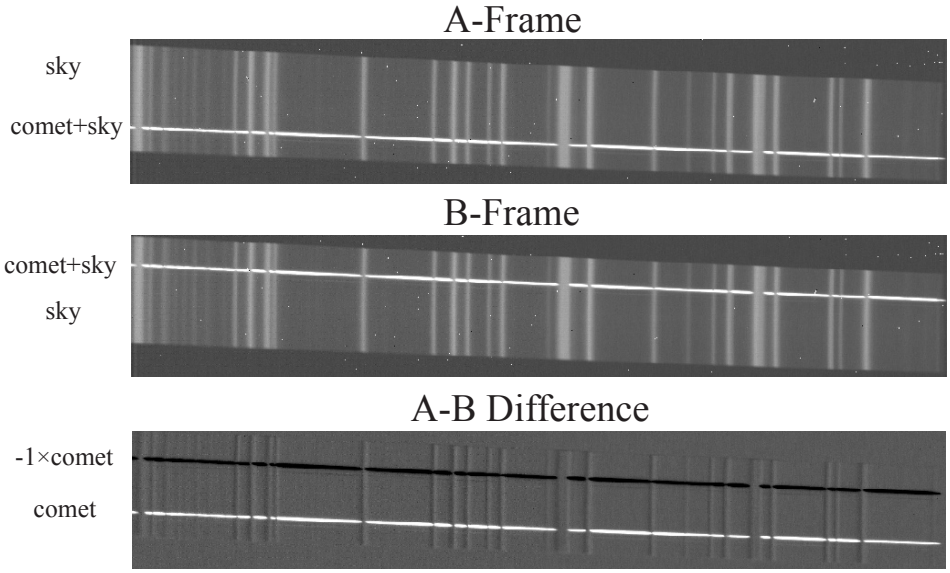

Figure A.1. Order 23 in the KL1 setting of the NIRSPEC spectrograph, showing an "A" frame, a "B" frame, and their difference. The slanted, white horizontal streak in the A and B frames is the comet signal. The vertical bands superimposed on this signal are sky emission lines. Note that these sky lines have been canceled out in the A-B difference frame, leaving only comet signal at the A-position and its negative at the B-position.

the final A frame (A2). In an "A" frame, the slit contains signal from the comet as well as thermal background and "sky" emissions (lines and continuum) at the A-position along the slit, while only containing thermal background and sky emissions at the B-position. In the following "B" frame, the slit contains only thermal background and sky emissions at the A-position, but now contains comet signal, thermal background, and sky emissions at the B-position. The same is true for the second B and A exposures. Combining these frames as "A1-B1-B2+A2" cancels emissions from the thermal background, instrumental biases, and sky emissions to second order in air mass, resulting in a frame which contains purely comet signal at the A-position and its negative at the B-position.

A comparable procedure is used for "off-chip" nodding. Off-chip nodding was necessary for iSHELL observations of comet 21P/Giacobini-Zinner in September 2018, when a malfunction of the iSHELL dekker caused the slit length to be fixed at 5″. The

iSHELL slit length can be interchanged during normal operations, with available slit lengths of 5″, 15″, and 24″. With the exception of the September 2018 21P/Giacobini-Zinner observations, all iSHELL data presented in this work were acquired with the 15″ long slit. Owing to the sole availability of the 5″ during the September 2018 observations, observations were performed with off-chip nodding, wherein the comet was placed at the midpoint of the slit for "A" frames and the telescope was nodded 20″ perpendicular to the slit for "B" frames. Exposures were combined in the same manner as on-chip nodding, but the total time on-source is reduced a factor of two for off-chip nodding (owing to the B frames containing only "sky" signal). Additionally, the spatial extent of measurements along the slit was reduced by a third.

Dark and flat field frames were also taken for every comet set acquired with a particular instrument setting. The dark frames correct for high dark current pixels (the response of the chip to an absence of illumination) and the flat field frames correct for the response of the chip to a uniform illumination source (in this case, a flat lamp inside of each spectrograph). In addition, "standard star" sets are taken for each comet setting to achieve flux calibration: converting instrument counts (ADU) to flux density ($W/m^2/cm^{-1}$) through a derived calibration factor, Γ ($W/m^2/cm^{-1}/ADU/s$). Standard stars are stellar sources with well-constrained magnitudes in the wavelength region of interest (L, L', and M for this work) that are available at similar air mass and right ascension (preferably within 2^h) to that of the comet. Darks and flats are taken for each standard star setting as well. A typical observing sequence may be (using iSHELL settings L1 and Lp1): L1 comet, L1 comet darks, L1 comet flats, L1 standard star, L1 star darks, L1 star flats, Lp1 standard star, Lp1 star darks, Lp1 star flats, Lp1 comet, Lp1 comet darks, Lp1 comet flats.

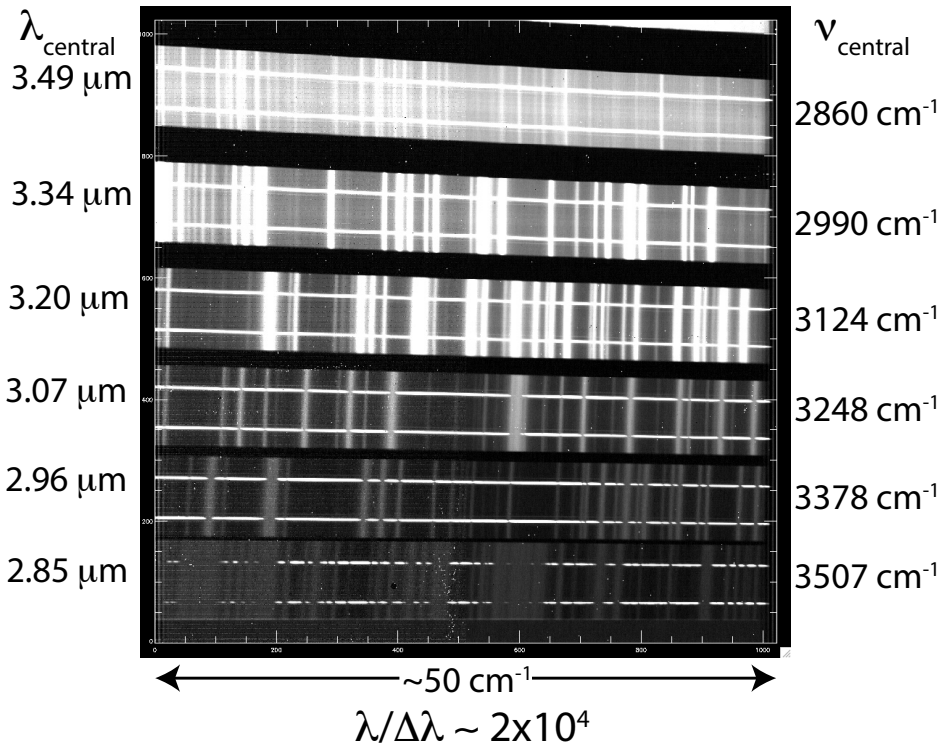

Figure A.2. The KL1 setting of NIRSPEC, including the frequency range of each echelle order, showing its piece-wise continuous spectral coverage.

THE NIRSPEC AND ISHELL SPECTROGRAPHS

To familiarize the reader with the spectrographs used in this work, a brief description of each will be given. NIRSPEC is a high-resolution ($\lambda/\Delta\lambda \sim$ 20,000), cross-dispersed, piece-wise continuous, near-infrared echelle spectrograph with a 1024x1024 pixel array. Figure A.2 shows the full KL1 setting (Orders 22-27) taken with NIRSPEC, along with the frequency range of each echelle order. In four instrument settings, NIRSPEC allows many transitions of all molecules targeted in this work to be sampled simultaneously with either H_2O or its proxy, OH*, significantly reducing systematic uncertainty in derived mixing ratios.

The other spectrograph employed in this work, iSHELL, is very similar to NIRSPEC; however, it features higher resolving power ($\lambda/\Delta\lambda \sim$ 40,000), a larger (2048x2048) array, and has nearly continuous wavelength coverage in the L, L', and M bands (i.e., between

roughly 2.8 μm and 5 μm). Additionally, iSHELL is capable of daytime observations with near-infrared active guiding (in fact, IRTF is currently the only near-infrared observatory to offer daytime observing). Combined with its high observing efficiency (even at M band), the capabilities of iSHELL have dramatically increased the number of observable comets, and enabled serial, long on-source integrations of targets. These observations are enabling searches for and improved understanding of novel behaviors and properties of comets, including coma compositional variability, heterogeneous outgassing, and detections of underrepresented species in cometary studies. Figure A.3 shows the full LP1 setting of iSHELL, including its "bowed" orders, along with the frequency range of each order. The large spectral grasp of iSHELL allows for up to dozens of strong lines of targeted species to be sampled within a single setting. Since each echelle order within a setting is captured simultaneously, emissions from a particular molecule in multiple orders can be coadded and analyzed together, significantly improving signal-to-noise, particularly for weak (e.g., C_2H_2, NH_3) and underrepresented species.

DATA REDUCTION AND FLUX CALIBRATION

1. Initial Processing. The iSHELL spectrograph first became available for use in late 2016. A considerable, research group-wide collaborative effort was undertaken to upgrade the data reduction algorithms used in this work to be able to process iSHELL frames. The routines are otherwise identical to those used for NIRSPEC data with three important exceptions: echelle order cropping, spatial resampling (straightening), and noise calculations. Aspects of the reduction specific to iSHELL data will be highlighted.

As shown in Figure A.2 and Figure A.3, each frame contains an image of the entire NIRSPEC or iSHELL array and contains many individual echelle orders. Each order is cropped and processed individually. After combining A and B frames as described above, each difference pair is flat-fielded (the flats themselves are dark subtracted). The reduction algorithms were originally written for cropping quadrilateral sections (in the case

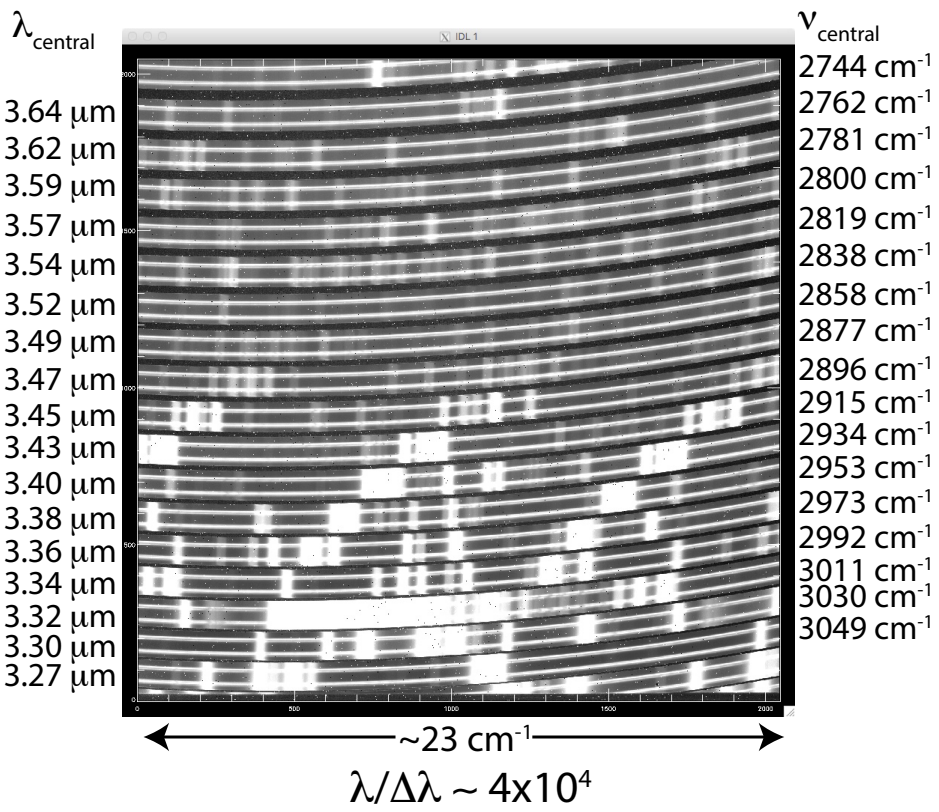

Figure A.3. The LP1 setting of iSHELL, including the frequency range of each echelle order, showing its nearly continuous spectral coverage within a setting.

of NIRSPEC), and were modified to accommodate cropping parabolic sections (in the case of iSHELL) to isolate orders based on user-defined inputs for the edges of each. After cropping, each order is cleaned of cosmic ray hits and "hot" (high dark current) pixels using a "sigma cleaning" algorithm, which flags pixels exceeding a user-defined tolerance threshold and cleans them using a near-neighbor averaging procedure.

At this point, the cropped order is still curved (for iSHELL) or slanted (for NIRSPEC), and the spectral lines are tilted at an angle (this is clearly visible for the sky lines in Figure A.2) and needs to be straightened such that each row corresponds to a unique spatial position along the slit and each column to a unique wavelength. Spatial resampling (spatial straightening) is achieved by fitting a Gaussian to the peak signal of the A and B beams in each column. A polynomial is then fit to these peaks (one polynomial for the peak row of

the A beam in each column, and another for the peak row of the B beam in each column) and is used to remove the curvature. For comets in which continuum is not visible in an A–B difference frame, the spatial straightening solution from the same setting and order of the standard star is used. The star and comet orders fall on the array in an identical manner, and the solution from the star is sufficient to properly remove spatial curvature from comet orders.

For NIRSPEC, and initially for iSHELL, spatial resampling was performed with a second order polynomial fit. This was the case for observations of C/2012 K1 (PanSTARRS) and 2P/Encke presented in this work. As more and more iSHELL data sets were acquired, including very high signal-to-noise standard star sets, it became apparent that spatial resampling with a third order polynomial more completely removed the curvature from the spatial dimension of iSHELL frames, and this was applied to iSHELL observations of 21P/Giacobini-Zinner. It is important to note that spatial resampling with a second order polynomial has been verified to completely straighten NIRSPEC frames. Similarly, comparisons of second order and third order spatial resampling were performed on 2P/Encke iSHELL data in advance of its publication. Results derived with both methods were consistent for 2P/Encke within uncertainty, and the results of the original second order spatial resampling were published.

Once each order has been straightened in the spatial dimension, it must be straightened in the spectral direction such that each column corresponds to a unique wavelength. The following approximation:

$$\nu(x) = \nu_{cen} + disp_1|x - x_0| + disp_2(x - x_0)^2 \tag{A.1}$$

relates column pixel number (x) and wavenumber (ν), where $\nu_{\rm cen}$ is the central wavenumber of the order and $disp_1$ and $disp_2$ are the first and second order dispersion terms. Dispersion coefficients are calculated for the left and right sides of the order separately, for a total of

five spectral resampling parameters. These parameters are adjusted by comparing sky lines in each order to a telluric radiance model. Now that the orders are straightened in both the spatial and spectral dimensions, wavelength calibration is achieved by again comparing sky lines to a telluric radiance model. Column burdens for telluric absorbers are calculated by fitting a telluric absorption model to observed telluric line intensities and widths. The telluric radiance and absorption models were calculated with the Line-by-Line-Radiative Transfer Model (LBLRTM, Clough *et al.* (2005); Villanueva *et al.* (2011b)) for observations of C/2012 K1 (PanSTARRS) and 2P/Encke, and with the Planetary Spectrum Generator (following Villanueva *et al.* (2015)) for observations of 21P/Giacobini-Zinner. Finally, each A–B pair is registered by identifying the peak position of continuum emission in the A and B positions in order to correct for drift of the comet along the slit during an AB sequence. Spectra are extracted from the processed frames by summing signal over 9 rows (for NIRSPEC) or 15 rows (for iSHELL), five (seven) rows to each side of the nucleus, defined as the peak of dust emission in a given echelle order.

2. A Note Regarding Noise in iSHELL Frames. In the case of iSHELL, reduced quantum efficiency near the edges of the chip result in lower S/N at the left and right ends of each echelle order. At present, a precise formalism for modeling this noise is unavailable. The data reduction algorithms therefore employ an algorithm for modeling noise based on NIRSPEC, as well as a routine to measure actual noise in each iSHELL frame. Careful analysis has shown that for high S/N data, such as 2P/Encke presented in this work, the differences between modeled and measured noise in iSHELL spectra are negligibly small. For data that push the limits of iSHELL's sensitivity, such as the analysis of CH_4 in comet 21P/Giacobini-Zinner, these differences are more pronounced and cannot be ignored. Therefore, the analysis of 21P/Giacobini-Zinner iSHELL frames was performed using measured noise in each frame in place of modeled noise.

3. Calculation of Nucleocentric Production Rates. Nucleocentric molecular production rates ($Q_{\rm NC}$) were calculated for each line using:

$$Q_{NC} = \frac{4\pi\Delta^2 F_i}{g_i \tau (hc\nu) f(x)} \tag{A.2}$$

where Δ is the geocentric distance in meters, $F_{\rm i}$ is the flux from the *i*th line incident at the top of the terrestrial atmosphere (W m^{-2}), $g_{\rm i}$ is the line fluorescence efficiency (*g*-factor) at $R_{\rm h}$ = 1 AU (photons s^{-1} molecule^{-1}), $hc\nu$ is the energy (J) of a photon with wavenumber ν (cm^{-1}), τ is the photodissociation time of a molecule at $R_{\rm h}$ = 1 AU (Huebner *et al.*, 1992), and *f(x)* is the fraction of molecules in the coma along the column described by the beam (of size 0.43″ × 1.8″ for NIRSPEC extracts, and of size 0.75″ × 2.5″ for iSHELL extracts), assuming outgassing purely from the nucleus and uniform outflow. An expression for calculating $f(x)$ for square pixels is given in Hoban *et al.* (1991). A gas outflow speed of $v_{\rm gas} = 800 \cdot R_h^{-0.5}$ m s^{-1} was assumed based on velocity-resolved measurements of comets at radio wavelengths (e.g., Biver *et al.* (2006); Cordiner *et al.* (2014)).

4. *Q*-curves, Growth Factors, and Global Production Rates. Due to the use of a narrow slit (0.75″ for iSHELL, 0.432″ for NIRSPEC) slit, atmospheric seeing inevitably reduces flux along lines of sight passing close to the nucleus, thereby depressing the calculated $Q_{\rm NC}$. The *Q*-curve formalism, first developed for analysis of OCS in C/1995 O1 (Hale-Bopp) (Dello Russo *et al.*, 1998), is used to correct for these effects. To generate *Q*-curves, production rates are calculated for each line at progressive intervals along the slit using equation A.2, summing up the flux contained in each interval and accounting for $f(x)$ (Figure A.4). Once slit positions have been reached that are sufficiently far away from the nucleus, seeing no longer dominates the measured flux and calculated production rates reach a "terminal" (or total) value, $Q_{\rm total}$, which is constant within uncertainty. The growth factor (GF) is defined as GF = $Q_{\rm total}/Q_{NC}$, and relates the nucleocentric production

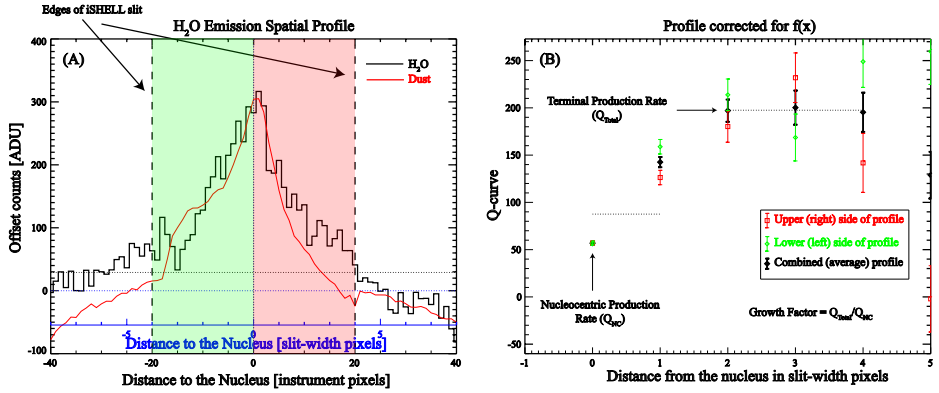

Figure A.4. A. Emission spatial profile of H_2O (black) and dust (red) in comet 2P/Encke on UT 2017 March 22 (Roth *et al.*, 2018). The "lower" side of the slit is shaded in green, and the "upper" side of the slit is shaded in red. B. Q-curve for the H_2O emission shown in panel A. The green diamonds represent the production rates measured from summed flux (corrected for $f(x)$) at each slit position from the "lower" side of the slit, red squares represent the same for positions on the "upper" side of the slit, and black diamonds are the average of the red and green measurements. The nucleocentric (Q_{NC}) and terminal (Q_{total}) production rates are indicated, as well as the identification of the growth factor (GF) as their ratio.

rate calculated for each line to the global (or total) production rate. The production rates reported in this work are weighted averages of the global production rates calculated for each observed line of a given species.

5. Determination of Rotational Temperature (T_{rot}). Rotational temperatures were determined using multiple complementary methods as detailed in Bonev (2005), Bonev *et al.* (2008a), DiSanti *et al.* (2006), and Villanueva *et al.* (2008). For the purposes of this work, these includes correlation and excitation analyses. Each will be described in turn.

5.1. Correlation analysis. Correlation analysis is useful for placing initial constraints on T_{rot} and for examining pure goodness-of-fit between model and data. In correlation analysis, synthetic fluorescence emission models are generated over a range of temperatures. The correlation coefficient (R) measuring the goodness-of-fit for the model at each temperature is recorded and plotted, making a "correllogram" (Figure A.5). The optimum temperature is found at the maximum point of the correllogram (the point of

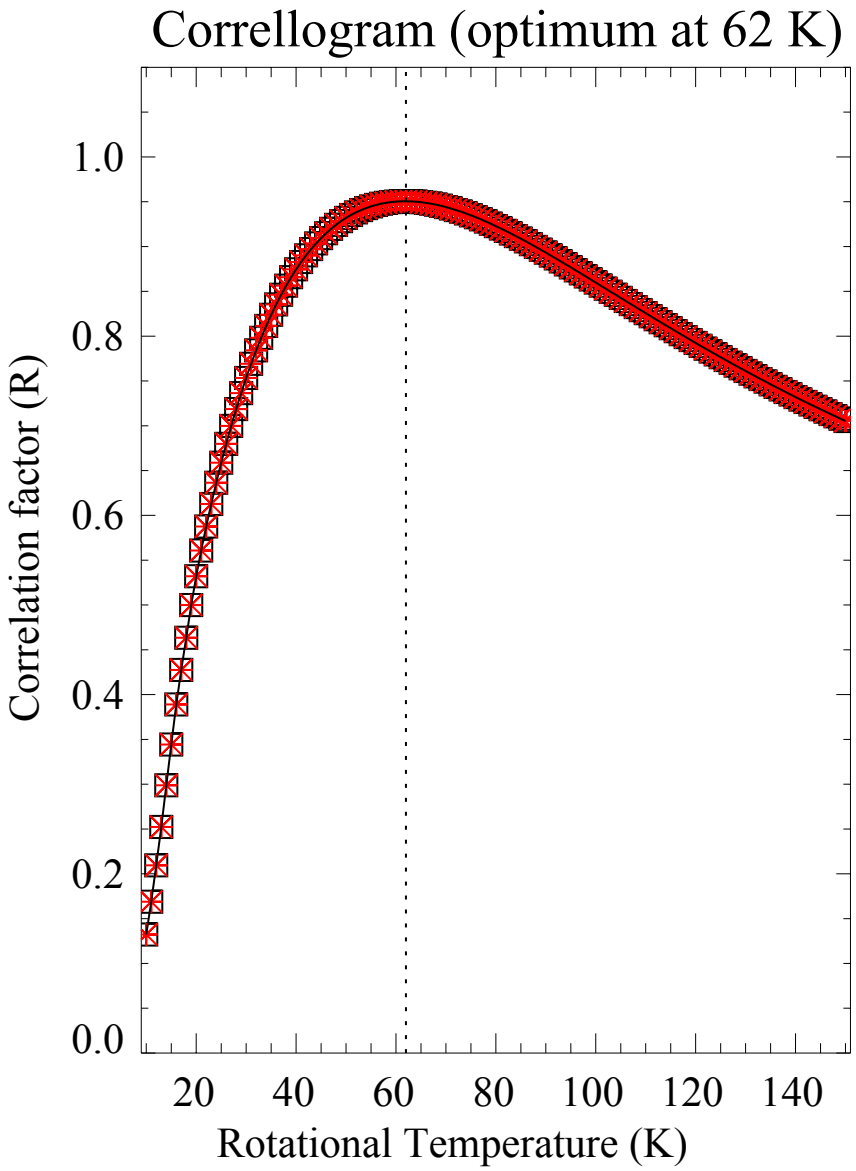

Figure A.5. Correllogram showing goodness-of-fit to H_2O emissions in 2P/Encke on UT 2017 March 25, with an optimum found at T_{rot} = 62 K. Note that the lower end of the temperature range is more well-constrained than the upper end.

maximum correlation). Figure A.5 shows a correllogram generated by fitting models of non-resonant fluorescence models for H_2O to dozens of H_2O lines near 2.9 μm in 2P/Encke on UT 2017 March 25. The optimum temperature is found to be 62 K based on the maximum in the correllogram.

The "sharpness" of the correllogram can also provide information regarding how well correlation analysis can constrain $T_{\rm rot}$ in a particular data set, both overall and with respect to low vs. high temperatures. A flat correllogram indicates that the data are fit by the models at each temperature with essentially the same goodness-of-fit, in which case correlation analysis is not very diagnostic of $T_{\rm rot}$. In contrast, a sharp correllogram indicates that a certain temperature (or range of temperatures) clearly fits the data better and is more diagnostic. Furthermore, the correllogram can provide insight into how well the different rotational levels are sampled for a particular set of lines. In the case of Figure A.5, the lower side of the correllogram is much sharper than the upper side, indicating that a larger number of lines with relatively low rotational energies in the ground vibrational state are being sampled compared to lines with relatively high rotational energies.

5.2. Excitation ("zero-slope") analysis. Once a preliminary range of probable $T_{\rm rot}$ has been identified through correlation analysis, excitation analysis (Dello Russo *et al.*, 2004) is used to identify the best-fit rotational temperature. In contrast to correlation analysis, which is mainly sensitive to how well a model fits the data, excitation analysis is sensitive to the range of rotational energies in the ground vibrational state that are sampled in a given spectrum. Excitation analysis takes advantage of the fact that for each line, $Q_i \propto F_i/g_i \propto N_i$, where $Q_{\rm i}$ is the production rate of each line, $F_{\rm i}$ is the flux of each line measured at the top of the terrestrial atmosphere, $g_{\rm i}$ is the g-factor (intensity) of each line, and $N_{\rm i}$ is the column density of molecules. For each line, $F_{\rm i}$ is a measured quantity and $g_i = g_i(T_{rot})$ is a modeled quantity that is dependent on $T_{\rm rot}$. When a sufficiently large spread in rotational energies is sampled, these quantities can be manipulated in the following fashion.

The inner coma being sampled by near-infrared measurements can be assumed to be in local thermodynamic equilibrium (Bonev, 2005), with sufficient density for its molecules to be thermalized by collisions; therefore, the population of rotational levels in the ground vibrational state is governed by a Boltzmann distribution characterized by a temperature, $T_{\rm rot}$. For each line, the quantity $F_i/g_i(T_{rot})$ (or equivalently, $N_{\rm i}$) is plotted versus its rotational

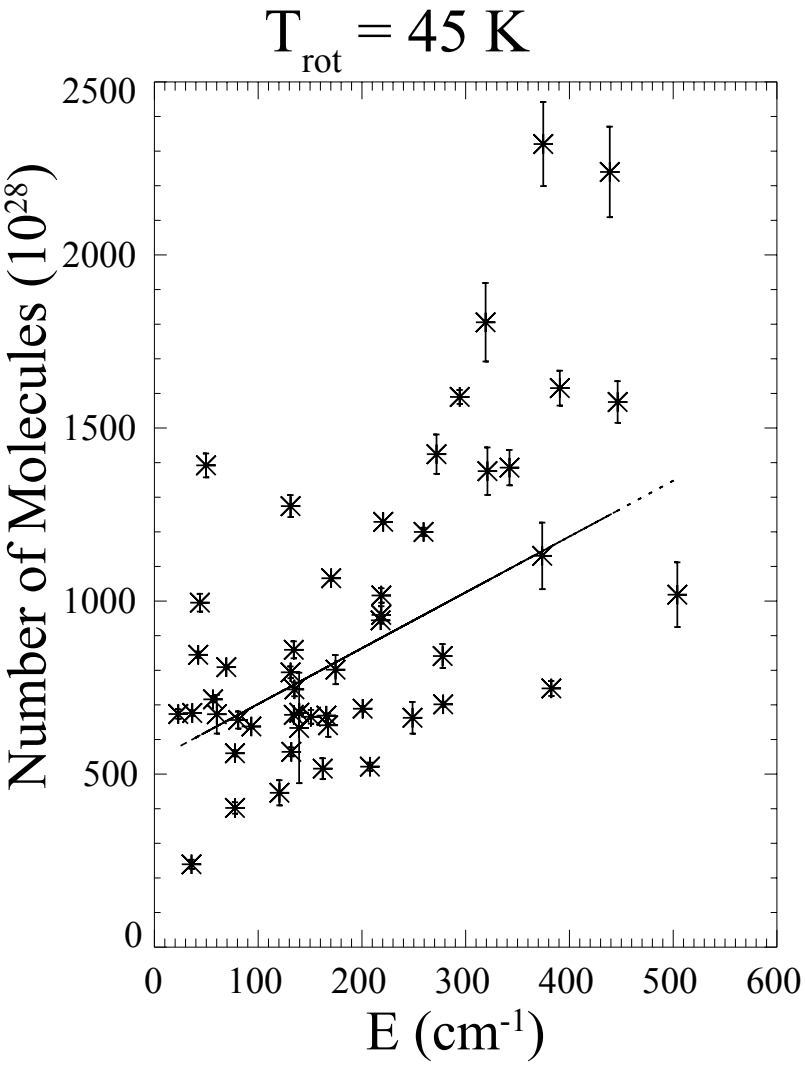

Figure A.6. Excitation analysis of H_2O in comet 2P/Encke at T_{rot} = 45 K. Note the positive slope of the best-fit line, indicating that the best-fit rotational temperature is higher than 45 K.

energy in the upper vibrational state (E_{up}) – this is referred to as an "excitation diagram". Figure A.6 shows an excitation diagram for dozens of H_2O lines near 2.9 μm in 2P/Encke on UT 2017 March 25 at T_{rot} = 45 K, along with the best-fit trend line.

It is clear that a wide range of upper state rotational energies is sampled, as well as that the slope of the best-fit line at T_{rot} = 45 K is positive. Recall for what follows that $N_i \propto F_i/g_i$. The measured flux of each line is indicative of the population in their upper state

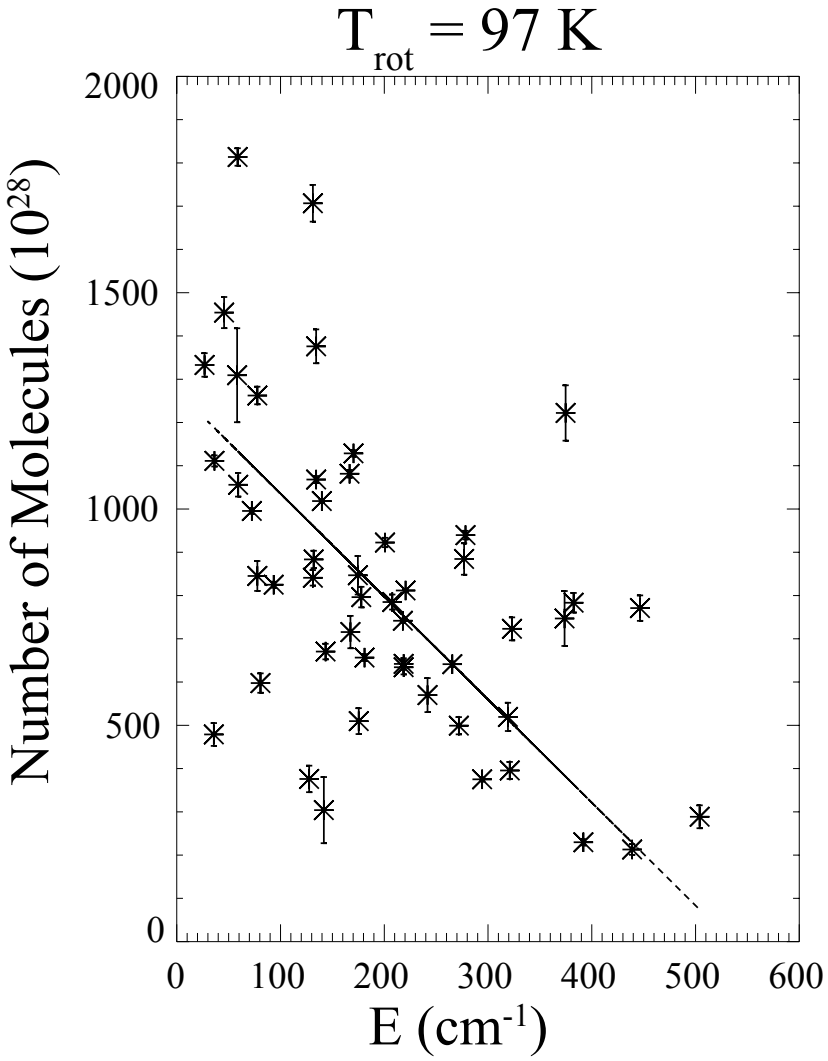

Figure A.7. Excitation analysis of H_2O in comet 2P/Encke at T_{rot} = 97 K. Note the negative slope of the best-fit line, indicating that the best-fit rotational temperature is lower than 97 K.

rotational energy levels. The upper state rotational energies of each line are not dependent on T_{rot}. However, the relative populations of the upper state rotational energies are dependent on the rotational populations in the ground vibrational state, which are directly dependent on T_{rot} (Bonev, 2005).

When the modeled T_{rot} is too low, $g_i(T_{rot})$ will be overestimated for lower-energy lines and underestimated for higher-energy lines, leading to a positive slope in the best-fit line in a plot of F_i/g_i vs. E_{up} (Figure A.6). Conversely, when the modeled T_{rot}

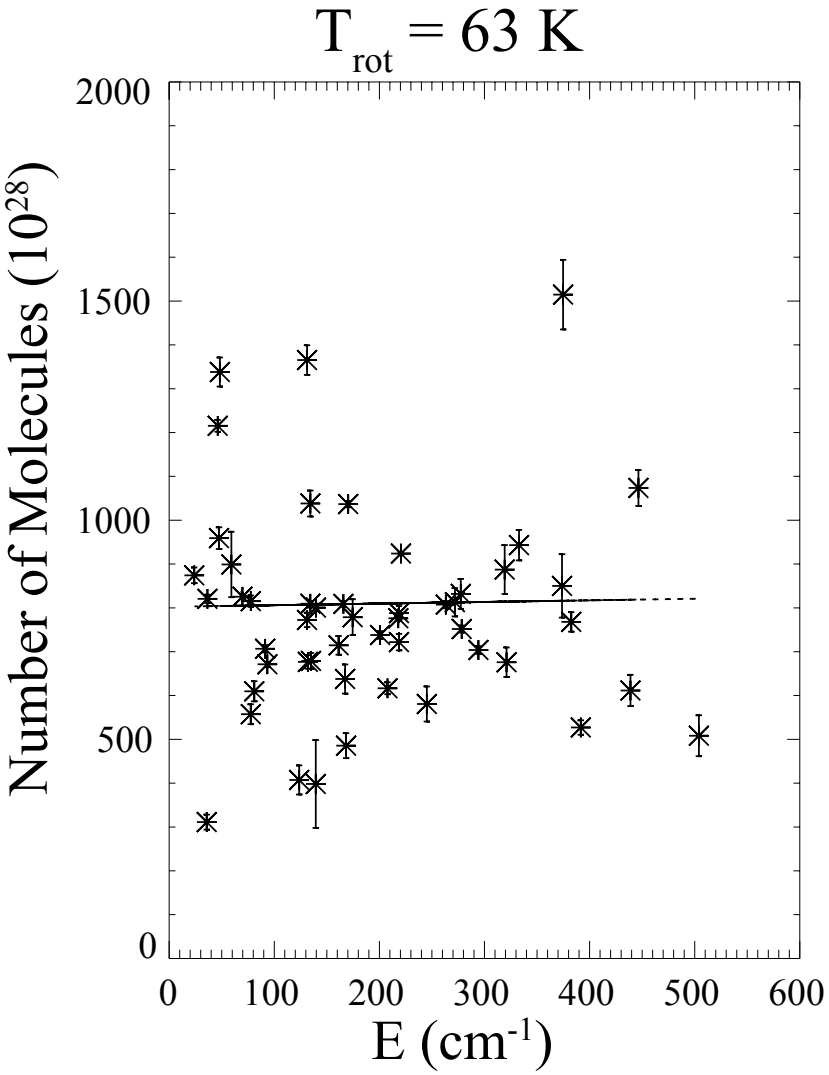

Figure A.8. Excitation analysis of H_2O in comet 2P/Encke at T_{rot} = 63 K. Note the zero slope of the best-fit line, indicating that the best-fit rotational temperature is consistent with 63 K.

is too high, $g_i(T_{rot})$ will be underestimated for lower-energy lines and overestimated for higher-energy lines, resulting in a negative slope to the best-fit line for F_i/g_i vs. E_{up} (Figure A.7). However, when the rotational temperature that accurately describes the Boltzmann distribution governing the lower-state rotational population levels is chosen,

F_i/g_i will be independent of upper-state rotational energy: each line will give the same $Q_i \propto F_i/g_i \propto N_i$, and the slope of the best-fit line for F_i/g_i vs. E_{up} will be zero within uncertainty (Figure A.8).

6. Uncertainties in measurements. It is important to provide a detailed accounting of the uncertainties associated with each of the measured or retrieved quantities reported in this work. These quantities include molecular production rates (determined as the weighted mean of individual production rates for each measured line of a given species), rotational temperatures (determined as the temperature which produces a zero-slope best-fit line when relating F/g vs. E_{up} for each line of a given species), and growth factors. The reduction algorithms employed in this work calculate two sources of uncertainty for each quantity: stochastic error and standard error.

The stochastic error is a measure of the signal-to-noise ratio of each of the lines used to calculate the aforementioned quantities. For all but the brightest comets, the signal from emission lines in the coma is weaker than the background signal introduced by the sky, including continuum and emission lines from telluric species – hence the dominant source of noise in the measured flux of each cometary line originates from thermal background noise (Bonev, 2005). The standard error is a measure of how quantities derived from the lines (e.g., Q_i, F_i/g_i) are spread about the weighted mean or about the best-fit line. In contrast to the stochastic error, the standard error is indicative of uncertainties introduced by modeled quantities (such as the g-factors): for instance, the flux of a C_2H_6 line may be measured with very high signal-to-noise, yet the production rate derived from the line may be in poor agreement with those derived from other C_2H_6 lines if its g-factor is poorly modeled.

In the case of global production rates and growth factors, these uncertainties are the stochastic and standard errors in the weighted means used to calculate each quantity. In the case of rotational temperatures derived with excitation analysis, the uncertainties are the stochastic and standard errors in a linear best fit. It is important to note that in most cases,

the standard error is found to dominate over the stochastic error when using the instruments, models, and reduction algorithms employed in this work. The following will examine how these quantities are incorporated into:

1. Uncertainties in molecular production rates introduced by uncertainties in rotational temperatures, uncertainties in growth factors, uncertainties in the telluric absorption model, and uncertainties in flux calibration.

2. Uncertainties in the abundance ratios, including for molecules whose transitions are in separate instrumental settings (i.e., abundance ratios between molecules that are not observed simultaneously).

6.1. Uncertainties in molecular production rates. The molecular production rates reported in this work are the weighted averages of the production rates calculated for each line of an individual species. The uncertainty associated with production rates for individual lines, $Q_{\rm i}$, is the stochastic error. When calculating the overall production rate using the weighted average of these quantities, both the stochastic error and the standard error of the average are calculated, and the larger of the two is taken to be the overall uncertainty. However, calculating this average production rate requires additional quantities, including the rotational temperature, the transmittance predicted by the telluric absorption model at the frequency of each line, the growth factor of each molecule, and the flux calibration determined for each spectral order.

In the case of the rotational temperature, uncertainties can be introduced in the slope of the best-fit line of F/g vs. E_{up} by uncertainties in the measured flux of each line, whether due to low signal-to-noise in the measured flux, uncertainties in modeling of the transmittance function (and hence the correction for telluric absorption) at the frequency of the line, or uncertainties in the applied flux calibration. Additional uncertainty can be introduced by the modeled *g*-factor, or the predicted intensity of the lines. Each of these will contribute to a greater spread in the derived F/g of individual lines about the best-fit

line and are accounted for by the standard error calculation. In general, the possible spread in production rates due to uncertainty in rotational temperature is found to be well within the uncertainty limits given by the standard error of the weighted average production rates reported in this work.

In the calculation of the growth factor, uncertainties are introduced by the spread of the production rates calculated at successive intervals along the slit about the "terminal" production rate value. The production rates at each position along the slit inside the terminal region are incorporated into a weighted average, and the standard and stochastic error are calculated, with the greater being taken as the overall uncertainty. Errors in the growth factor, especially when the growth factor of H_2O is assumed for weaker trace species, are systematic: while they introduce uncertainties in the production rates, they do not affect the uncertainties in calculated mixing ratios.

Finally, uncertainty in flux calibration can introduce uncertainties in the derived production rates. Similar to the growth factor, these uncertainties are systematic within a given instrumental setting and will affect the production rates but not the derived mixing ratios. The algorithms employed in this work incorporate a 10% uncertainty due to flux calibration in the reported measurements.

6.2. Uncertainties in abundance ratios. Once the production rates have been calculated, the final task is to derive mixing ratios, or relative abundances. In this case, the standard errors of the weighted average production rates of each species are added in quadrature, which gives the uncertainty in their abundance ratio. However, for molecules whose transitions are not observed simultaneously (e.g., if the mixing ratio CH_4/H_2O was calculated using $Q(CH_4)$ from the iSHELL Lp1 setting and $Q(H_2O)$ from the M2 setting), an additional source of uncertainty is introduced due to the variable nature of the coma and the considerable amount of time required to take measurements in two separate settings (on the order of several hours). The uncertainty introduced in such measurements is estimated to be 10%, which is added to the uncertainty in the calculated mixing ratios.

APPENDIX B

COPYRIGHT AGREEMENTS

COPYRIGHT AGREEMENTS FOR WORKS PUBLISHED

This dissertation include materials from works published or submitted for publication in the American Astronomical Society's *The Astronomical Journal*. These include Section 2 (Roth *et al.*, 2017), Section 3 (Roth *et al.*, 2018) and Section 4 (Roth *et al.*, 2019). Included for reference are the copyright agreements signed by Roth and coauthors specifying the rights granted to them, including the right to reproduce all or part of their articles in their own future works, such as this dissertation.

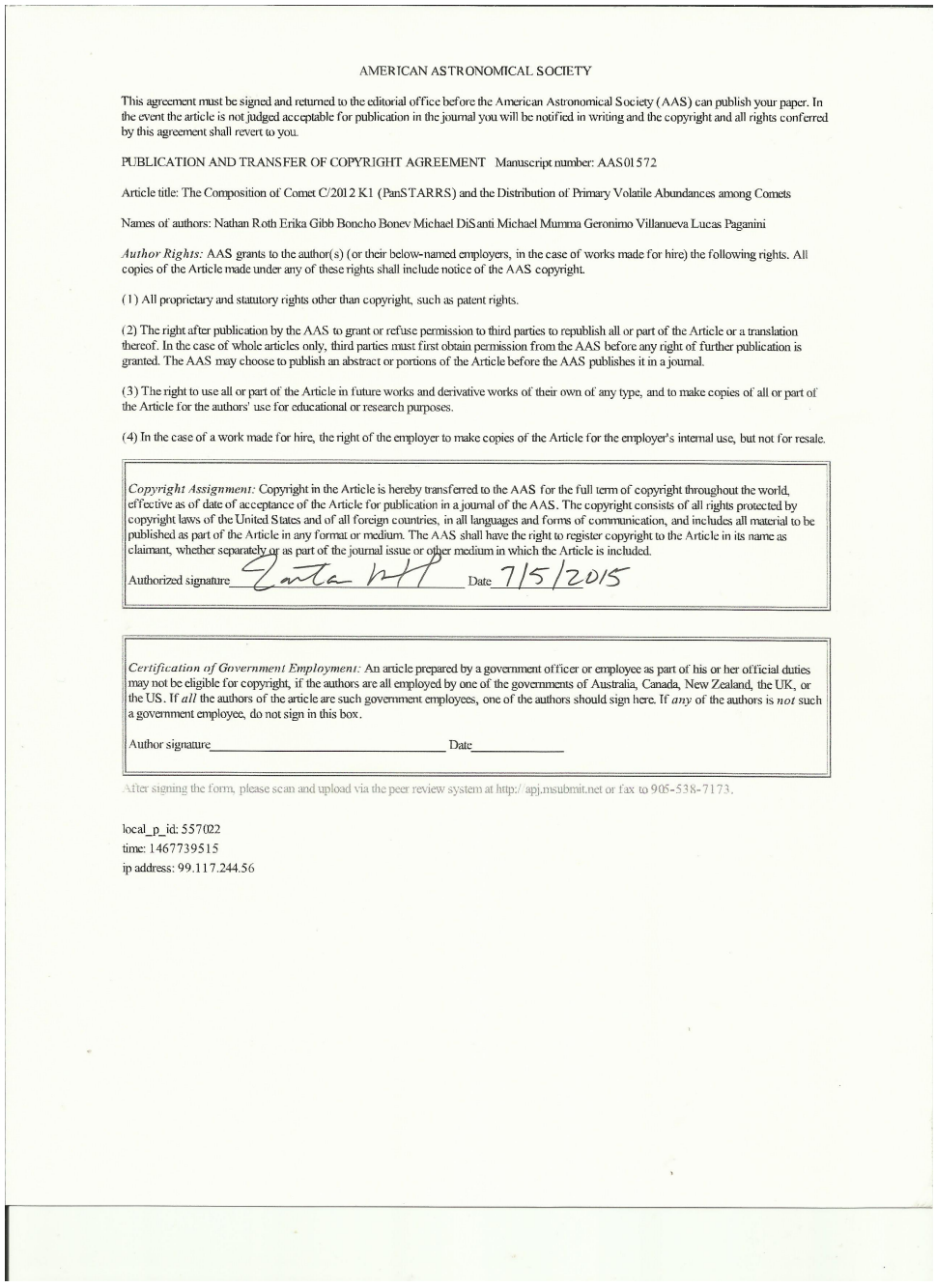

AMERICAN ASTRONOMICAL SOCIETY

This agreement must be signed and returned to the editorial office before the American Astronomical Society (AAS) can publish your paper. In the event the article is not judged acceptable for publication in the journal you will be notified in writing and the copyright and all rights conferred by this agreement shall revert to you.

PUBLICATION AND TRANSFER OF COPYRIGHT AGREEMENT Manuscript number: AAS01572

Article title: The Composition of Comet C/2012 K1 (PanSTARRS) and the Distribution of Primary Volatile Abundances among Comets

Names of authors: Nathan Roth Erika Gibb Boncho Bonev Michael DiSanti Michael Mumma Geronimo Villanueva Lucas Paganini

Author Rights: AAS grants to the author(s) (or their below-named employers, in the case of works made for hire) the following rights. All copies of the Article made under any of these rights shall include notice of the AAS copyright.

(1) All proprietary and statutory rights other than copyright, such as patent rights.

(2) The right after publication by the AAS to grant or refuse permission to third parties to republish all or part of the Article or a translation thereof. In the case of whole articles only, third parties must first obtain permission from the AAS before any right of further publication is granted. The AAS may choose to publish an abstract or portions of the Article before the AAS publishes it in a journal.

(3) The right to use all or part of the Article in future works and derivative works of their own of any type, and to make copies of all or part of the Article for the authors' use for educational or research purposes.

(4) In the case of a work made for hire, the right of the employer to make copies of the Article for the employer's internal use, but not for resale.

Copyright Assignment: Copyright in the Article is hereby transferred to the AAS for the full term of copyright throughout the world, effective as of date of acceptance of the Article for publication in a journal of the AAS. The copyright consists of all rights protected by copyright laws of the United States and of all foreign countries, in all languages and forms of communication, and includes all material to be published as part of the Article in any format or medium. The AAS shall have the right to register copyright to the Article in its name as claimant, whether separately or as part of the journal issue or other medium in which the Article is included.

Authorized signature Date 7/5/2015

Certification of Government Employment: An article prepared by a government officer or employee as part of his or her official duties may not be eligible for copyright, if the authors are all employed by one of the governments of Australia, Canada, New Zealand, the UK, or the US. If *all* the authors of the article are such government employees, one of the authors should sign here. If *any* of the authors is *not* such a government employee, do not sign in this box.

Author signature Date

After signing the form, please scan and upload via the peer review system at http://apj.msubmit.net or fax to 905-538-7173.

local_p_id: 557022
time: 1467739515
ip address: 99.117.244.56

Figure B.1. Copyright agreement between Roth and coauthors and the American Astronomical Society for Roth *et al.* (2017).

AMERICAN ASTRONOMICAL SOCIETY

This agreement must be electronically signed before the American Astronomical Society (AAS) can publish your paper. In the event the article is not judged acceptable for publication in the journal you will be notified in writing and the copyright and all rights conferred by this agreement shall revert to you.

PUBLICATION AND TRANSFER OF COPYRIGHT AGREEMENT Manuscript number: AAS11181

Article title: A Tale of "Two" Comets: The Primary Volatile Composition of Comet 2P/Encke Across Apparitions and Implications for Cometary Science

Names of authors: Nathan Roth Erika Gibb Boncho Bonev Michael DiSanti Neil Dello Russo Ronald Vervack Adam McKay Hideyo Kawakita

Author Rights: AAS grants to the author(s) (or their below-named employers, in the case of works made for hire) the following rights. All copies of the Article made under any of these rights shall include notice of the AAS copyright.

(1) All proprietary and statutory rights other than copyright, such as patent rights.

(2) The right after publication by the AAS to grant or refuse permission to third parties to republish all or part of the Article or a translation thereof. In the case of whole articles only, third parties must first obtain permission from the AAS before any right of further publication is granted. The AAS may choose to publish an abstract or portions of the Article before the AAS publishes it in a journal.

(3) The right to use all or part of the Article in future works and derivative works of their own of any type, and to make copies of all or part of the Article for the authors' use for educational or research purposes.

(4) In the case of a work made for hire, the right of the employer to make copies of the Article for the employer's internal use, but not for resale.

(5) In the case of a Gold Open Access work, each of the named authors and, where relevant, the employer consents to the publication of the work under the Creative Commons Attribution 3.0 license (https://creativecommons.org/licenses/by/3.0/) or any successor to that license.

Copyright Assignment: Copyright in the Article is hereby transferred to the AAS for the full term of copyright throughout the world, effective as of date of acceptance of the Article for publication in a journal of the AAS. The copyright consists of all rights protected by copyright laws of the United States and of all foreign countries, in all languages and forms of communication, and includes all material to be published as part of the Article in any format or medium. The AAS shall have the right to register copyright to the Article in its name as claimant, whether separately or as part of the journal issue or other medium in which the Article is included and the right to sue, counterclaim, and recover for past, present and future infringement of the rights assigned under this agreement.

This Agreement shall be controlled, construed and enforced in accordance with the laws of the District of Columbia without reference to the conflict of laws provisions thereof. The Parties consent to jurisdiction of the state and federal courts located in the District of Columbia in connection with any proceeding related to this Agreement or its enforcement.

Authorized Signature: Nathan Roth Date: 5/8/2018

Certification of Government Employment: An article prepared by a government officer or employee as part of his or her official duties may not be eligible for copyright, if the authors are all employed by one of the governments of Australia, Canada, New Zealand, the UK, or the US. If all the authors of the article are such government employees, one of the authors should sign here. If any of the authors is not such a government employee, do not sign in this box.

Authorized Signature:
Date:

local_p_id: 667241
time: 1525796452
ip address: 99.117.244.56

Figure B.2. Copyright agreement between Roth and coauthors and the American Astronomical Society for Roth *et al.* (2018).

AMERICAN ASTRONOMICAL SOCIETY

This agreement must be electronically signed before the American Astronomical Society (AAS) can publish your paper. In the event the article is not judged acceptable for publication in the journal you will be notified in writing and the copyright and all rights conferred by this agreement shall revert to you.

PUBLICATION AND TRANSFER OF COPYRIGHT AGREEMENT Manuscript number: AAS17919

Article title: Probing the Evolutionary History of Comets: An Investigation of the Hypervolatiles CO, CH4, and C2H6 in the Jupiter-family Comet 21P/Giacobini-Zinner

Names of authors: Nathan Roth Erika Gibb Boncho Bonev Michael DiSanti Neil Dello Russo Adam McKay Ronald Vervack Hideyo Kawakita Mohammad Saki Nicolas Biver Dominique Bockelee-Morvan Lori Feaga Nicolas Fougere Anita L. Cochran Michael R. Combi Yinsi Shou

Author Rights: AAS grants to the author(s) (or their below-named employers, in the case of works made for hire) the following rights. All copies of the Article made under any of these rights shall include notice of the AAS copyright.

(1) All proprietary and statutory rights other than copyright, such as patent rights.

(2) The right after publication by the AAS to grant or refuse permission to third parties to republish all or part of the Article or a translation thereof. In the case of whole articles only, third parties must first obtain permission from the AAS before any right of further publication is granted. The AAS may choose to publish an abstract or portions of the Article before the AAS publishes it in a journal.

(3) The right to use all or part of the Article in future works and derivative works of their own of any type, and to make copies of all or part of the Article for the authors' use for educational or research purposes.

(4) In the case of a work made for hire, the right of the employer to make copies of the Article for the employer's internal use, but not for resale.

(5) In the case of a Gold Open Access work, each of the named authors and, where relevant, the employer consents to the publication of the work under the Creative Commons Attribution 3.0 license (https://creativecommons.org/licenses/by/3.0/) or any successor to that license.

Copyright Assignment: Copyright in the Article is hereby transferred to the AAS for the full term of copyright throughout the world, effective as of date of acceptance of the Article for publication in a journal of the AAS. The copyright consists of all rights protected by copyright laws of the United States and of all foreign countries, in all languages and forms of communication, and includes all material to be published as part of the Article in any format or medium. The AAS shall have the right to register copyright to the Article in its name as claimant, whether separately or as part of the journal issue or other medium in which the Article is included and the right to sue, counterclaim, and recover for past, present and future infringement of the rights assigned under this agreement.

This Agreement shall be controlled, construed and enforced in accordance with the laws of the District of Columbia without reference to the conflict of laws provisions thereof. The Parties consent to jurisdiction of the state and federal courts located in the District of Columbia in connection with any proceeding related to this Agreement or its enforcement.

Authorized Signature: Nathan Roth Date: 05/21/2019

Certification of Government Employment: An article prepared by a government officer or employee as part of his or her official duties may not be eligible for copyright, if the authors are all employed by one of the governments of Australia, Canada, New Zealand, the UK, or the US. If all the authors of the article are such government employees, one of the authors should sign here. If any of the authors is not such a government employee, do not sign in this box.

Authorized Signature:
Date:

local_p_id: 667241
time: 1558442868
ip address: 99.117.244.56

Figure B.3. Copyright agreement between Roth and coauthors and the American Astronomical Society for Roth *et al.* (2019).

REFERENCES

A'Hearn, M. F., 'Comets: looking ahead,' Philosophical Transactions of the Royal Society A, 2017, **375**(2097), p. 20160261.

A'Hearn, M. F., Belton, M. J. S., Delamere, W. A., Feaga, L. M., Hampton, D., Kissel, J., Klaase, K. P., McFadden, L. A., Meech, K. J., Melosh, H. J., Schultz, P. H., Sunshine, J. M., Thomas, P. C., Veverka, J., Wellnitz, D. D., Yeomans, D. K., Besse, S., Bodewits, D., Bowling, T. J., Carcich, B. T., Collins, S. M., Farnham, T. L., Groussin, O., Hermalyn, B., Kelley, M. S., Kelley, M. S., Li, J.-Y., Lindler, D. J., Lisse, C. M., McLaughlin, S. A., Merlin, F., Protopapa, S., Richardson, J. E., and Williams, J. L., 'EPOXI at comet Hartley 2,' Science, 2011, **332**(6036), p. 1396.

A'Hearn, M. F., Birch, P. V., Feldman, P. D., and Millis, R. L., 'Comet Encke - gas production and lightcurve,' Icarus, 1985, **64**(1), pp. 1–10.

A'Hearn, M. F., Millis, R. C., Schleicher, D. O., Osip, D. J., and Birch, P. V., 'The ensemble properties of comets: Results from narrowband photometry of 85 comets, 1976-1992,' Icarus, 1995, **118**(2), pp. 223–270.

Biver, N., 'Ethyl alcohol and sugar in comet C/2014 Q2 (Lovejoy,' Science Advances, 2015, **1**, p. e1500863.

Biver, N., Bockelée-Morvan, D., Crovisier, J., Lis, D. C., Moreno, R., Colom, P., Henry, F., Herpin, F., Paubert, G., and Womack, M., 'Radio wavelength molecular observations of comets C/1999 T1 (McNaught-Hartley), C/2001 A2 (LINEAR), C/2000 WM1 (LINEAR) and 153P/Ikeya-Zhang,' Astronomy and Astrophysics, 2006, **449**(3), p. 1255.

Biver, N., Bockelée-Morvan, D., Hofstadter, M., Lellouch, E., Choukroun, M., Gulkis, S., Crovisier, J., Schloerb, F. P., Rezac, L., von Allmen, P., Lee, S., Leyrat, C., Ip, W. H., Hartogh, P., Encrenaz, P., Beaudin, G., and the MIRO team, 'Long-term monitoring of the outgassing and composition of comet 67P/Churyumov-Gerasimenko with the Rosetta/MIRO instrument,' Astronomy & Astrophysics, 2019, **in press**.

Bockelée-Morvan, D., Calmonte, U., Charnley, S., Duprat, J., Engrand, C., Gicquel, A., Hässig, M., Jehin, E., Kawakita, H., Marty, B., Milam, S., Morse, A., Rousselot, P., Sheridan, S., and Wirstrom, E., 'Cometary isotopic measurements,' Space Science Reviews, 2015, **197**, pp. 47–83.

Bockelée-Morvan, D., Crovisier, J., Erard, S., Capaccioni, F., Leyrat, C., Filacchione, G., Drossart, P., Encrenaz, T., Biver, N., de Sanctis M.-C., Schmitt, B., Kührt, E., M.-T., C., Combes, M., Combi, M., Fougere, N., Arnold, G., Fink, U., Ip, W., Migliorini, A., Piccioni, G., and Tozzi, G., 'Evolution of CO2, CH4, and OCS abundances relative to H2O in the coma of comet 67P around perihelion from Rosetta/VIRTIS-H observations,' Monthly Notices of the Royal Astronomical Society, 2016, **462**(1), pp. S1270–S183.

Bodewits, D., Farnham, T. L., A'Hearn, M. F., Feaga, L. M., McKay, A., Schleicher, D. G., and Sunshine, J. M., 'The evolving activity of the dynamically young comet C/2009 P1 (Garradd),' The Astrophysical Journal, 2014, **786**, p. 48.

Boissier, J., Bockelée-Morvan, D., Biver, N., Colom, P., Crovisier, J., Moreno, R., Zakharov, V., Groussin, O., Jorda, L., and Lis, D. C., 'Gas and dust productions of comet 103P/Hartley 2 from millimetre observations: Interpreting rotation-induced time variations,' Icarus, 2014, **228**, p. 197.

Bonev, B. P., *Towards a Chemical Taxonomy of Comets: Infrared Spectroscopic Methods for Quantitative Measurements of Cometary Water (With an Independent Chapter on Mars Polar Science)*, phdthesis, The University of Toledo, 2005.

Bonev, B. P. and Mumma, M. J., 'A comprehensive study of infrared OH prompt emission in two comets. ii. implications for unimolecular dissociation of H2O.' The Astrophysical Journal, 2006, **653**(1), pp. 788–791.

Bonev, B. P., Mumma, M. J., DiSanti, M. A., Dello Russo, N., Magee-Sauer, K., Ellis, R. S., and Stark, D. P., 'A comprehensive study of infrared OH prompt emission in two comets. i. observations and effective g-factors,' The Astrophysical Journal, 2006, **653**(1), pp. 774–787.

Bonev, B. P., Mumma, M. J., Kawakita, H., Kobayashi, H., and Villanueva, G. L., 'Ircs/subaru observations of water in the inner coma of comet 73P-B/Schwassmann Wachmann 3: Spatially resolved rotational temperatures and ortho para ratios,' Icarus, 2008a, **196**(1), pp. 241–248.

Bonev, B. P., Mumma, M. J., Radeva, Y. L., DiSanti, M. A., Gibb, E. L., and Villanueva, G. L., 'The peculiar volatile composition of comet 8P/Tuttle: A contact binary of chemically distinct cometesimals?' The Astrophysical Journal Letters, 2008b, **680**(1), p. L61.

Bonev, B. P., Mumma, M. J., Villanueva, G. L., DiSanti, M. A., Ellis, R. S., Magee-Sauer, K., and Dello Russo, N., 'A search for variation in the H2O ortho-para ratio and rotational temperature in the inner coma of comet C/2004 Q2 (Machholz),' The Astrophysical Journal, 2007, **661**(1), pp. L97–L100.

Bonev, B. P., Villanueva, G. L., DiSanti, M. A., Boehnhardt, H., Lippi, M., Gibb, E. L., Paganini, L., and Mumma, M. J., 'Beyond 3 au from the Sun: The hypervolatiles CH4, C2H6, and CO in the distant comet C/2006 W3 (Christensen),' The Astronomical Journal, 2017, **153**(5), p. 241.

Bregman, J. D., Witteborn, F. C., Allamandola, L. J., Campins, H., Wooden, D. H., Rank, D. M., Cohen, M., and Tielens, A. G. G. M., 'Airborn and groundbased spectrophotometry of comet P/Halley from 5-13 micrometers,' Astronomy and Astrophysics, 1987, **187**(1-2), pp. 616–620.

Brooke, T. Y., Weaver, H. A., Chin, G., Bockelée-Morvan, D., Kim, S. J., and Xu, L.-H., 'Spectroscopy of comet Hale-Bopp in the infrared,' Icarus, 2003, **166**(1), pp. 167–187.

Capaccioni, F., Coradini, A., Filacchione, G., Erard, S., Arnold, G., Drossart, P., De Sanctis, M. C., Bockelée-Morvan, D., Capria, M. T., Tosi, F., Leyrat, C., B., S., Quirico, E., Ceronni, P., Mennella, V., Raponi, A., Ciarniello, M., McCord, T., Moroz, L., Palomba, E., Ammannito, E., Barucci, M. A., Gellucci, G., Benkhoff, J., Bilbring, J. P., Blanco, A., Blecka, M., Carlson, R., Carsenty, U., Colangeli, L., Combes, M., Combi, M., Crovisier, J., Encrenaz, T., Federico, C., Fink, U., Fonti, S., Ip, W. H., Irwin, P., Jaumann, R., Kuehrt, E., Langevin, Y., Magni, G., Mottola, S., Orofino, V., Palumbo, P., Piccioni, G., Schade, U., Taylor, F., Tiphene, G., Tozzi, G. P., Beck, P., Biver, N., Bonal, L., Combe, J. P., Despan, D., Flamini, E., Fornasier, S., Friger, A., Grassi, D., Gudipati, M., Longobardo, A., Markus, K., Merlin, F., Orosei, R., Rinaldi, G., Stephan, K., Cartacci, M., Cicchetti, A., Giuppi, S., Hello, Y., Henry, F., Jacquinod, S., Noschese, R., Peter, G., Politi, R., Reess, J. M., and Semery, A., 'The organic-rich surface of comet 67P/Churyumov-Gerasimenko as seen by VIRTIS/Rosetta,' Science, 2015, **347**(6220), p. aaa0628.

Clough, S. A., Shephard, M. W., Mlawer, E. J., Delamere, J. S., Iacono, M. J., Cady-Pereira, K., Boukabara, S., and Brown, P. D., 'Atmospheric radiative transfer modeling: a summary of the aer codes,' Journal of Quantitative Spectroscopy and Radiative Transfer, 2005, **91**(2), pp. 233–244.

Cochran, A. L., Barker, E. S., and Gray, C. L., 'Thirty years of cometary spectroscopy from mcdonald observatory,' Icarus, 2012, **218**(1), pp. 144–168.

Cochran, A. L., Levasseur-Regourd, A.-C., Cordiner, M., Hadamcik, E., Lasue, J., Gicquel, A., Schleicher, D., Charnley, S. B., Mumma, M. J., Paganini, L., Bockelée-Morvan, D., Biver, N., and Kuan, Y.-J., 'The composition of comets,' Space Science Reviews, 2015, **197**(1-4), pp. 9–46.

Cordiner, M. A., Remijan, A. J., Boissier, J., Milam, S. N., Mumma, M. J., Charnley, S. B., Paganini, L., Villanueva, G., Bockelée-Morvan, D., Kuan, Y. J., Chuang, Y. L., Lis, D. C., Biver, N., Crovisier, J., Minniti, D., and Coulson, I. M., 'Mapping the release of volatiles in the inner comae of comets C/2012 F6 (Lemmon) and C/2012 S1 (ISON) using the Atacama Large Millimeter/Submillimeter Array,' The Astrophysical Journal Letters, 2014, **792**, p. L2.

Cottin, H. and Fray, N., 'Distributed sources in comets,' Space Science Reviews, 2008, **138**, pp. 179–197.

Crovisier, J., Biver, N., Bockelée-Morvan, D., Bossier, J., Colom, P., and Lis, D. C., 'The chemical diversity of comets: Synergies between space exploration and ground-based radio observations,' Earth, Moon, and Planets, 2009, **105**(2-4), pp. 267–272.

Dello Russo, N., DiSanti, M. A., Magee-Sauer, K., Gibb, E. L., Mumma, M. J., Barber, R. J., and Tennyson, J., 'Water production and release in comet 153P/Ikeya-Zhang (C/2002 C1): accurate rotational temperature retrievals from hot-band lines near 2.9-μm,' Icarus, 2004, **168**(1), pp. 186–200.

Dello Russo, N., DiSanti, M. A., Mumma, M. J., Magee-Sauer, K., and Rettig, T. W., 'Carbonyl sulfide in comets C/1996 B2 (Hyakutake) and C/1995 O1 (Hale-Bopp): Evidence for an extended source in Hale-Bopp,' Icarus, 1998, **135**(2), pp. 377–388.

Dello Russo, N., Kawakita, H., Bonev, B. P., Vervack, R. J. J., Gibb, E. L., Shinnaka, Y., Roth, N. X., DiSanti, M. A., and McKay, A. J., 'Post-perihelion volatile production and release from Jupiter-family comet 45P/Honda-Mrkos-Pajdusakova,' Icarus, 2019, **submitted**.

Dello Russo, N., Kawakita, H., Jr., V. R. J., and Weaver H., A., 'Emerging trends and a comet taxonomy based on the volatile chemistry measured in thirty comets with high-resolution infrared spectroscopy between 1997 and 2013,' Icarus, 2016a, **278**, pp. 301–332.

Dello Russo, N., Mumma, M. J., DiSanti, M. A., and Magee-Sauer, K., 'Production of ethane and water in comet C/1996 B2 Hyakutake,' Journal of Geophysical Research (Planets), 2002b, **107**(E11), p. 5095.

Dello Russo, N., Mumma, M. J., DiSanti, M. A., Magee-Sauer, K., and Novak, R., 'Ethane production and release in comet C/1995 O1 Hale-Bopp,' Icarus, 2001, **153**(1), pp. 162–179.

Dello Russo, N., Mumma, M. J., DiSanti, M. A., Magee-Sauer, K., Novak, R., and Rettig, T. W., 'Water production and release in comet C/1995 O1 Hale-Bopp,' Icarus, 2000, **143**(2), pp. 324–337.

Dello Russo, N., Vervack, R. J. J., Kawakita, H., Cochran, A., McKay, A. J., Harris, W. M., Weaver, H. A., Lisse, C. M., DiSanti, M. A., Kobayashi, H., Biver, N., Bockelée-Morvan, D., Crovisier, J., Opitom, C., and Jehin, E., 'The compositional evolution of C/2012 S1 (ISON) from ground-based high-resolution infrared spectroscopy as part of a worldwide observing campaign,' Icarus, 2016b, **266**, pp. 152–175.

Dello Russo, N., Vervack, R. J. J., Lisse, C. M., Weaver, H. A., Kawakita, H., Kobayashi, H., Cochran, A. L., Harris, W. M., McKay, A. J., Biver, N., Bockelée-Morvan, D., and Crovisier, J., 'The volatile composition and activity of comet 103P/Hartley 2 during the EPOXI closest approach,' The Astrophysical Journal Letters, 2011, **734**(1), p. L8.

Dello Russo, N., Vervack, R. J. J., Weaver, H. A., Biver, N., Bockelée-Morvan, D., Crovisier, J., and Lisse, C. M., 'Compositional homogeneity in the fragmented comet 73P/Schwassmann-Wachmann 3,' Nature, 2007, **448**(7150), pp. 172–175.

DiSanti, M. A., Bonev, B. P., Dello Russo, N., Vervack, R. J. J., Gibb, E. L., Roth, N. X., McKay, A. J., and Kawakita, H., 'Hypervolatiles in a Jupiter-family comet: Observations of 45P/Honda-Mrkos-Pajdušáková using iSHELL at the NASA-IRTF,' The Astronomical Journal, 2017, **154**(6), p. 246.

DiSanti, M. A., Bonev, B. P., Gibb, E. L., Paganini, L., Villanueva, G. L., Mumma, M. J., Keane, J. V., Blake, G. A., Dello Russo, N., Meech, K., Vervack, R. J. J., and McKay, A. J., 'En route to destruction: The evolution in composition of ices in comet D/2012 S1 (ISON) between 1.2 and 0.34 au from the Sun as revealed at infrared wavelengths,' The Astrophysical Journal, 2016, **820**(1), p. 20.

DiSanti, M. A., Bonev, B. P., Magee-Sauer, K., Dello Russo, N., Mumma, M. J., Reuter, D. C., and Villanueva, G. L., 'Detection of formaldehyde emission in comet C/2002 T7 (LINEAR) at infrared wavelengths: Line-by-line validation of modeled fluorescent intensities,' The Astrophysical Journal, 2006, **650**(1), pp. 470–483.

DiSanti, M. A., Bonev, B. P., Villanueva, G. L., and Mumma, M. J., 'Highly depleted ethane and mildly depleted methanol in comet 21P/Giacobini-Zinner: Application of a new emprical v2-band model for CH3OH near 50 K,' The Astrophysical Journal, 2013, **763**(1), p. 19.

DiSanti, M. A., Mumma, M. J., Dello Russo, N., and Magee-Sauer, K., 'Carbon monoxide production and excitation in comet C/1995 O1 (Hale-Bopp): Isolation of native and distributed CO sources,' Icarus, 2001, **153**(2), pp. 361–390.

DiSanti, M. A., Mumma, M. J., Dello Russo, N., Magee-Sauer, K., and Griep, D. M., 'Evidence for a dominant native source of carbon monoxide in comet C/1996 B2 (Hyakutake),' Journal of Geophysical Research Planets, 2003, **108**(E61), p. 5061.

DiSanti, M. A., Villanueva, G. L., Paganini, L., Bonev, B. P., Keane, J. V., Meech, K. J., and Mumma, M. J., 'Pre- and post-perihelion observations of C/2009 P1 (Garradd): Evidence for an oxygen-rich heritage?' Icarus, 2014, **228**, pp. 167–180.

Dorman, G., Pierce, D. M., and Cochran, A. L., 'The spatial distribution of C2, C3, and NH in comet 2P/Encke,' The Astrophysical Journal, 2013, **778**(2), p. 140.

Drahus, M., Jewitt, D., Guilbert-Lepoutre, A., Waniak, W., and Sievers, A., 'The sources of HCN and CH3OH and the rotational temperature in comet 103P/Hartley 2 from time-resolved millimeter spectroscopy,' The Astrophysical Journal, 2012, **756**, p. 80.

Drozdovskaya, M. N., Walsh, C., van Dishoeck, E. F., Furuya, K., Marboeuf, U., Thiabaud, A., Harsono, D., and Visser, R., 'Cometary ices in forming protoplanetary disc midplanes,' Monthly Notices of the Royal Astronomical Society, 2016, **462**(1), pp. 977–993.

Emel'Yanenko, V. V., Asher, D. J., and Bailey, M. E., 'The fundamental role of the Oort cloud in determining the flux of comets through the planetary system,' Monthly Notices of the Royal Astronomical Society, 2007, **381**(2), pp. 779–789.

Faggi, S., Villanueva, G. L., Mumma, M. J., and Paganini, L., 'The volatile composition of comet C/2017 E4 (Lovejoy) before its disruption, as revealed by high-resolution infrared spectroscopy with iSHELL at the NASA/IRTF,' The Astronomical Journal, 2018, **156**, p. 68.

Farnham, T. L., 'Coma morphology of Jupiter-family comets,' Planetary and Space Science, 2009, **57**(10), pp. 1192–1217.

Feaga, L. M., A'Hearn, M. F., Farnham, T. L., Bodewits, D., Sunshine, J. M., Gersch, A. M., Protopapa, S., Yang, B., Drahus, M., and Schleicher, D. G., 'Uncorrelated volatile behavior during the 2011 apparition of Comet C/2009 P1 Garradd,' The Astronomical Journal, 2014, **147**(1), p. 24.

Feldman, P. D., A'Hearn, M. F., Bertaux, J. L., Feaga, L. M., Keeney, B. A., Knight, M. W., Noonan, J., Parker, J. W., Schindhelm, E., Steffl, A. J., Stern, A. S., Vervack, R. J., and Weaver, H. A., 'FUV spectral signatures of molecules and the evolution of the gasesous coma of comet 67P/Churyumov-Gerasimenko,' The Astronomical Journal, 2018, **155**(1), p. 9.

Fernandez, Y. R., Lowry, S. C., Weissman, P. R., Mueller, B. E. A., Samarasinha, N. H., Belton, M. J. S., and Meech, K. J., 'New near-aphelion light curves of comet 2P/Encke,' Icarus, 2005, **175**(1), pp. 194–214.

Ferrin, I., 'Secular light curve of 2P/Encke, a comet active at aphelion,' Icarus, 2008, **197**(1), pp. 169–182.

Fink, U., 'A taxonoic survey of comet composition 1985-2004 using ccd spectroscopy,' Icarus, 2009, **201**(1), pp. 311–344.

Fink, U., Doose, L., Rinaldi, G., Bieler, A., Capaccioni, F., Bockelée-Morvan, D., Filacchione, G., Erard, S., Leyrat, C., Blecka, M., Capria, M. T., Combi, M., Crovisier, J., De Sanctis, M. C., Fougere, N., Taylor, F., Migliorini, A., and Piccioni, G., 'Investigation into the disparate origin of CO2 and H2O outgassing for comet 67/P,' Icarus, 2016, **277**, pp. 78–97.

Fougere, N., Altwegg, K., Berthelier, J. J., Bieler, A., Bockelée-Morvan, D., Calmonte, U., Cappacioni, F., Combi, M. R., De Keyser, J., Debout, V., Erard, S., Fiethe, B., Filacchione, G., Fink, U., Fuselier, S. A., Gombosi, T. I., Hansen, K. C., Hässig, M., Huang, Z., Le Roy, L., Leyrat, C., Migliorini, A., Piccioni, G., Rinaldi, G., Rubin, M., Shou, Y., Tenishev, V., Toth, G., and Tzou, C. Y., 'Direct simulation Monte Carlo modeling of the major species in the coma of comet 67P/Churyumov-Gerasimenko,' Monthly Notices of the Royal Astronomical Society, 2016a, **162**, pp. S156–S169.

Fougere, N., Altwegg, K., Berthelier, J. J., Bieler, A., Bockelée-Morvan, D., Calmonte, U., Cappacioni, F., Combi, M. R., De Keyser, J., Debout, V., Erard, S., Fiethe, B., Filacchione, G., Fink, U., Fuselier, S. A., Gombosti, T. I., Hansen, K. C., Hässig, M., Huang, Z., Le Roy, L., Leyrat, C., Migliorini, A., Piccioni, g., Rinaldi, G., Rubin, M., Shou, Y., Tenishev, V., Togh, G., and Tzou, C. Y., 'Three-dimensional direct simulation Monte-Carlo modeling of the coma of comet 67P/Churyumov-Gerasimenko observed by the VIRTIS and ROSINA instruments on board Rosetta,' Astronomy and Astrophysics, 2016b, **588**, p. A134.

Fray, N., Bénilan, Y., Biver, N., Bockelée-Morvan, D., Cottin, H., Crovisier, J., and Gazeau, M.-C., 'Heliocentric evolution of the degradation of polyoxymethylene: Application to the origin of the formaldehyde (H2CO) extended source in comet C/1995 O1 (Hale-Bopp),' Icarus, 2006, **184**(1), pp. 239–254.

Gibb, E. L., Bonev, B. P., Villanueva, G., DiSanti, M. A., Mumma, M. J., Sudholt, E., and Radeva, Y., 'Chemical composition of comet C/2007 N3 (Lulin): Another "atypical" comet,' The Astrophysical Journal, 2012, **750**(2), p. 102.

Gibb, E. L., Mumma, M. J., Dello Russo, N., DiSanti, M. A., and Magee-Sauer, K., 'Methane in Oort cloud comets,' Icarus, 2003, **165**(2), pp. 391–406.

Gomes, R., Levison, H. F., Tsiganis, K., and Morbidelli, A., 'Origin of the cataclysmic late heavy bombardment period of the terrestrial planets,' Nature, 2005, **435**(7041), pp. 466–469.

Harker, D. E., Woodward, C. E., and Wooden, D. H., 'The dust grains from 9P/Tempel 1 before and after the encounter with Deep Impact,' Science, 2005, **310**(5746), pp. 278–280.

Hoban, S., Mumma, M., Reuter, D. C., DiSanti, M., Joyce, R. R., and Storrs, A., 'A tentative identification of methanol as the progenitor of the 3.52-um emission feature in several comets,' Icarus, 1991, **93**, p. 122.

Huebner, W. F., Keady, J. J., and Lyon, S. P., 'Solar photo rates for planetary atmospheres and atmospheric pollutants,' Astrophysics and Space Science, 1992, **195**(1), pp. 1–294.

Hässig, M., Altwegg, K., Balsiger, H., Bar-Nun, A., Berthelier, J. J., Bochsler, P., Briois, C., Calmonte, U., Combi, M., De Keyser, J., Eberhardt, P., Fiethe, B., Fuselier, S. A., Galand, M., Gasc, S., Gombosi, T. I., Hansen, K. C., Jäckel, A., Keller, H. U., Kopp, E., Korth, A., Kührt, E., Le Roy, L., Mall, U., Marty, B., Mousis, O., Neefs, E., Owen, T., Rème, H., Rubin, M., Sémon, T., Tornow, C., Tzou, C.-Y., Waite, J. H., and Wurz, P., 'Tie variability and heterogeneity in the coma of 67P/Churyumov-Gerasimenko,' Science, 2015, **347**(6220), p. aaa0276.

Ihalawela, C. A., Pierce, D. M., Dorman, G. R., and Cochran, A. L., 'The spatial distribution of OH and CN radicals in the coma of comet Encke,' The Astrophysical Journal, 2011, **741**(2), p. 89.

Kawakita, H., Dello Russo, N., Vervack, R. J. J., Kobayashi, H., DiSanti, M. A., Opitom, C., Jehin, E., Weaver, H. A., Cochran, A. L., Harris, W. M., Bockelée-Morvan, D., Biver, N., Crovisier, J., McKay, A. J., Manfroid, J., and Gillon, M., 'Extremely organic-rich coma of comet C/2010 G2 (Hill) during its outburst in 2012,' The Astrophysical Journal, 2014, **788**(2), p. 110.

Kelley, M. S. P., Woodward, C. E., Bodewits, D., Farnham, T. L., Gudipat, M. S., Harker, D. E., Hines, D. C., Knight, M. W., Kolokolova, L., Li, A., de Pater, I., Protopapa, S., Russel, R. W., Sitko, M. L., and Wooden, D. H., 'Cometary science with the James Webb Space Telescope,' Publications of the Astronomical Society of the Pacific, 2016, **128**(959), p. 018009.

Kiselev, N. N., Jockers, K., Rosenbush, V. K., Velichko, F. P., Bonev, T., and Karpov, N., 'Anomalous wavelength dependence of polarization of comet 21P/Giacobini-Zinner,' Planetary and Space Science, 2000, **48**(10), p. 1005.

Le Roy, L., Altwegg, K., Balsiger, H., Berthelier, J.-J., Bieler, A., Briois, C., Calmonte, U., Combi, M. R., De Keyser, J., Dhooghe, F., Fiethe, B., Fuselier, S. A., Gasc, S., Gombosi, T. I., Hässig, M., Jäckel, A., Rubin, M., and Tzou, C.-Y., 'Inventory of the volatiles on comet 67P/Churyumov-Gerasimenko from Rosetta/ROSINA,' Astronomy & Astrophysics, 2015, **583**, p. A1.

Levison, H. F., Morbidelli, A., Tsiganis, K., Nesvorny, D., and Gomes, R., 'Late orbital instabilities in the outer planets induced by interaction with a self-gravitating planetesimal disk,' The Astronomical Journal, 2011, **142**(5), p. 152.

Levison, H. F., Terrel, D., Wiegert, P. A., Dones, L., and Duncan, M. J., 'On the origin of the unusual orbit of comet 2P/Encke,' Icarus, 2006, **182**(1), pp. 161–168.

Lippi, M., Villanueva, G. L., DiSanti, M. A., Böhnhardt, H., Mumma, M. J., Bonev, B. P., and Prialnik, D., 'A new model for the v1 vibrational band of HCN in cometary comae, with application to three comets,' Astronomy & Astrophysics, 2013, **551**, p. A51.

Lowry, S. C. and Weissman, P. R., 'Rotation and color properties of the nucleus of comet 2P/Encke,' Icarus, 2007, **188**(1), pp. 212–223.

Luspay-Kuti, A., Hässig, M., Fuselier, S. A., Mandt, K. E., Altwegg, K., Balsiger, H., Gasc, S., Jäckel, A., Le Roy, L., Rubin, M., Tzou, C.-Y., Wurz, P., Mousis, O., Dhooghe, F., Berthelier, J. J., Fiethe, B., Gombosi, T. I., and Mall, U., 'Composition-dependent outgassing of comet 67P/Churyumov-Gerasimenko from ROSINA/DFMS. implications for nucleus heterogeneity?' Astronomy & Astrophysics, 2015, **583**, p. A4.

Magee-Sauer, K., Mumma, M. J., DiSanti, M. A., and Dello Russo, N., 'Hydrogen cyanide in comet C/1996 B2 Hytakutake,' Journal of Geophysical Research (Planets), 2002b, **107**(E11), p. 5096.

Magee-Sauer, K., Mumma, M. J., DiSanti, M. A., Dello Russo, N., Gibb, E. L., Bonev, B. P., and Villanueva, G. L., 'The organic composition of comet C/2002 A2 (LINEAR). i. evidence for an unusual organic chemistry,' Icarus, 2008, **194**(1), pp. 347–356.

Magee-Sauer, K., Mumma, M. J., DiSanti, M. A., Dello Russo, N., and Rettig, T. W., 'Infrared spectroscopy of the v3 band of hydrogen cyanide in comet C/1995 O1 Hale-Bopp,' Icarus, 1999, **142**(2), pp. 498–508.

McKay, A. J., Cochran, A. L., DiSanti, M. A., Villanueva, G., Dello Russo, N., Vervack, R. J. J., Morgenthaler, J. P., Harris, W. M., and Chanover, N. J., 'Evolution of H2O, CO, and CO2 production in comet C/2009 P1 Garradd during the 2011-2012 apparition,' Icarus, 2015, **250**, pp. 504–515.

McKay, A. J., Kelley, M. S. P., Cochran, A. L., Bodewits, D., DiSanti, M. A., Dello Russo, N., and Lisse, C. M., 'The CO2 abundance in comets C/2012 K1 (PanSTARRS), C/2015 K5 (LINEAR), and 290P/Jäger as measured with Spitzer,' Icarus, 2016, **266**, pp. 249–260.

McLean, I. S., Becklin, E. E., Bendiksen, O., Brims, G., Canfield, J., Figer, D. F., Graham, J. R., Hare, J., Lacayanga, F., Larkin, J. E., Larson, S. B., Levenson, N., Magnone, N., Teplitz, H., and Wong, W., 'Design and development of NIRSPEC: a near-infrared echelle spectrograph for the Keck II telescope,' Proceedings of the SPIE, 1998, **3354**, pp. 566–578.

Milam, S. N., Adande, G., Cordiner, M. A., Wirstrom, E., and Charnley, S. B., 'Molecular tracers of nitrogen enrichment in prestellar cores: amines vs. nitriles,' in 'Proceedings of the 46th Lunar and Planetary Science Conference,' 2015 p. 1934.

Morbidelli, A., Levison, H. F., Tsiganis, K., and Gomes, R., 'Chaotic capture of Jupiter's Trojan asteroids in the early solar system,' Nature, 2005, **435**(7041), pp. 462–465.

Mumma, M. J., Bonev, B. P., Villanueva, G. L., Paganini, L., DiSanti, M. A., Gibb, E. L., Keane, J. V., Meech, K. J., Blake, G. A., Ellis, R. S., Lippi, M., Boehnhardt, H., and Magee-Sauer, K., 'Temporal and spatial aspects of gas release during the 2010 apparition of comet 103P/Hartley 2,' The Astrophysical Journal Letters, 2011, **734**(1), p. L7.

Mumma, M. J. and Charnley, S. B., 'The chemical composition of comets - emerging taxonomies and natal heritage,' Annual Review of Astronomy and Astrophysics, 2011, **49**(1), pp. 471–524.

Mumma, M. J., Dello Russo, N., DiSanti, M. A., Magee-Sauer, K., Novak, R., Conrad, A., and Chaffee, F., 'Comet C/1999 T1 (McNaught-Hartley),' IAU Circular, 2001b, **7578**.

Mumma, M. J., DiSanti, M. A., Dello Russo, N., Fomenkova, M., Magee-Sauer, K., Kaminski, C. D., and Xie, D. X., 'Detection of abundant ethane and methane, along with carbon monoxide and water, in comet C/1996 B2 Hyakutake: Evidence for interstellar origin,' Science, 1996, **272**(5266), pp. 1310–1314.

Mumma, M. J., DiSanti, M. A., Dello Russo, N., Magee-Sauer, K., Gibb, E., and Novak, R., 'Remote infrared observations of parent volatiles in comets: A window on the early solar system,' Advances in Space Research, 2003, **31**(12), pp. 2563–2575.

Mumma, M. J., DiSanti, M. A., Dello Russo, N., Magee-Sauer, K., and Rettig, T. W., 'Detection of CO and ethane in comet 21P/Giacobini-Zinner: Evidence for variable chemistry in the outer solar nebula,' The Astrophysical Journal, 2000, **531**(2), pp. L155–L159.

Mumma, M. J., McLean, I. S., DiSanti, M. A., Larkin, J. E., Dello Russo, N., Magee-Sauer, K., Becklin, E. E., Bida, T., Chaffee, F., Conrad, A. R., Figer, D. F., Gilbert, A. M., Graham, J. R., Levenson, N. A., Novak, R. E., Reuter, D. C., Teplitz, H. I., Wilcox, M. K., and Xu, L.-H., 'A survey of organic volatile species in comet C/1999 H1 (Lee) using NIRSPEC at the Keck Observatory,' The Astrophysical Journal, 2001, **546**(1183).

Mumma, M. J., Weaver, H. A., Larson, H. P., Davis, D. S., and Williams, M., 'Detection of water vapor in Halley's comet,' Science, 1986, **232**, pp. 1523–1528.

Nakano, S., 'NK 2588 C/2012 K1 (PANSTARRS),' Nakano Notes, 2013.

Paganini, L., Mumma, M. J., Boenhardt, H., DiSanti, M. A., Villanueva, G. L., Bonev, B. P., Lippi, M., Käufl, H. U., and Blake, G. A., 'Ground-based infrared detections of CO in the Centaur-comet 29P/Schwassmann-Wachmann 1 at 6.26 au from the Sun,' The Astrophysical Journal, 2013b, **766**(2), p. 100.

Paganini, L., Mumma, M. J., Villanueva, G. L., DiSanti, M. A., Bonev, B. P., Lippi, M., and Boehnhardt, H., 'The chemical composition of CO-rich comet C/2009 P1 (Garradd) at Rh = 2.4 and 2.0 au before perihelion,' The Astrophysical Journal Letters, 2012, **748**(1), p. L13.

Protopapa, S., Sunshine, J. M., Feaga, L. M., Kelley, M. S. P., A'Hearn, M. F., Farnham, T. L., Groussin, O., Besse, S., Merlin, F., and Li, J.-Y., 'Water ice and dust in the innermost coma of comet 103P/Hartley 2,' Icarus, 2014, **238**, pp. 191–204.

Radeva, Y. L., Mumma, M. J., Bonev, B. P., DiSanti, M. A., Villanueva, G. L., Magee-Sauer, K., Gibb, E. L., and Weaver, H. A., 'The organic composition of comet C/2000 WM1 (LINEAR) revealed through infrared spectroscopy,' Icarus, 2010, **206**(2), pp. 764–777.

Radeva, Y. L., Mumma, M. J., Villanueva, G. L., Bonev, B. P., DiSanti, M. A., A'Hearn, M. F., and Dello Russo, N., 'High-resolution infrared spectroscopic measurements of comet 2P/Encke: Unusual organic composition and low rotational temperatures,' Icarus, 2013, **223**(1), pp. 298–307.

Rayner, J., Bond, T., Bonnet, M., Jaffe, D., Muller, G., and Tokunaga, A., 'iSHELL: a 1-5 micron cross-dispered R=70,000 immersion grating spectrograph for IRTF,' Proceedings of the SPIE, 2012, **8446**, p. 84462C.

Rayner, J., Tokunaga, A., Jaffe, D., Bonnet, M., Ching, G., Connelley, M., Kokubun, D., Lockhart, C., and Warmbier, E., 'iSHELL: a construction, assembly and testing,' Proceedings of the SPIE, 2016, **9908**, p. 990884.

Rickman, H., Marchi, S., A'Hearn, M. F., Barbieri, C., El-Maarry, M. R., Güttler, C., Ip, W.-H., Keller, H. U., Lamy, P., Marzari, F., Massironi, M., Naletto, G., Pajola, M., Sierks, H., Koschny, D., Rodrigo, R., Barucci, M. A., Bertaux, J.-L., Bertini, I., Cermonese, G., Da Deppo, V., Debei, S., De Cecco, M., Fornasier, S., Fulle, M., Groussin, O., Gutiérrez, P. J., Hviid, S. F., Jorda, L., Knollenberg, J., Kramm, J.-R., Kührt, E., Küppers, M., Lara, L. M., Lazzarin, M., Lopez-Moreno, J. J., Michalik, H., Sabau, L., Thomas, N., Vincent, J.-B., and Wenzel, K.-P., 'Comet 67P/Churyumov-Gerasimenko: Constraints on its origins from OSIRIS observations,' Astronomy & Astrophysics, 2015, **583**, p. A44.

Roth, N. X., Gibb, E. L., Bonev, B. P., DiSanti, M. A., Dello Russo, N., McKay, A. J., Vervack, R. J. J., Kawakita, H., Saki, M., Biver, N., Bockelée-Morvan, D., Feaga, L., Fougere, N., Cochran, A., Combi, M., and Shou, Y., 'Probing the evolutionary history of comets: An investigation of the hypervolatiles CO, CH4, and C2H6 in the Jupiter-family comet 21P/Giacobini-Zinner,' The Astronomical Journal, 2019, **submitted**.

Roth, N. X., Gibb, E. L., Bonev, B. P., DiSanti, M. A., Dello Russo, N., Vervack, R. J. J., McKay, A. J., and Kawakita, H., 'A tale of "two" comets: The primary volatile composition of comet 2P/Encke across apparitions and implications for cometary science,' The Astronomical Journal, 2018, **156**, p. 251.

Roth, N. X., Gibb, E. L., Bonev, B. P., DiSanti, M. A., Mumma, M. J., Villanueva, G. L., and Paganini, L., 'The composition of comet C/2012 K1 (PanSTARRS) and the distribution of primary volatile abundances among comets,' The Astronomical Journal, 2017, **153**, p. 168.

Schleicher, D. and Bair, A., *Asteroids, Comets, Meteors, Book of Abstracts*, chapter Chemical and physical properties of comets in the Lowell database: Results from 35 years of narrow-band photometry, p. 475, University of Helsinki, 2014.

Sekanina, Z., 'Outgassing asymmetry of periodic comet Encke. i - apparitions 1924-1984,' The Astronomical Journal, 1988a, **95**, pp. 911–924, 970, 971.

Sekanina, Z., 'Outgassing asymmetry of periodic comet Encke. ii - apparitions 1868-1918 and a study of the nucleus evolution,' The Astronomical Journal, 1988b, **96**, pp. 1455–1475.

Stern, S. A., 'The evolution of comets in the Oort cloud and Kuiper belt,' Nature, 2003, **424**(6949), pp. 639–642.

Villanueva, G. L., Bonev, B. P., Mumma, M. J., Magee-Sauer, K., DiSanti, M. A., Salyk, C., and Geoffrey, A., 'The volatile composition of the split ecliptic comet 73P/Schwassmann-Wachmann 3: A comparison of fragments C and B,' The Astrophysical Journal, 2006, **650**(1), pp. L87–L90.

Villanueva, G. L., DiSanti, M. A., Mumma, M. J., and Xu, L.-H., 'A quantum band model of the v3 fundamental of methanol (CH3OH) and its application to fluorescence spectra of comets,' The Astrophysical Journal, 2012a, **747**(1), p. 3.

Villanueva, G. L., Magee-Sauer, K., and Mumma, M. J., 'Modeling of nitrogen compounds in cometary atmospheres: Fluorescence models of ammonia (NH3), hydrogen cyanide (HCN), hydrogen isocyanide (HNC) and cyanoacetylene (HC3N),' Journal of Quantitative Spectroscopy and Radiative Transfer, 2013, **129**, pp. 158–168.

Villanueva, G. L., Mumma, M. J., Bonev, B. P., DiSanti, M. A., Gibb, E. L., Boehnhardt, H., and Lippi, M., 'A sensitive search for deuterated water in comet 8P/Tuttle,' The Astrophysical Journal Letters, 2009, **690**(1), pp. L5–L9.

Villanueva, G. L., Mumma, M. J., Bonev, B. P., Novak, R. E., Barber, R. J., and DiSanti, M. A., 'Water in planetary and cometary atmospheres: H2O/HDO transmittance and fluorescence models,' Journal of Quantitative Spectroscopy and Radiative Transfer, 2012b, **113**(3), pp. 202–220.

Villanueva, G. L., Mumma, M. J., DiSanti, M. A., Bonev, B. P., Gibb, E. L., Magee-Sauer, K., Blake, G. A., and Salyk, C., 'The molecular composition of comet C/2007 W1 (Boattini): Evidence of a peculiar outgassing and a rich history,' Icarus, 2011a, **216**(1), pp. 227–240.

Villanueva, G. L., Mumma, M. J., and Magee-Sauer, K., 'Ethane in planetary and cometary atmospheres: Transmittance and fluorescence models of the v7 band at 3.3 um,' Journal of Geophysical Research, 2011b, **116**(E8), p. E08012.

Villanueva, G. L., Mumma, M. J., Novak, R. E., and Hewagama, T., 'Identification of a new band system of isotopic CO2 near 3.3 um: Implications for remote sensing of biomarker gases on Mars,' Icarus, 2008, **195**(1), pp. 34–44.

Villanueva, G. L., Mumma, M. J., Novak, R. E., Käufl, H. U., Hartogh, P., Encrenaz, T., Tokunaga, A., Khayat, A., and Smith, M. D., 'Strong water isotopic anomalies in the martian atmosphere: Probing current and ancient reservoirs,' Science, 2015, **348**(6231), p. 218.

Weaver, H. A., Chin, G., Bockelée-Morvan, D., Crovisier, J., Brooke, T. Y., Cruikshank, D. P., Geballe, T. R., Kim, S. J., and Meier, R., 'An infrared investigation of volatiles in comet 21P/Giacobini-Zinner,' Icarus, 1999, **142**(2), pp. 482–497.

Willacy, K., Alexander, C., Ali-Dib, M., Ceccarelli, C., Charnley, S. B., Doronin, M., Ellinger, Y., Gast, P., Gibb, E., Milam, S. N., Mousis, O., Pauzat, F., Tornow, C., Wirström, E. S., and Zicler, E., 'The composition of the protosolar disk and the formation conditions for comets,' Space Science Reviews, 2015, **197**(1-4), p. 151.

Woodney, L. M., Schleicher, D. G., Reetz, K. M., and Ryan, K. J., 'Rotational properties of comet 2P/Encke based on nucleus lightcurves and coma morphology,' Bulletin of the American Astronomical Society, 2007, **38**, p. 486.

Xie, X. and Mumma, M. J., 'Monte Carlo simultaion of cometary atmospheres: Application to comet P/Halley at the time of the Giotto spacecraft encounter. i. isotropic model,' The Astrophysical Journal, 1996a, **464**, p. 442.

Xie, X. and Mumma, M. J., 'Monte Carlo simulation of cometary atmospheres: Application to comet P/Halley at the time of the Giotto spacecraft encounter. ii. axisymmetric model,' The Astrophysical Journal, 1996b, **464**, p. 457.

Zolensky, M. E., Zega, T. J., Yano, H., Wirick, S., Westphal, A. J., Weisberg, M. K., Weber, I., Warren, J. L., Velbel, M. A., Tsuchiyama, A., Tsou, P., Toppani, A., Tomioka, N., Tomeoka, K., Teslich, N., Taheri, M., Susini, J., Stroud, R., Stephan, T., Stadermann, F. J., Snead, C. J., Simon, S. B., Simionovici, A., See, T. H., Robert, F., Rietmeijer, F. J. M., Rao, W., Perronnet, M. C., Papanastassiou, D. A., Okudaira, K., Ohsumi, K., Ohnishi, I., Nakamura-Messenger, K., Nakamura, T., Mostefaoui, S., mikouchi, T., Meibom, A., Matrajt, G., Marcus, M. A., Leroux, H., Lemelle, L., Le, L., Lanzirotti, A., Langenhort, F., Krot, A. N., Keller, L. P., Kearsey, A. T., Joswiak, D., Jacob, D., Ishii, H., Harvey, R., Hagiya, K., Grossman, L., Grossman, J. N., Graham, g. A., Gounelle, M., Gillet, P., Genge, M. J., Flynn, G., Ferroir, T., Fallon, F., Ebel, D. S., Dai, Z. R., Cordier, P., Clark, B., Chi, M., Butterworth, A. L., Brownlee, D. E., Bridges, J. C., Brennan, S., Brearley, A., Bradley, J. P., Bleuet, P., Bland, P. A., and Bastien, R., 'Mineralogy and petrology of comet 81P/Wild 2 nucleus samples,' Science, 2006, **314**(5806), p. 1735.

VITA

Nathaniel Xavier Roth was born in St. Louis, Missouri. He received his B.S. in Physics from the University of Missouri–St. Louis in December of 2014. He went on to receive his M.S. in Physics at the University of Missouri–St. Louis in August of 2016, and was awarded a NASA Earth and Space Science Fellowship in September of 2016. He received his Doctor of Philosophy in Physics from the Missouri University of Science and Technology and the University of Missouri–St. Louis in July 2019.